# STUDY OF PROJECTILE FRAGMENTATION REACTIONS AT INTERMEDIATE ENERGIES

By

George A. Souliotis

A DISSERTATION

Submitted to
Michigan State University
in partial fulfillment of the requirements
for the Degree of

DOCTOR OF PHILOSOPHY

Department of Chemistry

1992

# ABSTRACT

## STUDY OF PROJECTILE FRAGMENTATION REACTIONS AT INTERMEDIATE ENERGIES

By

George A. Souliotis

The experimental measurements of the present work represent a first attempt towards obtaining systematic data of projectile fragment distributions near 0 degrees produced by intermediate-energy beams delivered by the K1200 cyclotron at the NSCL. The measurements were performed with two different devices operated as 0-degree spectrometers: the K1200 interim beamline and the A1200 mass separator. Momentum distributions and limited angular distributions of projectile-like fragments (PLFs) from a $^{14}$N (75 MeV/u) beam with $^{27}$Al and $^{181}$Ta targets were measured using the interim K1200 beamline, but the results were of limited quality. In a first series of measurements with the A1200, the 0-degree momentum distributions of PLFs from several beams [$^{20}$Ne (85 MeV/u), $^{15}$N (70 MeV/u) and $^{18}$O (70 MeV/u)] were measured, but only a limited number of complete momentum spectra were obtained. In a second series, a detailed measurement of neutron-rich PLFs from the reaction $^{18}$O (80 MeV/u) + $^{27}$Al was successfully performed. Accurate measurements of 0-degree momentum distributions and relative yields of PLFs were obtained and analysed.

Analysis of the centroids of the momentum-per-nucleon (velocity) distributions of the fragments indicated that, along with the fragmentation (break-up) channels,

direct stripping and/or pick-up channels contribute significantly to the production of the fragments. Interestingly, the mean velocities of nucleon pick-up products were considerably lower than that of the beam, consistent with momentum conservation and the additional assumption that the nucleon(s) picked-up from the target have preferentially momenta (on average) equal to the nuclear Fermi momentum oriented in the direction of the projectile motion. The widths of the momentum distributions of both nucleon-removal and nucleon pick-up products were in agreement with the independent-particle model of Goldhaber and the cluster stripping model of Friedman. In the case of pick-up products, the momentum distributions of both the projectile part and the picked-up nucleon(s) had to be taken into account. Calculations of yields with the abrasion-ablation model and the intranuclear cascade model showed that both these high-energy models were not able to describe the trend of the data. However, calculations with Friedman's model provided a good description of the experimental yields, implying that a break-up (and/or pick-up) mechanism involving low excitation energy is responsible for the production of PLFs from the present light projectile.

To my Parents

*Antonios* and *Kyriaki*

## ACKNOWLEDGEMENTS

I wish to express my sincere thanks and deepest appreciation to my advisor, Prof. Dave Morrissey, for his guidance, support and encouragement throughout the cource of my dissertation work. His advice, suggestions and continuous interest in my work and progress have been crucial for the completion of the present thesis.

I am grateful to Dr. Brad Sherrill for his contribution, help and suggestions during the experiments and data analysis of the present work. Sincere thanks go to Dr. Dave Mikolas for his important help, guidance and friendly discussions during the initial stages of my work at the NSCL.

I would like to acknowledge Dr. Jeff Winger, Dr. Nigel Orr, Prof. Jerry Nolen and all the people that helped in the various phases of the experiments. John Yurkon and Denis Swan deserve thanks for their assistance in detector testing and operation and Orilla McHarris for her assistance in the preparation of various figures of my thesis work.

It has been an important experience to work with the excellent support of the staff and faculty of the NSCL, which I acknowledge very much. My dissertation commitee members, Profs. Dave Morrissey, Jerry Nolen, Walt Benenson and Kathy

Hunt deserve recognition for their support and guidance during my graduate career.

It is my pleasure to thank Prof. Aristides Mavridis of the University of Athens for his scientific inspiration and support during my undergraduate years in Athens. Special thanks go to Eleni Archontaki for her friendship and assistance during my first year at MSU.

I would like to express my thankfulness and gratefulness to my family, especially to my parents who have played a major role in my education with their devotion, support and encouragement throughout the years. Finally, I am grateful to Eleni not only for her friendship, thoughtfulness and encouragement during my graduate studies, but for giving inspiration to my life as well.

# Contents

# List of Tables

# List of Figures

# Chapter 1

# Introduction–Motivation

Projectile fragmentation is a specific nuclear reaction that takes place when heavy projectile nuclei (i.e. heavier than $^4$He) undergo peripheral collisions with target nuclei, mainly at intermediate and high bombarding energies. A large number of isotopes can be produced during the fragmentation of a heavy projectile. These fragments (projectile-like fragments–PLFs) emerge in a narrow cone in the forward direction with velocities near that of the projectile. Among the different PLFs, various exotic (radioactive) nuclei can be produced. These exotic nuclei can be separated and used as secondary (radioactive) beams, allowing the possibility of a new class of experiments to study nuclear structure and nuclear reaction mechanisms. For these reasons, projectile fragmentation has become a very important and powerful tool to produce and study exotic nuclei. The technique of converting a primary beam into a secondary radioactive beam by projectile fragmentation has been succesfully used at several laboratories: LBL [Alon 84], GANIL [Anne 87] and RIKEN [Kubo 90]; also, fragment separators are in the final construction stages for other laboratories (e.g. GSI [Münz 90]). At the National Superconducting Cyclotron Laboratoty (NSCL), this technique is realized with the A1200 beam analysis device [Sher 90].

In order to relate projectile fragmentation with other nuclear reaction phenomena, it is convenient to use a simple classification scheme based on two parameters of the

reaction: the relative kinetic energy of the projectile–target system and the impact parameter of the collision.

Nuclear reactions can be divided in three categories according to the bombarding energy (usually expressed in MeV/nucleon: MeV/u): low energy reactions (below 20 MeV/u), intermediate (or medium) energy reactions (between 20 and 200 MeV/u) and high (or relativistic) energy reactions (above 200 MeV/u). In the low energy region, the projectile kinetic energy is near the Coulomb barrier of the projectile–target system (E/A $\simeq$ 5 MeV). In the relativistic energy region, the projectile kinetic energy is comparable to its rest mass (E/A $\simeq$ 931 MeV). These latter energies are large compared to typical nuclear energy scales, like nucleon separation energies or the Fermi energy, which characterize the nuclear ground state. The changes between the different energy regions are gradual and the numerical values mentioned here are somewhat arbitrary.

Depending on the impact parameter of the collision, which is a measure of the degree of proximity of the reaction partners, the collisions can be divided as follows [e.g. Gelb 78, Frie 87]:

1. Distant interactions: elastic Coulomb scattering (Rutherford scattering) or inelastic Coulomb scattering (Coulomb excitation or dissociation).

2. Peripheral collisions: at low energy: direct nucleon transfer and/or incomplete fusion; at intermediate energy: projectile and target fragmentation and/or nucleon transfer; at high energy: projectile and target fragmentation.

3. Central collisions: at low energy: fusion, compound nucleus reactions; at intermediate and high energy: shattering of the projectile and the target into light fragments and nucleons.

In this framework, projectile and target fragmentation reactions are the reactions that occur when the nuclei just begin to overlap and have relatively large velocities. From a physical standpoint, projectile and target fragmentation are the same process in complementary rest frames. However, the experimental techniques used in their study and their historical evolution have been quite different.

For more than three decades, a wealth of data has been accumulated for the production of fragmentation products from proton–nucleus collisions using high-energy proton beams. The target fragments produced by these interactions, usually called spallation products, were studied by radiochemical methods, and extensive systematics have been established [Gold 78, Hufn 85, Morr 89]. More than a decade ago, with the availability of relativistic energy heavy-ion beams (up to a few GeV/u), the field of high-energy projectile fragmentation was opened up. The main advantage of studying projectile rather than target fragmentation is that, while fragments originating from target break-up are slow-moving (and may be stopped in the target material), fragments from the projectile are fast-moving and can be easily studied by magnetic spectrometers.

A number of systematic measurements of production cross sections and momentum distributions of PLFs from light projectiles exist at high energies [e.g. Heck 72, Grei 75, Viyo 79]. A rather complete parametrization of the variations has been established and, several disparate models have been successful in describing the observations [e.g. Gold 74, Oliv 79, Morr 79, Frie 83, Sümm 90a]. In general, these models are based on the assumption of a two step process consisting of a fast collision step and a slow deexcitation one. On the other hand, at low energies (below 20 MeV/u), where heavy-ion beams have been available for about two decades, projectile-like products have also been observed, but the fragmentation mechanism is not operating, because of the low relative velocity of the nuclei [Bond 71, Gelb 78, McVo 80,

Egel 81, Murp 83, Home 84]. At such low energies, direct transfer, deep-inelastic and incomplete fusion reactions can take place during peripheral collisions of the projectile with the target nucleus.

Intermediate energy heavy-ion beams have become available only during the last few years and a few projectile fragmentation measurements have been performed in this energy region [e.g. Guer 83, Blum 86, Borr 86, Bazi 90]. However, the data obtained so far are not adequate to provide a systematic parametrization and a clear understanding of the transition region. Apart from characteristics similar to those observed at high energies, the data exhibit new features that may yield important information on the reaction mechanism of peripheral collisions (e.g. orbital deflection [Bibb 79, Silk 88]). Also, along with "pure" fragmentation channels (where nucleons are only removed from the projectile), nucleon transfer channels have been observed (where one or more nucleons have been picked-up by the projectile [e.g. Borr 86, Soul 91]). In addition, the only estimates of yields and momentum distributions are presently based on extrapolations of the high energy parametrizations for lack of a better method. For example, at the NSCL, estimates of production rates of secondary radioactive beams of PLFs separated by the A1200 are performed with the computer code "INTENSITY" [Wing 91], which is based on the parametrizations of Sümmerer and Morrissey [Sümm 90] of high-energy fragmentation reactions.

Therefore, in order to understand the reaction mechanisms operating in peripheral collisions at intermediate energies and obtain parametrizations of PLF distributions, additional refined measurements are necessary, mainly near $0^o$ (since the projectile-like isotopes are produced in a narrow cone about $0^o$). Such systematic data and parametrizations, apart from a nuclear reaction standpoint, will improve our predictive power to choose the proper energy and beam–target combinations to produce radioactive beams. Measurements of reaction products at $0^o$ are difficult in general,

because of the presence of the primary beam and require the use of magnetic spectrometers.

In this work, as a first attempt towards obtaining systematic data on intermediate-energy fragmentation, the results from a series of 0–degree measurements of projectile-like fragments from several beams produced by the K1200 Cyclotron at the NSCL are presented. The characteristics of the distributions of the PLFs are described and analysed with several theoretical models.

In chapter 2, a more detailed discussion of projectile fragmentation reactions is presented along with a description of models previously developed to interpret the observations. For two of the models, namely Goldhaber's model and Friedman's model, a derivation of the relevant equations is presented in appendix A.

In chapters 3 and 4, our measurements of projectile fragmentation distributions at the NSCL are described in detail. In chapter 3, the preliminary measurements performed with the interim K1200 beamline operated as a spectrometer are presented (a discussion of Beam Optics concepts and a derivation of the equations developed for the analysis of the data are given in appendix B). In chapter 4, the measurements with the recently commissioned A1200 beam analysis device (operated in a 0-degree spectrometer mode) are presented.

In chapter 5, the systematic variation of the centroids and the widths of the momentum distributions and the relative yields of the observed projectile-like fragments (both fragmentation and transfer products) are presented and compared with calculations performed using extended versions of the models presented in chapter 2.

Finally, in chapter 6, conclusions from the present study of intermediate–energy fragmentation reactions are summarized and areas for further investigation are mentioned.

# Chapter 2

# Projectile Fragmentation: Overview–Models

## I Introduction

In this chapter a detailed description of the projectile fragmentation process is presented and various models used to interpret the experimental results are discussed. In section II, the isotopic distributions of PLFs are discussed. Two high-energy models, the abrasion-ablation model and the intranuclear cascade model are described and their predictions are compared to high-energy fragmentation data. In addition, the features of the isotopic distributions of PLFs at lower energies are presented. In section III, the momentum distributions of PLFs are discussed. The characteristics of the momentum distributions at high-energies are first presented and two models (Goldhaber's model and Friedman's model) are described. Also, the features of the momentum distributions at lower energies are discussed, and various mechanisms involved in the production of PLFs at these energies are mentioned.

## II Isotopic Distributions

A large variety of fragments is produced by the fragmentation of a medium or heavy projectile. As an example, approximately 70 isotopes were identified between Z=8

and 16 from the fragmentation of $^{40}$Ar at 213 MeV/nucleon [Viyo 79]. In general, it has been found that for a given element, the variation of the cross section $\sigma(Z, A)$ with respect to A, called the isotopic distribution, is approximately Gaussian in shape; for elements close to the projectile, the centroids of the distributions are close to the N/Z ratio of the projectile, whereas for lighter elements the centroids correspond to isotopes closer to the valley of $\beta$-stability. Very little systematic data exist for projectile-fragmentation of heavy beams (A>40) and here one has to rely on radiochemical measurements of target fragments [e.g. Sümm 90a]. The general features of the distributions of fragments from these nuclei seem to be dominated by the effects of statistical deexcitation of primary fragments. Two basic models have been used to interpret the features of the isotopic distributions, one based on a macroscopic and the other on a microscopic description of the collision. These models are outlined below.

**Abrasion–ablation model**

The abrasion-ablation model [Bowm 73, Morr 78, Oliv 79] is a simple macroscopic, geometric model used to describe the isotopic distributions of target-like and projectile-like fragments from high-energy collisions. According to this model, projectile and target are taken to be spherical and the Coulomb deflection of the projectile trajectory is neglected (the deflection is very small because of the high relative velocity). For a peripheral collision with a given impact parameter, projectile and target nucleons which lie in the geometric overlap region interact strongly (participant nucleons), and are removed from the initial nuclei, whereas the other nucleons do not interact (spectator nucleons). This first step of the process, called abrasion, is fast because of the large relative velocity of projectile and target. The remaining spectator pieces, called primary fragments, are excited (it should be noted that no specific assumption concerning the fate of the removed parts of the projectile and the target

is necessary to describe projectile or target fragmentation). In the original model, the excitation energy of the primary fragments was assumed to originate from surface tension: the abraded primary fragment, having a "bite" on it, has an odd shape with a surface that is larger than that of a spherical shape of the same volume; the surface energy is given by the product of this "extra" surface times the nuclear surface tension coefficient (with a typical value of $\sim$ 1.0 MeV/fm$^2$) [Bowm 73]. Apart from the excitation energy due to surface tension, which could be considered as a lower limit, additional excitation energy can be deposited to the primary fragments by nucleon–nucleon collisions in the participant region; some nucleons, scattered out of this region, are directed towards the projectile and the target spectators, depositing part of their energy in the spectators by further nucleon–nucleon collisions [Oliv 79].

From the geometric character of the abrasion, the number of nucleons removed from the projectile $\alpha_P(b)$ can be calculated as a function of the impact parameter $b$ of the collision [e.g. see Morr 78]: $\alpha_P(b)$ is proportional to the overlap volume of the projectile (with mass $A_P$) and the target (with mass $A_T$), (see Fig. 2.1). From the function $\alpha_P(b)$, the cross section $\sigma(A_{PF})$ for the production of all primary fragments with mass $A_{PF}$ can be calculated. In order to calculate the cross section $\sigma(Z_{PF}, A_{PF})$ of a given primary isotope [$\sigma(Z_{PF}, A_{PF})$ is a fraction of the primary mass yield $\sigma(A_{PF})$], a model for the relative number of removed protons and neutrons from the nucleus has to be introduced. Several models concerning proton–neutron correlations will be described in a moment.

The excited primary fragments are then assumed to undergo deexcitation by statistical emission (evaporation) of nucleons (or light fragments). This evaporation step, called ablation, is slow compared to the abrasion and leads to the formation of the final fragments. In order to calculate the yields from the ablation step, standard evaporation codes have been used [e.g. Blan 76, Tass 91], which are based on

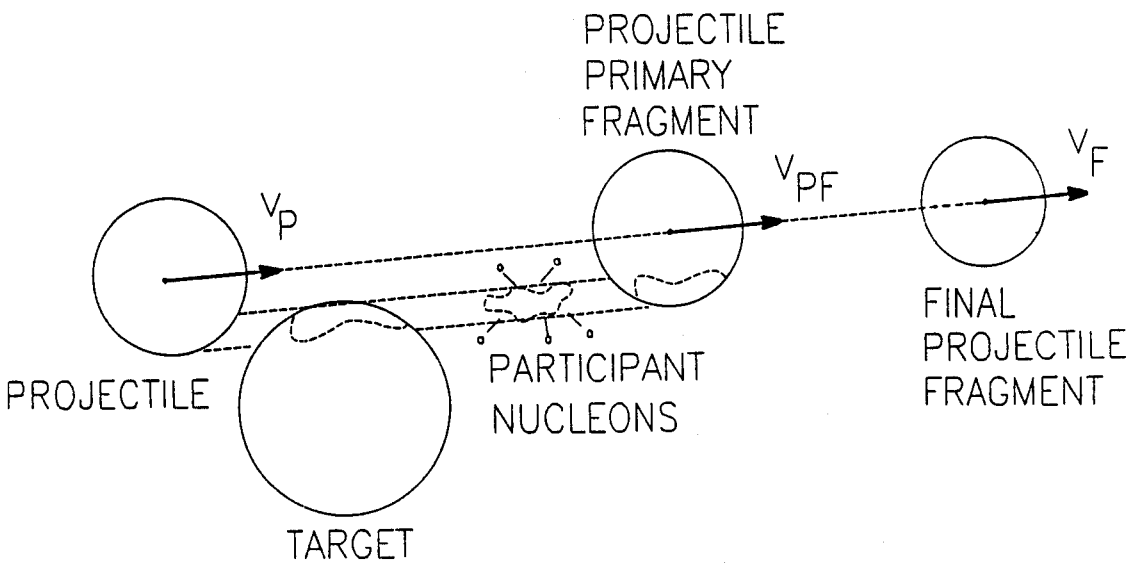


Figure 2.1: An abrasion–ablation picture of a peripheral collision. The collision between the projectile and the target shears off a part from both the projectile and the target. The excited primary fragments (spectators) undergo deexcitation by statistical emission of particles to produce the final (observed) fragments.

the statistical theory of the compound nucleus. Whether the highly excited primary fragments relax into a thermally equilibrated state implied by the compound nucleus model is open to debate. Calculations indicate that it is at least plausible and in fact likely [Harp 71]. It is the nature of the decay process that an ensemble of even a single primary fragment will generate numerous final fragments. Consequently, in order to calculate the production cross section of a given final fragment, all primary fragments leading to it have to be taken into account.

Fluctuations in the number of protons (or neutrons) in the primary fragment (or equivalently, in the abraded part of the projectile) must also be considered. Three different models describing these fluctuations in terms of the proton–neutron correlations in the projectile nucleus can be found in the literature:

Complete proton–neutron correlation. Under this assumption, the nucleus is taken to be "frozen" and therefore the proton-to-neutron ratio of the abraded part of the projectile is exactly equal to that of the projectile. Only one primary fragment nucleus corresponds to this situation, with cross section equal to $\sigma(A_{PF})$. This assumption has found limited application [West 76].

No proton–neutron correlation. Under this assumption, every abraded nucleon has a probability $Z_P/A_P$ to be a proton and $N_P/A_P$ to be a neutron. The probability $\mathcal{P}(Z_R, N_R)$ that the abraded part (with mass $A_R$) of the projectile has $Z_R$ protons and $N_R$ neutrons is given by a hypergeometric distribution:

$$\mathcal{P}(Z_R, N_R) = \frac{\binom{Z_P}{Z_R}\binom{N_P}{N_R}}{\binom{A_P}{A_R}} = \frac{\binom{Z_P}{Z_{PF}}\binom{N_P}{N_{PF}}}{\binom{A_P}{A_{PF}}} \tag{2.1}$$

where $Z_R = Z_P - Z_{PF}$, $N_R = N_P - N_{PF}$ and $A_R = A_P - A_{PF}$ are the number of protons, neutrons and nucleons, respectively, removed from the projectile and the

parentheses denote combinatorials, e.g. $\binom{Z_P}{Z_R} = Z_P!/[(Z_P - Z_R)!Z_R!]$. The cross section of a given primary fragment is the product of the probability $\mathcal{P}(Z_R, N_R)$ given by eq. (2.1) times the primary mass yield $\sigma(A_{PF})$. In general, this assumption can only describe the data when coupled to very high excitation energies of the primary fragments [Oliv 79], because it predicts wide primary isotopic distributions [Viyo 79].

Proton–neutron correlation arising from GDR vibrations. According to this model, the mean value of the ratio of the abraded neutrons to protons is equal to that of the projectile, and fluctuations in the number of abraded projectile protons (and neutrons) arise from giant dipole vibrations of the nucleus. The giant dipole resonance is a collective excitation mode of the nucleus in which, upon absorption of electric dipole radiation, the protons vibrate collectively against the neutrons. According to a macroscopic description given by Goldhaber and Teller [Gold 48], the protons and the neutrons behave like two separate rigid but interpenetrating density distributions and the resulting resonance consists of a harmonic displacement of these spherical distributions with respect to each other. Myers et al. [Myer 77] have presented a description of the GDR mode in terms of the macroscopic droplet model of the nucleus. This formulation was used by Morrissey et al. [Morr 78], to describe the proton–neutron correlations during the abrasion step of fragmentation reactions. According to this treatment, the production cross section $\sigma(Z_{PF}, A_{PF})$ of a primary fragment is related to the mass yield $\sigma(A_{PF})$ by a Gaussian distribution:

$$\sigma(Z_{PF}, A_{PF}) = \frac{1}{\sqrt{2\pi\sigma_Z^2}} e^{-\frac{(Z_{PF}-Z_{PF,0})^2}{2\sigma_Z^2}} \sigma(A_{PF}) \tag{2.2}$$

where the centroid $Z_{PF,0}$ of the primary charge distribution is determined by the projectile $Z_P/A_P$ ratio: $Z_{PF,0} = A_{PF}\frac{Z_P}{A_P}$. Notice that this value for the centroid $Z_{PF,0}$ is the same as the prediction of the complete correlation model for $Z_{PF}$. The width $\sigma_Z$ of the charge distribution is calculated from eqs. 15–17 of [Morr 78]. The predictions

of this model for the widths of the isotopic distributions lie, as expected, between the previous two limiting cases. The model has been successful in describing the isotopic distributions of the projectile fragmentation products from the reaction $^{40}$Ar(213 MeV/u) + C [Viyo 79]. However, comparisons with limited target fragmentation data from heavy targets [Morr 80] and also recent projectile fragmentation data from heavy beams ($A$ >40) [Stép 91] have been less satisfactory.

### Intranuclear cascade model

The intranuclear cascade (INC) model is a microscopic model in which the projectile and target are considered to be made up of (nearly) independent nucleons confined in spherical potential wells. The production of projectile fragments also occurs in a two-step process. During the first (fast) step, the motion of the potential wells past one another leads to individual nucleon-nucleon collisions. The result of these collisions is the formation of excited primary fragments. In the second (slow) step, the primary products deexcite by statistical evaporation, leading to the formation of the final fragments. Thus, the intranucler cascade model includes exactly the same second step as the abrasion–ablation model, but importantly, it differs in the description of the first step, namely the production of primary fragments.

From a calculational point of view, the INC model is implemented as a Monte Carlo simulation of simultaneous nucleon–nucleon (N–N) scatterings. The principal physical information required for an INC calculation is the free N–N scattering cross section [Chen 68]. This cross section, which is usually taken from experimental data, is energy and isospin dependent, as illustated in Figure 2.2 [Harv 85]. We notice that, at intermediate energies, the proton–neutron scattering cross section ($\sigma_{pn}$) is approximately three times larger than the proton–proton or the neutron–neutron scattering cross sections ($\sigma_{pp}$ and $\sigma_{nn}$, respectively). However, at high energies (>500 MeV/u), $\sigma_{pn}$ becomes approximately equal to $\sigma_{pp}$ or $\sigma_{nn}$.

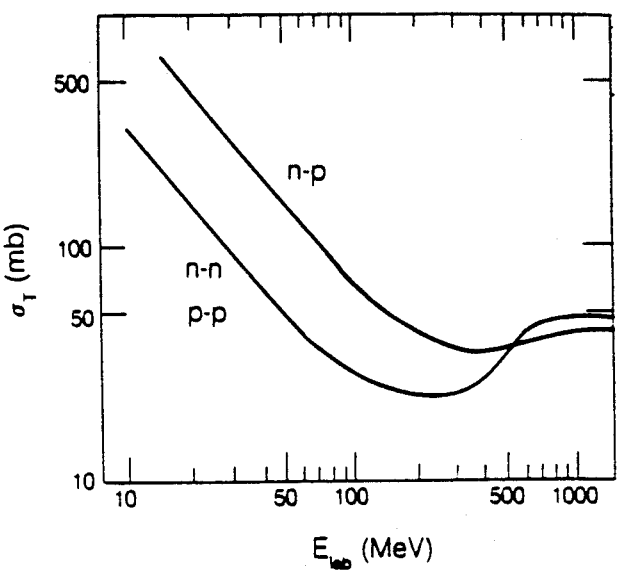


Figure 2.2: The total nucleon–nucleon scattering cross sections [Harv 85]. At intermediate energies, $\sigma_{pn}$ is $\sim$3 times larger than $\sigma_{pp}$ or $\sigma_{nn}$; this difference almost disappears at high energies (>500 MeV/u).

At the beginning of the calculation, both projectile and target nuclei are considered as noninteracting Fermi spheres; during the collision step, random N–N scattering is allowed to occur in the overlap region which removes nucleons from the projectile and the target, creating excited primary fragments. The excitation energy of these fragments originates from the "holes" which cascade nucleons leave in the volume of the projectile or target remnant or from nucleons trapped in the remnant. Subsequently, the excited primary products deexcite by statistical evaporation.

One of the most well known INC codes is the "VEGAS" code, originally developed by Chen et al. for proton–nucleus collisions [Chen 68] and later generalized to relativistic heavy-ion collisions by Yariv and Fraenkel [Yari 79]. This latter code, called "ISABEL", takes into account, along with the Fermi motion of the nucleons inside the colliding nuclei, the effects of the Pauli principle on the nucleon motion and the nucleon–nucleon scattering.

The "ISABEL" code has been used to describe projectile fragmentation data [Morr 79] for the reaction $^{40}$Ar(213 MeV/u) + C [Viyo 79], along with a correlated abrasion–ablation model. The predictions of the INC model for the primary fragments are different from those of the abrasion–ablation model. Specifically, the range of mass removed from the projectile (and the target) is lower, the excitation energy of the primary fragments is higher and the primary isotopic distributions are wider than those predicted by the abrasion–ablation model. However, after the deexcitation step, the final fragment distributions are rather similar, with noticeable differences only for fragments very close to the projectile. In Figure 2.3, the measured isotopic distributions of O, F and Ne isotopes from the reaction $^{40}$Ar(213 MeV/u) + $^{12}$C are shown, along with the predictions of both the INC model and the abrasion–ablation model [Morr 79]. We notice that both models agree with the trend of the data equally well and cannot be differentiated by these data. No measurements for this reaction

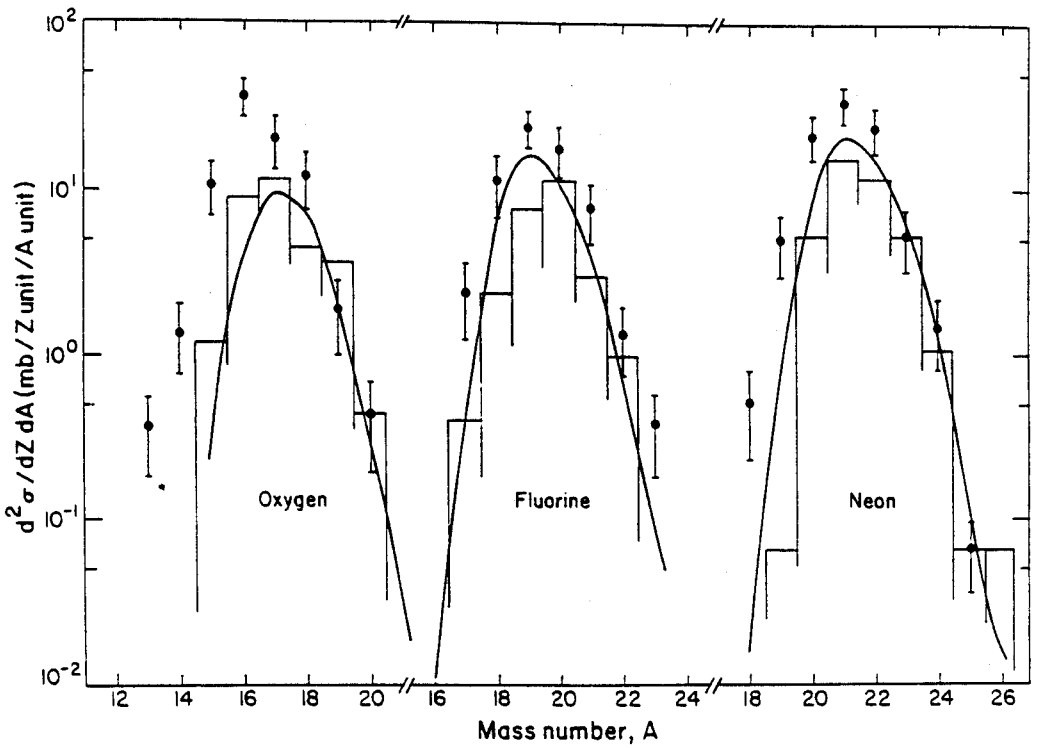


Figure 2.3: A comparison of the calculated production cross sections (using the abrasion–ablation model and the intranuclear cascade model) with the measured data from the fragmentation of $^{40}$Ar(213 MeV/u). Solid curve: abrasion-ablation model, histograms: INC model, solid points: data [Morr 79].

are available for near-projectile fragments, where the predictions of the two models are slightly different.

Up to the present, relatively few detailed measurements on production cross sections of fragments from relativistic projectiles exist in the literature. Apart from the measurements of $^{40}$Ar residues, careful measurements of fragments from the relativistic light ions $^{14}$N, $^{12}$C and $^{16}$O have been performed [Heck 72, Grei 75]. Also another important measurement has been performed on the elemental cross sections (charge distributions) of fragmentation products of relativistic $^{56}$Fe projectiles [West 79]. Very recently, a detailed measurement of cross sections and momentum distributions of projectile fragments from the reaction $^{84}$Kr(200 MeV/u) + $^{197}$Au has been performed [Stép 91], along with calculations with the correlated abrasion–ablation model [Morr 79] and the intranuclear cascade model [Yari 79]. For this heavy projectile, the abrasion–ablation model gave a poor description of the isotopic distributions of fragments near the projectile. This was attributed to an underestimation of the excitation energy of the primary fragments (taken, as usual, to be the excess surface energy of the abraded projectile). However, calculations with the INC model were found to be in good agreement with the measured isotopic distributions. Therefore, the magnitude of the excitation energy of the primary products predicted by the INC model was consistent with the data. In addition to the isotopic distributions, the INC model gave good predictions of the centroids and the widths of the fragment momentum distributions (see also section III).

An interesting characteristic of high energy projectile fragmentation is that the relative yields of projectile fragments are independent of the target [e.g. see Olso 81, Olso 83]. This means that, for a given projectile, the variation of fragment cross sections with target mass is given only by a single factor. This property of the cross sections, referred to as "factorization", reflects the geometrical character of

high energy peripheral collisions.

Some of the features of the distributions of high-energy fragmentation cross sections are also observed in the intermediate energy region, along with new ones. A limited number of measurements of isotopic distributions have been made in this energy region; e.g. reactions with $^{40}$Ar projectiles at 44 and 27 MeV/u on various targets [Guer 83, Rami 84, Rami 85, Blum 86, Borr 86] and also reactions with $^{86}$Kr(44 MeV/u) projectiles on various targets [Bazi 90]. The isotopic distributions of fragments far in mass from the projectile are similar to those observed at high energies, approximately having a Gaussian shape and a width which is independent of the target. However, the isotopic distributions of near-projectile fragments are slightly shifted towards the neutron rich side when neutron-rich targets are used (see Figure 2.4).

It has been pointed out by Borrel et al. [Borr 86] that the target effect is related only to the neutron excess of the target and not to its size: in the reactions of $^{40}$Ar(44 MeV/u) with the neutron rich targets $^{64}$Ni and $^{103}$Rh (both having the same $N/Z$ ratio, but different size), the relative yields of the observed near-projectile fragments were the same. This effect can be qualitatively understood, if we assume that the removal of nucleons from the projectile occurs only through individual nucleon–nucleon collisions with the target and, in addition, we take into account the energy dependence of the N–N scattering cross sections (see Fig. 2.2). In the intermediate energy region, we expect that protons from the projectile are more likely than neutrons to be scattered from target nucleons, if a neutron rich target is used. Therefore, the projectile fragments tend to be proton-defficient, that is, neutron-rich. At higher energies (>500 MeV/u) however, where the nucleon–nucleon cross sections are all similar, the $N/Z$ ratio of the target will have no effect to the isotopic distributions of the fragments.

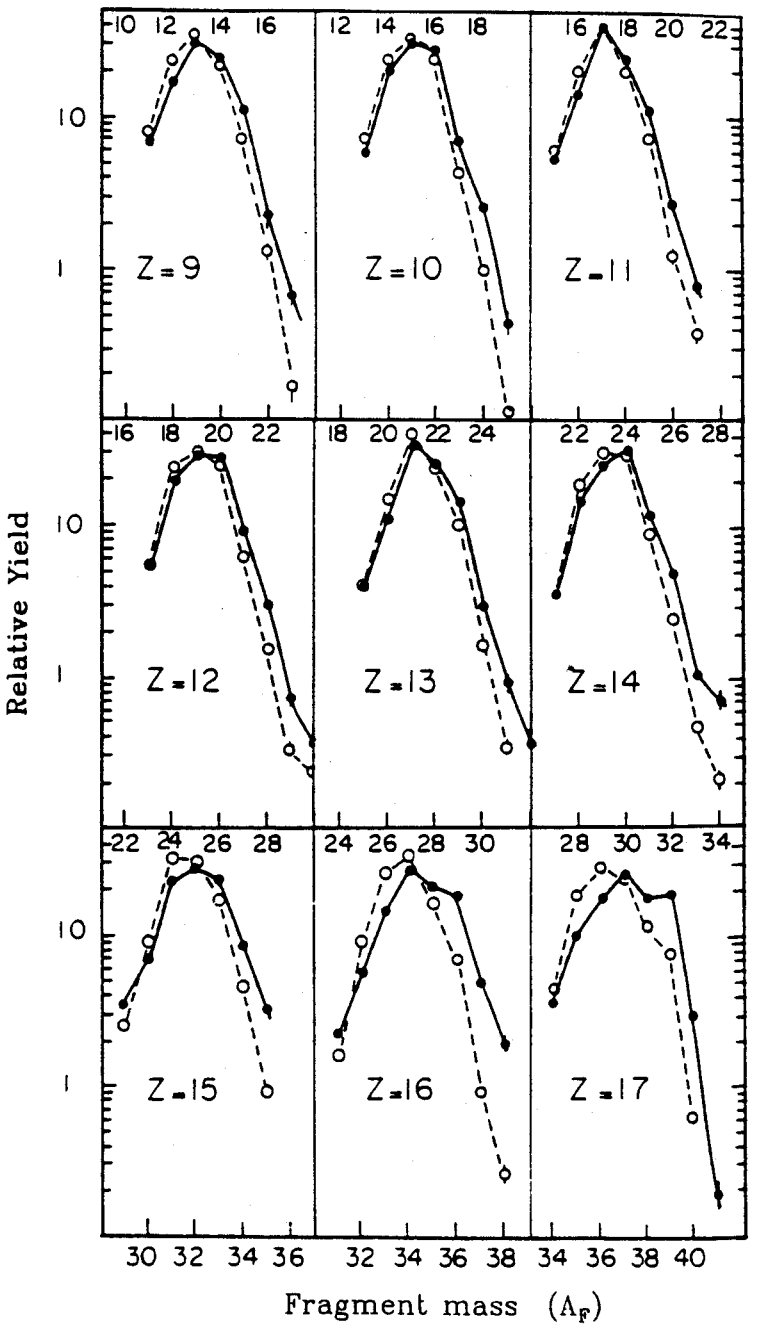


Figure 2.4: A comparison of experimental isotopic yields for the reactions of $^{40}$Ar(44 MeV/u) projectiles with $^{58}$Ni target (open circles) and $^{197}$Au target (closed circles) [Guer 83]. Near projectile elements, as S and Cl, exhibit wider isotopic distributions on their neutron rich sides for the more neutron rich $^{197}$Au target than for the $^{58}$Ni target.

Another new feature of intermediate energy "fragmentation" is the production of PLFs resulting from a net nucleon transfer (pick-up or exchange) between the projectile and the target (see also Fig. 2.4). Consequently, in this energy regime a nucleon transfer mechanism is present, along with the "pure" fragmentation mechanism.

At low energies, where a substantial number of measurements has been performed [e.g. Gelb 78, Egel 83], the isotopic distributions of PLFs reflect the characteristics of a composite nuclear system formed by a partial fusion of the projectile with the target [Bond 71, Home 84]. It has been shown that the relative isotopic yields of PLFs produced at low energies depend exponentially on the ground-state-to-ground-state $Q$-value, $Q_{gg}$, of the two-body rearrangement reaction leading to a given fragment [Bond 71]. Thus, the reaction mechanism of peripheral collisions at low energies is completely different from that at high energies. At low energies (<20 MeV/u), the relative projectile–target velocities are smaller than the mean velocity of nucleons inside the nuclei (the mean nucleon velocities due to Fermi motion are $\sim 0.2c$) and therefore, the collision times are longer than the transit time for nuclear dimensions. Because of the long collision times, a partially equilibrated dinuclear system can be formed. Nucleon exchange between projectile and target can occur during the interaction stage. Thus, the average $N/Z$ of the PLFs can be seriously affected by the $N/Z$ of the target. Such a behaviour is not observed at high energies, because of the high relative velocities (e.g. $v \simeq 0.9c$ for $E/A \simeq 2.0$ GeV) and, consequently, the sudden "clean-cut" character of the collision.

At intermediate energies, however, the reaction mechanism exhibits some features of both high and low energy mechanisms. At these energies, direct nucleon transfer and/or deep-inelastic (partial equilibrium) mechanisms compete with the "sudden" fragmentation mechanism.

It should be pointed out that a very important question, concerning the production

of projectile-like fragments is the magnitude and the source of excitation energy imparted to the primary spectator nuclei (primary fragments). Predictions of this energy are model dependent and still open to debate. The very broad momentum distributions and the relative proton-excess of TLFs from heavy targets [Morr 80, Sümm 90a] and PLFs from heavy projectiles ($A$ >40) [Bazi 90, Stép 91] imply that the excitation energies of the primary fragments are high and rather long deexcitation chains lead to the observed fragment distributions. As already mentioned, it has been shown that the INC model correctly accounts for the excitation energy of the primary products [Stép 91]. On the other hand, measurements of PLF distributions from lighter projectiles at intermediate energies [Gelb 78, Guer 83, Blum 86, Borr 86] seem to indicate that the excitation energy of the projectile primary fragments remains surprisingly low, consistent with a rather "cold" break-up (or pick-up) mechanism [Home 84, Harv 85].

Valuable information on the excitation energy spectrum of primary fragments can also be obtained from exclusive measurements. There are only a few measurements of this type in the literature. Measurements of charged particles in coincidence with PLFs for the systems $^{20}$Ne + $^{197}$Au at 11 and 17 MeV/u [Stok 84] and $^{16}$O(16 MeV/u) + CsI [Murp 83a] have shown very low charged particle multiplicities in coincidence with PLFs, implying very low primary fragment excitation energies at low bombarding energies. Also, recent neutron multiplicity measurements on the reaction $^{40}$Ar + $^{197}$Au at 27.2 MeV/u [Morj 88] have shown that very large excitation energies are found in the target-like fragments. In addition, a comparison of the average neutron multiplicities from reactions with Ar and Kr projectiles at 35 MeV/u on various targets [Gali 88] have shown that the Kr projectile induces 50% higher neutron multiplicities, implying that more excited primary fragments are formed when using a heavier projectile.

# III Momentum Distributions

In addition to the isotopic distribution, another characteristic of projectile-like fragments that contains important information on the reaction mechanism is the momentum distribution. At high energies, systematic measurements of momentum distributions have been performed for the fragmentation products of relativistic $^{12}C$ and $^{16}O$ projectiles [Grei 75] and for the products of $^{40}Ar$(213 MeV/u) [Viyo 79] and $^{84}Kr$(200 MeV/u) [Stép 91] projectiles, whose isotopic distributions were discussed in the previous section. As an example, the momentum distribution of $^{10}Be$ isotopes from the fragmentation of $^{12}C$ at 2.1 GeV/u is shown in Fig. 2.5a.

In general, the momentum distributions are well represented by Gaussian functions centered at velocities near (slightly lower than) that of the projectile, and have widths following a parabolic dependence on the fragment mass: $\sigma^2 \propto A_F(A_P - A_F)$, where $A_P$ and $A_F$ are the mass numbers of the projectile and fragment respectively (e.g. see Fig. 2.5b). Deviations from this behaviour have been observed in fragmentation studies of heavy projectiles [Stép 91] and heavy targets [Morr 89]: the momentum distributions of fragments far in mass from the parent nuclei are wider than predicted by the parabolic parametrization (see also Fig. 2.6).

The longitudinal (or parallel) momentum distributions were found to be independent of the target and the bombarding energy. Transverse momentum distrubutions were also measured for $^{12}C$ and $^{16}O$ fragmentation and their widths were found to be equal to the widths of the corresponding parallel distributions within 10%.

A small downshift in velocity (relative to the beam velocity) of the centroids of the fragment momentum distributions has been observed. This downshift increases with the number of nucleons removed from the projectile and has been interpreted as a "friction" phenomenon: in order to remove bound nucleons from the projectile,

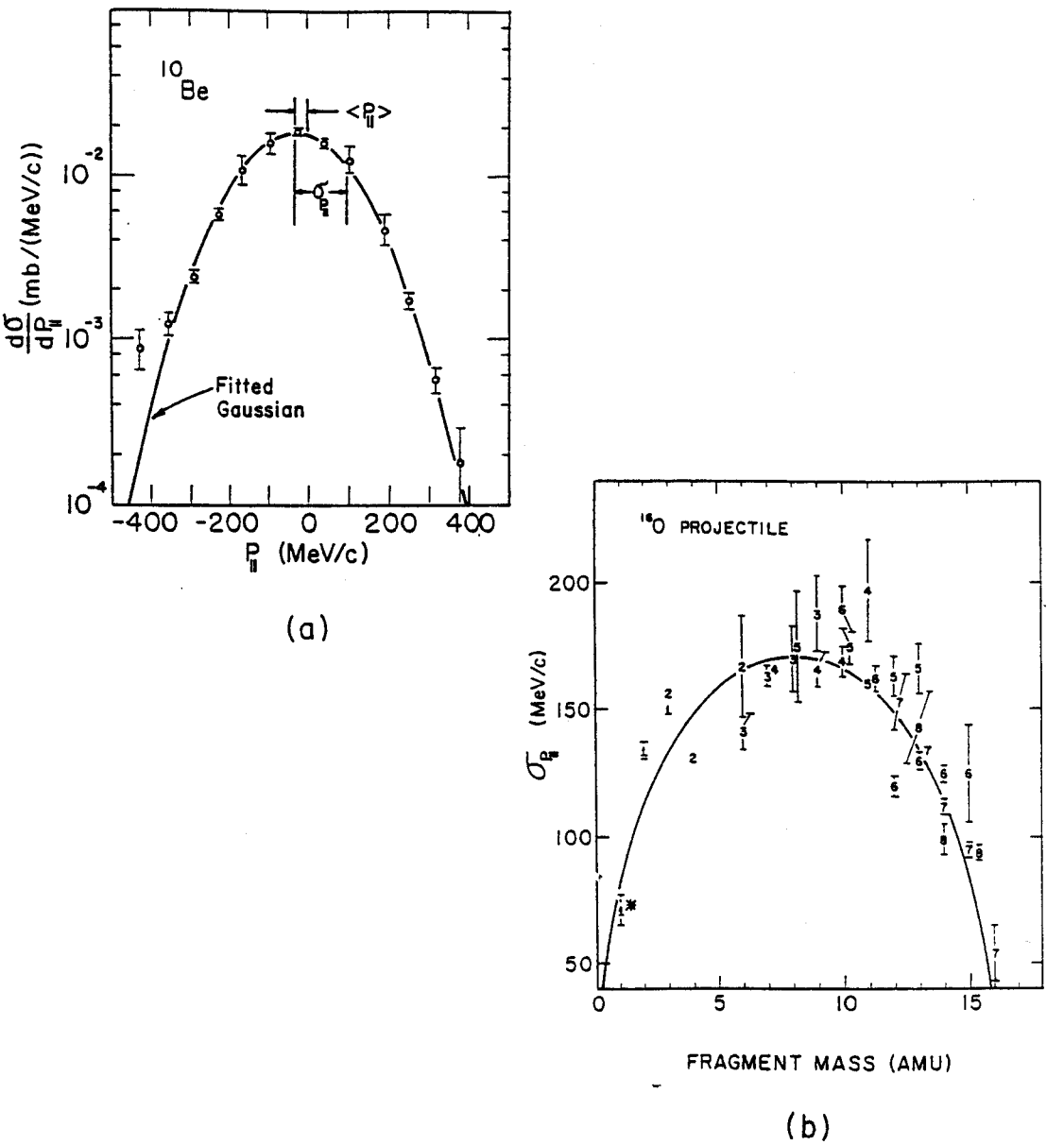


Figure 2.5: a) The parallel-momentum distribution of $^{10}$Be fragments from the reaction of a $^{12}$C projectile at 2.1 GeV/u on a Be target. The distribution is expressed in the projectile rest frame. A Gaussian function is fitted to the data points. The average momentum and the width of the fitted distribution are indicated [Grei 75]. b) Dependence of the parallel-momentum distribution widths on the fragment mass. The data are from the fragmentation of $^{16}$O at 2.1 GeV/u [Grei 75]. The plotted symbols indicate the atomic number Z of the fragments. The parabola represents the best fit to the data and has a reduced width $\sigma_0 = 83 \pm 1$ MeV/c.

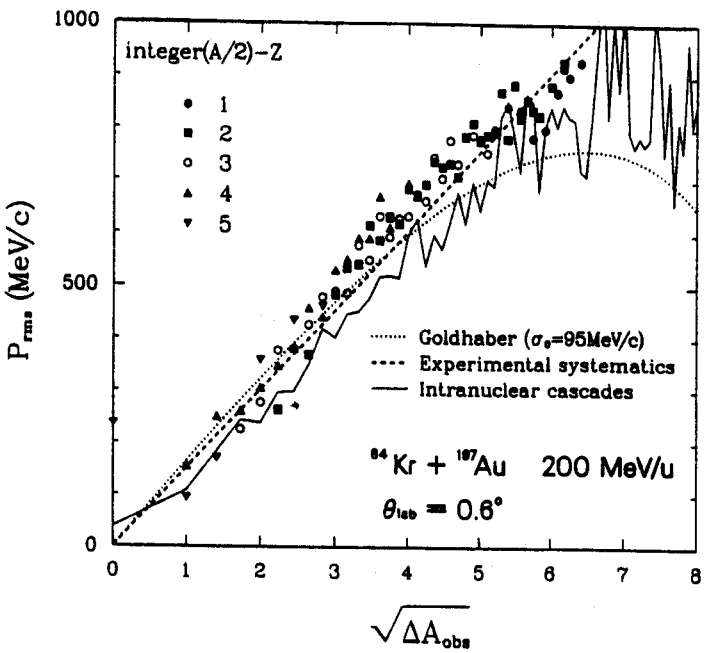


Figure 2.6: The total-momentum dispersion $P_{rms}$ of projectile fragments as a function of the square root of mass loss ($\Delta A$) from the reaction $^{84}$Kr (200 MeV/u) + $^{197}$Au [Stép 91]. ($P_{rms} = \sqrt{3}\sigma_{||}$, under the assumption of isotropy, see text.) Two model calculations are shown: Goldhaber's model (thin dotted line) and intranuclear cascade model (solid line). Fragments far in mass from the projectile ($\Delta A > 25$) have momentum dispersions larger than predicted by Goldhaber's model. For these fragments, the considerable fluctuations in the INC calculation are essentially statistical.

energy has to be consumed. This energy is assumed to come from the projectile kinetic energy and consequently, the resulting fragment has, on average, lower velocity than that of the initial projectile. In order to calculate the fragment average velocity according to this "friction" concept, a picture of the way the nucleons are stripped from the projectile has to be introduced. For this purpose, two different assumptions are discussed below. First, the nucleons are assumed to be stripped from the projectile one after the other [with an average of $E_{s,n} \simeq 8$ MeV (for medium and heavy nuclei) required for each removal]. Second, the nucleons are assumed to be removed from the projectile simultaneously as a single (bound) cluster $R$, thus creating the observed fragment $F$. The energy required in this case is equal to the separation energy of the projectile into the clusters $F$ and $R$. Both these simple assumptions give predictions in agreement with the trend of the high energy fragmentation data and correspond, respectively, to an independent-particle description of the fragmenting projectile nucleus, and to a cluster structure description (see below the discussion of Goldhaber's model and Friedman's model, respectively).

In order to interpret the origin and the variation of the widths of the PLF momentum distributions, two simple models, Goldhaber's statistical model and Friedman's peripheral model, each based on a different description of the projectile nucleus, are discussed below.

**Goldhaber's Model**

This model [Gold 74] is an independent-particle description of the projectile nucleus: the nucleus is considered as a spherical potential well in which the nucleons move independently. It is assumed that the only correlation between the nucleons arises from momentum conservation; the nucleons inside the projectile have some distribution of momenta that, at any time, gives a total momentum of zero in the rest frame of the projectile. Consequently, if one part of the projectile is removed by a

rapid interaction with the target, it carries away its relative momentum and, because of momentum conservation, the remaining fragment recoils with an opposite momentum. Assuming isotropy of the internal momenta of the nucleons in the projectile, the recoil momentum distribution of the fragments, projected on a given coordinate axis, is a Gaussian distribution. The width of the distribution can be related to the fragment mass, if either of the following two assumptions is made:

Sudden fragmentation hypothesis: a part is suddenly removed from the projectile by the interaction with the target. This assumption suggests a process similar to the first step (abrasion) of the abrasion-ablation model (but here an ablation step is missing). It has been shown by Goldhaber that conservation of momentum leads to the following relation for the width:

$$\sigma^2 = \sigma_0^2 \frac{A_F(A_P - A_F)}{A_P - 1} \quad . \tag{2.3}$$

where the parameter $\sigma_0$, called the reduced width, is related to the nucleon momenta in the projectile by the expression:

$$\sigma_0^2 = \frac{\langle p_n^2 \rangle}{3} \tag{2.4}$$

where $\langle p_n^2 \rangle$ denotes the average-square momentum of the nucleon motion.

Assuming a Fermi-gas distribution of the nucleon momenta in the projectile, we have:

$$\langle p_n^2 \rangle = \frac{3}{5} p_{Fermi}^2 \tag{2.5}$$

where $p_{Fermi}$ is the Fermi momentum. Inserting this expression of $\langle p_n^2 \rangle$ into eq. (2.4), the reduced width is related to the Fermi momentum of the nucleon motion according to:

$$\sigma_0^2 = \frac{p_{Fermi}^2}{5} \tag{2.6}$$

Consequently, according to the sudden fragmentation hypothesis, the observed Gaussian distributions are directly related to the Fermi motion of the nucleons in the projectile.

The nucleon Fermi momentum $p_{Fermi}$ can be obtained experimentally by quasielastic electron scattering [Moni 71]. It has shown by Moniz et al. that $p_{Fermi}$ increases from the lighter to the heavier nuclei up to nickel ($A = 58$), where a value $p_{Fermi} \simeq 260$ MeV/c was obtained. This increase of $p_{Fermi}$ with mass is expected because $p_{Fermi}$ is related to the nuclear matter density $\rho = A/V$ according to the equation [see e.g. Path 72]:

$$p_{Fermi} = \left(\frac{3}{8\pi}\right)^{1/3} h \left(\frac{\rho}{2}\right)^{1/3} \tag{2.7}$$

where $h$ is Plank's constant and it has been assumed that $N = Z = A/2$ and also that $p_{Fermi}$ is the same for protons and neutrons. The nuclear density is known to increase with mass until it becomes roughly constant for heavier nuclei; this behaviour is a reflection of "saturation" of the nuclear forces [e.g. see Blat 52]. Expression (2.7) provides another way to obtain $p_{Fermi}$: from measurements of the nuclear matter density (e.g. via elastic electron scattering). For heavy nuclei, a typical value of $\rho$ is $\sim 0.17$ nucleons/fm$^3$; with this value, eq. (2.7) gives $p_{Fermi} \simeq 270$ MeV/c. This result is in good agreement with the values obtained from quasielastic electron scattering data.

In Table 2.1, the experimentally obtained values of the reduced width $\sigma_0$ from the fragmentation of relativistic $^{12}$C, $^{16}$O and $^{40}$Ar projectiles are listed. Also, the corresponding "theoretical" values of $\sigma_0$ are calculated using eq. (2.6), where the values of $p_{Fermi}$ from Moniz et al. [Moni 71] are used.

From this table, we notice that the measured reduced widths increase with increasing projectile mass (as the nuclear Fermi momentum does) and, interestingly, they

Table 2.1: Comparison of the experimentally obtained reduced widths from the fragmentation of relativistic projectiles [Grei 75, Viyo 79] with the theoretical values obtained from eq. (2.6), where for the Fermi momentum $p_{Fermi}$, the values reported by Moniz et al. [Moni 71] have been used.

| Projectile | $E(MeV/u)$ | $\sigma_{0,exp}$ | $\sigma_{0,theo}$ | $p_{Fermi}$ |
|---|---|---|---|---|
| $^{12}C$ | 2100 | $81 \pm 2$ | 99 | 221 |
| $^{16}O$ | 2100 | $83 \pm 1$ | 103 | 230 |
| $^{40}Ar$ | 213 | $94 \pm 5$ | 112 | 251 |

are always smaller than those calculated using the Fermi momentum values. This discrepancy can be understood if we recall that Goldhaber's independent-particle model ignores all correlations between nucleons, beyond the purely kinematical ones. It has been shown by Bertsch [Bert 81] that the Pauli exclusion principle between identical nucleons reduces the widths of the observed momentum distributions. A qualitative interpretation of this result is that a large anticorrelation between the momenta of two identical nucleons is expected when they are found close together in coordinate space.

Thermodynamic equilibrium hypothesis: in this second fragmentation picture, the projectile, after interaction with the target, is assumed to be in a highly excited state at thermodynamic equilibrium. The excited projectile decays into two fragments by a statistical break-up process. This process is similar to the second step (ablation) of the abrasion-ablation model, but here the the abrasion step is missing. In this case, conservation of momentum leads to the same relation between the width and the fragment mass, eq. (2.3), but the reduced width is now related to the excitation temperature $T$ of the projectile at the moment of its statistical decay:

$$\sigma_0^2 = m_n k T \frac{A_P - 1}{A_P} \tag{2.8}$$

where $m_n$ is the nucleon mass and k is the Boltzmann constant. Furthermore, the

excitation energy of the nuclear Fermi gas is related to its temperature with the following equation:

$$E^* = a(kT)^2 \tag{2.9}$$

where $a$ is a level density parameter, empirically expressed as: $a = A_P/(8\ \text{MeV})$. Thus, the excitation energy per nucleon of the projectile can be expressed as:

$$\epsilon^* = \frac{E^*}{A_P} = \frac{(kT)^2}{8\ \text{MeV}} \tag{2.10}$$

Inserting a typical value of $\sigma_0 \simeq 90$ MeV/c into eq. (2.8), we get $kT \simeq 8$ MeV, which gives, according to eq. (2.10), $\epsilon^* \simeq 8$ MeV. This value of the excitation energy per nucleon is comparable to the average binding energy per nucleon ($\sim 8$ MeV) of the projectile, implying that the projectile has some probability to disintegrate into nucleons. Thus, taking into account the experimental fact that bound fragments are abuntantly produced in a fragmentation reaction, the formation of a highly excited projectile in thermodynamic equilibrium should be considered as an extreme case.

It should be pointed out that in both fragmentation models, the variation of the widths of the momentum distributions with mass loss is a result of momentum conservation. Between these two extreme cases, these is a third possibility, that of a long evaporation chain, which also leads to the same result. Consequently, the widths of the momentum distributions cannot distinguish between a fast nucleon-removal process and a slower equilibration process, therefore they are insensitive to the speed of the fragmentation process. In order to obtain information about the course of the fragmentation reaction, the isotopic distributions of PLFs along with correlations among PLFs and light particles should be investigated in detail.

Goldhaber's model has been successful in describing the experimental parallel momentum distributions also at lower energies (e.g. fragmentation of $^{40}$Ar at 44 and 27 MeV/u [Blum 86, Borr 86]). However, the behaviour of the transverse momentum

distributions of fragments from intermediate energy projectiles is more complicated. Measurements on the fragmentation of $^{16}O$ projectiles in the 100 MeV/nucleon region have provided evidence that the isotropy observed at high energies is not present at these energies. The transverse momentum distributions of the observed fragments are wider than the parallel distributions. This effect is attributed to orbital deflection of the projectile by the combined Coulomb-nuclear field of the target before fragmentation takes place [Bibb 79, Silk 88, Brad 88]. It has been shown by Bibber et al. [Bibb 79] that including orbital deflection to Goldhaber's model leads to an expression for the width of the transverse momentum distribution of the form:

$$\sigma^2 = \sigma_0^2 \frac{A_F(A_P - A_F)}{A_P - 1} + \sigma_1^2 \frac{A_F(A_F - 1)}{A_P(A_P - 1)} \tag{2.11}$$

where $\sigma_0$ is the reduced width due to the intrinsic nucleon motion and $\sigma_1^2 = \frac{1}{2}\langle p_{A\perp}^2 \rangle$ is the variance of the transverse momentum $p_{A\perp}$ of the projectile due to orbital deflection at the moment of fragmentation. Typical values of the parameters $\sigma_0$ and $\sigma_1$, obtained from the $^{16}O$ data, were $\sigma_0 \simeq 80$ MeV/c and $\sigma_1 \simeq 200$ MeV/c [Bibb 79].

Another important feature of the momentum distributions of PLFs produced at intermediate and low energies is the existence of a long tail on the low-energy side of the peak, which has been attributed to the presence of dissipative mechanisms [Blum 86, Borr 86]. When applying Goldhaber's model to describe these data, the tail is excluded from the Gaussian fit.

A compilation of the best fit values of the reduced width parameter $\sigma_0$ obtained from the analysis, within the framework of Goldhaber's model, of existing fragmentation data at high and low energies has been reported by Murphy and Stokstad [Murp 83, Stok 85]. For energies down to ~40 MeV/u, a rather constant behaviour of $\sigma_0$ with energy has been observed, indicating the essential validity of Goldhaber's model. However, at lower energies, a decrease of the reduced width $\sigma_0$ (and also of the

"unreduced" width $\sigma$) with energy has been observed. This has been attributed to the dominance of a direct nucleon-transfer mechanism over the "sudden" fragmentation mechanism. Using a local-momentum plane-wave Born approximation (LM-PWBA) model, McVoy and Nemes [McVo 80] showed that such a narrower width is expected for the transfer component of the momentum distribution than for the fragmentation component. In a transfer reaction, the particle is transfered to a definite final state due to momentum and angular momentum conservation; this imposes strong constraints on the available phase space of the exit channel of the reaction and thus leads to a narrower momentum distribution of the observed fragment. Such strong constraints do not exist in a fragmentation reaction.

It should be noted that Goldhaber's model uses only the average (statistical) properties of the nucleons inside the projectile. The detailed nuclear structure of the projectile is completely ignored. More recently, a simple quantum mechanical model has been proposed by Friedman [Frie 83] in which, in addition to the average properties of the projectile nucleons, the nuclear structure is considered in a simple way in the calculation of the momentum distribution widths and the yields of projectile fragments. This model is discussed below.

**Friedman's Model**

This model considers the probability that a part $R$ to be removed from the projectile, preexists as a (single) cluster in the projectile before fragmentation. This cluster is stripped from the projectile upon interaction with the target and a final fragment $F$ remains from the projectile and is observed. In this picture, in contrast to Goldhaber's model, the nucleons removed from the projectile are not independent, but they are strongly correlated in space to form a cluster (with given binding energy) near the surface of the projectile.

The relative motion of the cluster $R$ with respect to the fragment $F$ inside the projectile is described by a radial wave function $\psi_{F-R}(r)$ which, near the nuclear surface, can be written as:

$$\psi_{F-R}(r) \propto \frac{e^{-\alpha r}}{r} \tag{2.12}$$

where $\alpha$ is the wave-number of the relative motion:

$$\alpha = \frac{1}{\hbar}\sqrt{2\mu E_s} \tag{2.13}$$

where $\mu$ is the reduced mass of the system $F$–$R$, $\mu = A_F(A_P - A_F)/A_P$, and $E_s$ is its separation energy.

The parallel momentum distribution of the observed fragment, determined by the Fourier transform of the cluster wave function $\psi_{F-R}(r)$, is a Gaussian distribution (centered at a velocity equal to that of the projectile, as in Goldhaber's model) with a width $\sigma$ given by:

$$\sigma^2 = \hbar^2 \frac{\alpha}{2x_0}\left(1 + \frac{1}{\alpha x_0}\right) \tag{2.14}$$

where $x_0 = 1.2A_F^{1/3}$ is the radius of the fragment. If the Coulomb interaction between the fragment $F$ and the removed part $R$ is taken into account in the wave function $\psi_{F-R}(r)$, the width has been shown to be:

$$\sigma^2 = \hbar^2 \frac{\alpha}{2x_0}\left(\sqrt{1+y} + \frac{1}{\alpha x_0}\right). \tag{2.15}$$

where $y = (b_c/x_0)/E_s$ is the ratio of the Coulomb energy of the system $F$–$R$ at the "touching" point (at $r = x_0$) to the separation energy $E_s$; $b_c$ is the Coulomb parameter of the system $F$–$R$, $b_c = e^2 Z_F Z_R$. Equation (2.15) shows that the Coulomb interaction between the fragment and the removed part results in a small increase of the width of the parallel momentum distribution of the fragment. This effect is not present in the simpler independent-particle model.

According to Friedman's model, the production cross section or the yield $\gamma_F$ of a given fragment $(Z_F, A_F)$ from the projectile $(Z_P, A_P)$ can be written as:

$$\gamma_F \propto S(Z_R, A_R) \frac{e^{-2\alpha x_0 b}}{x_0^3(1-b)}. \tag{2.16}$$

where the factor $S(Z_R, A_R)$ expresses the relative probability that the removed part $R$ of the projectile contains $Z_R$ protons and $N_R = A_R - Z_R$ neutrons and is expressed by the hypergeometric distribution, eq. (2.1); the second factor of this equation is the square modulus (evaluated at $r = x_0$) of a normalized radial wave function $\psi_{F-R}(r)$. The wave function is assumed to be constant up to a radius $R_c = x_0(1-b)$ and then exponentially decrease according to eq. (2.12) at larger distances. The "cut-off" parameter $b$ for a given projectile can be graphically determined as follows. Taking the logarithms of both sides of eq. (2.16), we have:

$$W \equiv \ln \frac{\gamma_F x_0^3}{S(Z_R, A_R)} = -b(2\alpha x_0) - \ln(1-b) + \text{const} \tag{2.17}$$

For a set of fragmentation yields from a given projectile, the function $W$ should vary linearly with $2\alpha x_0$ with a slope equal to the parameter $b$.

It should also be pointed out that the predictions of the model are strongly affected by the way the nucleons are assumed to be stripped from the projectile: as a single cluster (the simplest assumption) or, as more than one cluster or, as separate nucleons. Each of these choices has a different separation energy and thus results in a different value of the width and the yield.

A drawback of this model is that it gives only relative yields of fragments; no absolute cross sections can be predicted due to the complete neglect of the impact parameter (or the angular momentum) of the collision. A detailed microscopic calculation which takes into account the impact parameter along with the "Friedman" probability for the removal of a cluster from the projectile has been reported [Harv 85] and has provided yield predictions in agreement with experimental data.

In general, Friedman's model is in good agreement with the experimental data, as is Goldhaber's model, but it gives better results for fragments very close to the projectile, especially in cases where the cluster structure of the projectile may play an important role in the fragmentation process (e.g. stripping of an $\alpha$ particle from an $^{16}O$ or $^{20}Ne$ projectile [Frie 83, Home 84]). A derivation of the equations for the momentum-distribution widths and the yields according to Friedman's model is given in appendix A.

Finally, apart from the simple models of Goldhaber and Friedman, the characteristics of the momentum distributions can be calculated with the INC model [e.g. see Stép 91]. Calculations with the models described in this chapter and comparisons with the distributions of projectile-like fragments obtained from the measurements of the present work (chapters 3 and 4) are presented in chapter 5.

# Chapter 3

# Operation of the K1200 Interim Beamline as a Spectrometer

## I Introduction

The work presented in this chapter represents the first attempt to measure fragmentation products at 0 degrees using intermediate energy beams delivered by the K1200 cyclotron. Soon after the commissioning of the K1200 cyclotron, a short interim beamline [Sher 87] was installed outside the cyclotron in order to do nuclear research while the final beamlines and experimental devices were under construction. During this time, we designed and performed an experiment in which the interim beamline was operated as a 0-degree spectrometer [Soul 91].

In this chapter, after a description of the beamline, its characteristics and the detector system used, the measurements performed with this system are described. In addition, the procedures developed for the analysis of the data are presented along with several representative results of projectile fragment distributions obtained from these data. In appendix B, we include a discussion of relevant Beam Optics concepts and a derivation of the equations developed for the present study.

# II Description of the spectrometer and the detectors

The interim K1200 beamline consisted of four superconducting magnets (fig. 3.1), which were: a quadrupole singlet, a quadrupole doublet, a $\pm 16^{\circ}$ bending dipole magnet and a quadrupole doublet. The details of the construction of these magnets have been described elsewhere [Zell 85]. For the present study, we operated the two quadrupole doublets and the bending magnet as a 0-degree spectrometer (the quadrupole singlet was turned off). The characteristics of the magnetic elements of the spectrometer are summarized in Table 3.1.

Projectile fragments, produced in a fragmentation target placed 40 cm after the exit of the K1200 cyclotron, traveled through the device and were focused and detected inside a 92-inch diameter cylindrical scattering chamber. The detection system for the present work was mounted on the movable radial arm of the chamber and consisted of two position counters and a $\Delta$E–E plastic scintillator telescope. The first position counter was placed near the entrance to the 92-inch scattering chamber and the second counter 1.8 m further downstream. Both position counters were low pressure multiwire proportional counters (MWPC's) of Breskin type [Bres 82]. From these detectors (see Fig. 3.2), a position signal is obtained by a delay-line readout of the electric charge induced on two layers of interleaved cathode strips. The time difference between the signals from the two ends of the delay line can be measured and is proportional to position along the counter. The position measurement from the front counter contained information on the rigidity, whereas the difference between the position measurements of the two counters contained information on the scattering angle of a particle. Section VI describes in detail how the rigidity and the scattering angle were obtained from the measured position and angle.

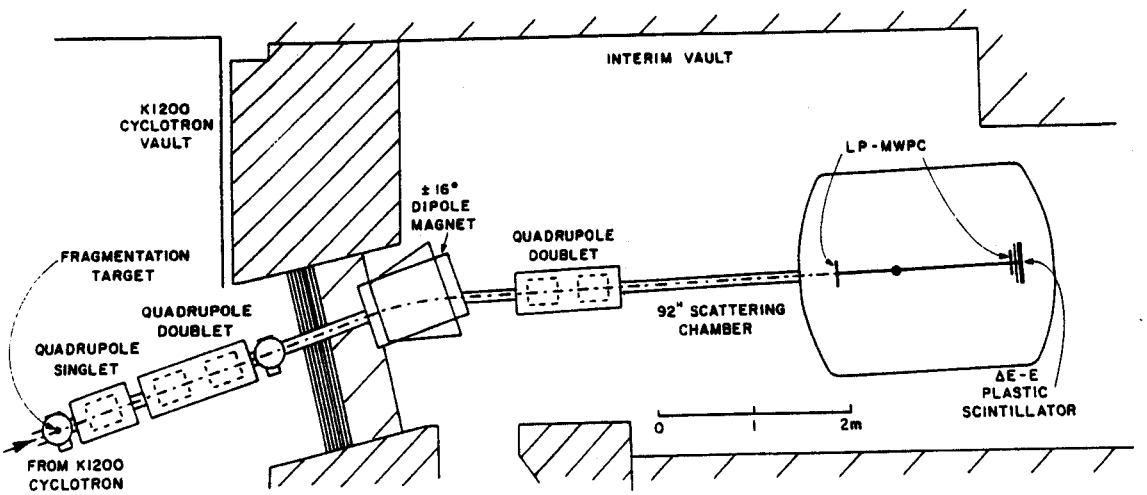


Figure 3.1: Schematic layout of the interim beamline spectrometer.

Table 3.1: Characteristics of the interim beamline spectrometer and its elements.

| Quadrupoles | |
|---|---|
| Effective length | 43.0 cm |
| Pole-tip radius | 5.08 cm |
| Max. magnetic field at pole tip | 15 kG |
| Electric current at max. field | 14 A |
| Distance between quads in a doublet | 16.7 cm |
| **Dipole** | |
| Mean deflection angle | 16.4° |
| Mean bending radius | 3.08 m |
| Entrance face angle | 0.0° |
| Exit face angle | 16.4° |
| Effective length of central trajectory | 0.882 m |
| Pole-gap width | 5.0 cm |
| Maximum magnetic field | 18 kG |
| Electric current at max. field | 100 A |

| Distances between elements | |
|---|---|
| Target— first doublet entrance | 1.187 m |
| First doublet exit—dipole entrance | 1.677 m |
| Dipole exit—second doublet entrance | 0.852 m |
| Second doublet exit—front MWPC | 2.662 m |
| Front MWPC—back MWPC | 1.840 m |

The ΔE–E telescope, mounted behind the back position detector, consisted of a thin (3 mm) fast plastic scintillator for energy loss measurement and a thick (5 cm) plastic scintillator as a stopping detector. Each scintillator was viewed by a photomultiplier tube (PMT) on each end (left or right). A ΔE parameter was calculated event-by-event by taking the square root of the product (geometric mean) of the left and right PMT signals of the ΔE scintillator. Due to light attenuation by self-absorption in the plastic scintillator, each PMT signal is exponentially dependent on the position of a particle along the scintillator. The product of the two signals is position independent and its square root proportional to ΔE (whereas the logarithm of the ratio of these signals is linearly related to position). The atomic number Z of the particles was obtained from the ΔE parameter, since according to Bethe equation [see e.g. Kran 87]: $\Delta E \propto \frac{Z^2}{v^2}$, where $v$ is the velocity of the particles.

The back MWPC had a low efficiency, so its position information was not used in the analysis of the data. Instead, a back position parameter was constructed from the logarithmic ratio of the two PMT signals of the ΔE scintillator. This position measurement was found to be consistent with the position measurement provided by the back MWPC for highly ionizing particles and was combined with the front position parameter to provide a final angle parameter for the particles. The position resolution of both MWPC's was better than 1 mm; the position resolution of the back position parameter obtained by the ΔE scintillator was 1.0 cm and the angle resolution obtained by the combination of this position parameter and the front position parameter was 6 mr. The fact that the angle measurement had to rely on the less accurate position values from the plastic scintillator had a significant effect on the overall momentum resolution (see section III).

Time of flight (TOF) was measured relative to the K1200 radiofrequency (RF) cycle. A start timing signal was obtained from the ΔE scintillator. A combination of

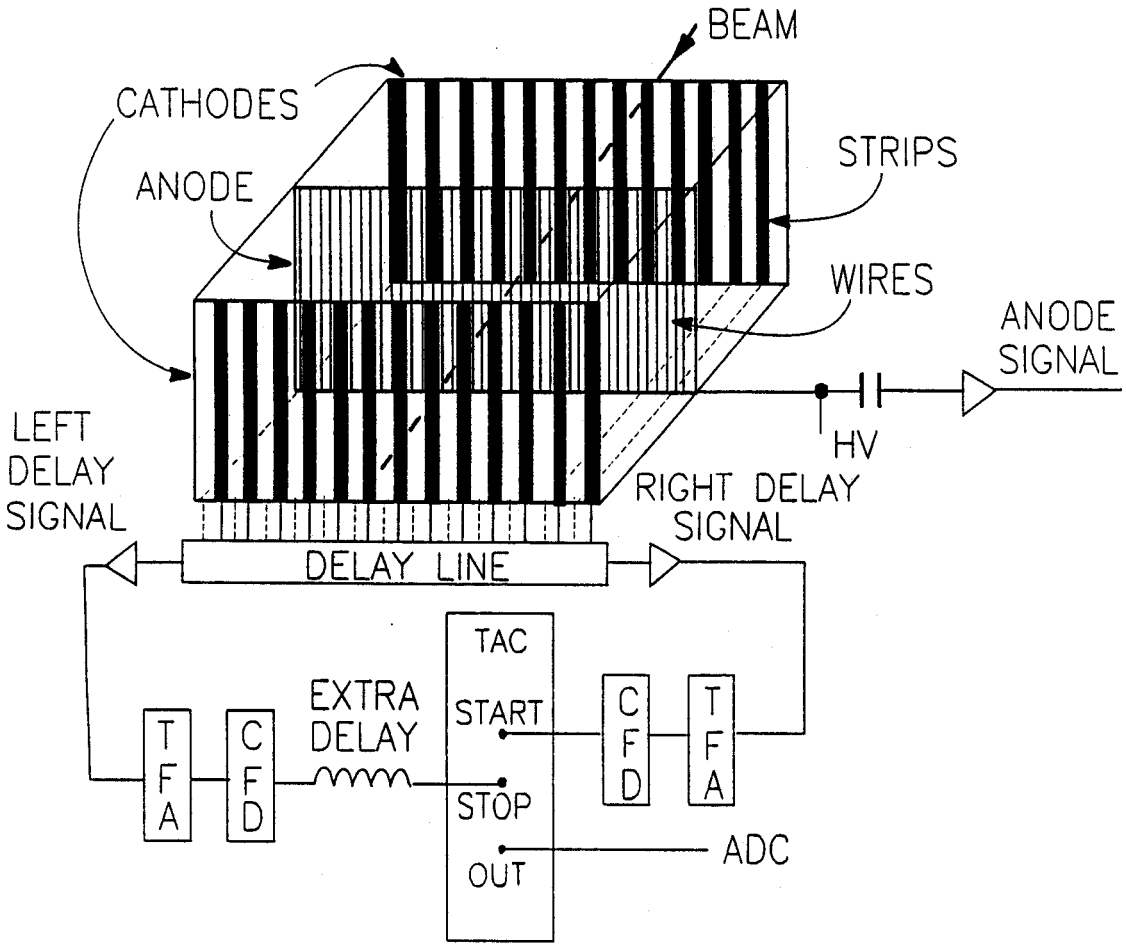


Figure 3.2: Schematic diagram of the MWPC and the delay-line position measurement. The anode of the detector consists of a series of closely and evenly spaced wires. Each of the two cathods consists of a thin plastic foil with evenly spaced aluminum strips deposited on it. The strips of both cathods are interleaved and alternately connected to a common delay line. The electron avalanche created by an ion entering the gas volume of the detector is collected by the nearest anode wires, whereas inducing a positive charge on the corresponding cathode strips. The time difference between the delay-line signals created by this induced charge is measured with a TAC and is linearly related to the position of the ion along the detector (for electronic module acronyms see Fig. 3.3).

TOF and position provided an A/q (mass-over-charge) parameter, which was combined with the $\Delta$E parameter in a two-dimensional histogram to provide particle identification. Due to multiple turn extraction from and the phase acceptance of the cyclotron, only limited TOF resolution (approximately 4 ns) was obtained, which hindered the isotope identification for Z's higher than 6.

# III Beam optics calculations

Beam optics calculations (up to third order), performed with the program TRANSPORT [Care 88], showed that a moderate acceptance solution was possible for this simple spectrometer, i.e. 35 mr horizontal and 10 mr vertical angular acceptances and 8% momentum acceptance. The optical characteristics of the spectrometer, the first order TRANSPORT matrix elements and the important second and third order matrix elements at the front position counter are summarized in Table 3.2. The TRANSPORT beam optics notation and units have been used in Table 3.2 and throughout this study. An overview of relevant Beam Optics concepts is given in appendix B. At the end of Table 3.2, the field values of the magnets corresponding to setting the spectrometer for $^{14}N^{7+}$ at 75 MeV/u [which has a momentum-over-charge ratio p/q of 0.762 (GeV/c)/e] are given.

For the present system, there are no first order correlations between the coordinates of the particle motion on the horizontal (bending) $xz$ plane and the vertical (non-bending) yz plane. However, such correlations arise in second and higher orders. The TRANSPORT calculation showed that the second and third order correlations of horizontal and vertical coordinates are negligible for the relatively small vertical angular acceptance of 10 mr; in all cases, the contributions to the position and angle resolution are less than 1 mm and 1 mr, respectively, and these contributions were

Table 3.2: Beam-optical characteristics of the interim beamline spectrometer.

| Important parameters | |
|---|---|
| Horizontal magnification | $(x\|x) = -0.63$ |
| Dispersion at the front MWPC | $(x\|\delta) = 0.65$ cm/% |
| Horiz. beam spot at the target (full-width) | $\Delta x_0 = 6$ mm |
| Max. horiz. angular acceptance | $\Delta\theta_0 = 35$ mr |
| Max. vertical angular acceptance | $\Delta\phi_0 = 10$ mr |
| Max. solid angle | $\Delta\Omega = 0.35$ msr |

First order TRANSPORT matrix elements

| $x$ | $\theta$ | $y$ | $\phi$ | $l$ | $\delta$ |
|---|---|---|---|---|---|
| -0.63119 | -0.07302 | 0.00000 | 0.00000 | 0.00000 | 0.64914 |
| 18.66188 | 0.57452 | 0.00000 | 0.00000 | 0.00000 | 0.61110 |
| 0.00000 | 0.00000 | 1.60686 | 0.80937 | 0.00000 | 0.00000 |
| 0.00000 | 0.00000 | 1.53734 | 1.39669 | 0.00000 | 0.00000 |
| 1.24998 | 0.04176 | 0.00000 | 0.00000 | 1.00000 | -0.01198 |
| 0.00000 | 0.00000 | 0.00000 | 0.00000 | 0.00000 | 1.00000 |

Second and third order matrix elements

| | |
|---|---|
| $(x\|x\delta) = -1.18 \times 10^{-1}$ | $(\theta\|x\delta) = -6.65 \times 10^{-1}$ |
| $(x\|\theta\delta) = -4.53 \times 10^{-3}$ | $(\theta\|\theta\delta) = -5.07 \times 10^{-2}$ |
| $(x\|\theta^2) = -5.8 \times 10^{-5}$ | $(\theta\|\theta^2) = -2.3 \times 10^{-4}$ |
| $(x\|\delta^2) = 1.02 \times 10^{-3}$ | $(\theta\|\delta^2) = 1.58 \times 10^{-2}$ |
| $(x\|\theta\delta^2) = 2.78 \times 10^{-4}$ | $(\theta\|\theta\delta^2) = 1.28 \times 10^{-3}$ |

| Magnetic fields (in KG) for $^{14}$N at 75 MeV/u | | | |
|---|---|---|---|
| First quad | 6.204 | Third quad | 1.701 |
| Second quad | -3.667 | Forth quad | -0.041 |
| Dipole | 8.244 | | |

neglected in the present study. Hence, only the correlations of the coordinates in the bending plane were taken into account when extracting the momentum and the scattering angle of a particle from the measured position and angle. Simple algebraic formulas and a calculation procedure were developed for this purpose and are described in section VI.

From the first order TRANSPORT matrix, we see that a relatively small value of the horizontal magnification $(x|x)$ is achieved, but a considerable $(x|\theta)$ term is present at the front counter, which introduces a first order correlation of final position with initial scattering angle. Consequently, a first order horizontal focus was only approximately created at the front detector. The actual focal plane [where $(x|\theta)$ is zero] lies in between the two detectors.

In any spectrometer with relatively large momentum and angular acceptance, there will be large second order aberrations [mainly due to the $(x|\theta\delta)$ term]. These can be corrected with sextupoles or by focal plane reconstruction. In the present study, we chose the latter method. Consequences of this choice are that it is not necessary to have a first order focus at a position sensitive detector, but an accurate angular measurement is required.

Generally, it is desirable for the contributions of the second and higher order matrix elements at the focal plane to be small fractions (i.e. less than 0.1) of the displacement due to the dispersion. When one position counter is used at the exit of a spectrometer, it is necessary that this detector be placed at the position of the focal plane. However, if two position detectors are used (thus final position and angle of the particles can be measured, as in the present system), it is not necessary to place one of the detectors along the focal plane. In such a case, the position of the focal plane can, in principle, be reconstructed offline, provided that the angle measurement has sufficient accuracy.

For the present system, where reaction angle and momentum reconstruction are performed, an experimental uncertainty in the the reaction angle of approximately 15 mr was obtained from the elastic scattering data. This value is consistent with a conservative estimate of 22 mr obtained from eq. (B.29), which takes into account the contribution from the final angle uncertainty and the beam-spot size (approximately 6 mm). Similarly, the experimental momentum resolution of approximately 2.0% can be mainly attributed to the reaction angle uncertainty combined with the presence of the $(x|\theta)$ term. An estimate of the momentum resolution of approximately 2.0%, based on the beam optics, can be obtained from eqs. (B.27) and (B.28). However, the momentum resolution of the system with only the front counter position, without scattering angle reconstruction, would be worse. Specifically, at the full horizontal angular acceptance of $\Delta\theta_0$=35 mr and momentum acceptance of $\Delta\delta$ = 8% of the spectrometer, the effects of the $(x|\theta)$ and $(x|\theta\delta)$ terms to the image width would result in a momentum resolution of approximately 4.5%.

# IV Electronics

A schematic diagram of the electronic modules used in the interim beamline experiment is shown in Fig. 3.3. The basic characteristics are discussed below. Each MWPC was connected to a TAC measuring the time difference between a START signal from the right end of the MWPC cathode delay-line and a STOP signal (additionally delayed) from the left end. Time-of-flight versus the RF was also measured by another TAC with a START signal from the $\Delta$E scintillator and a STOP signal from the cyclotron RF. The signals from the TAC's were sent to ADC's. The pulse height signals of both ends of the $\Delta$E and E scintillators were sent to QDC's and the corresponding timing signals were AND'ed. The event trigger (master gate) was defined by the coincidence of the timing signals from the scintillators (indicating that

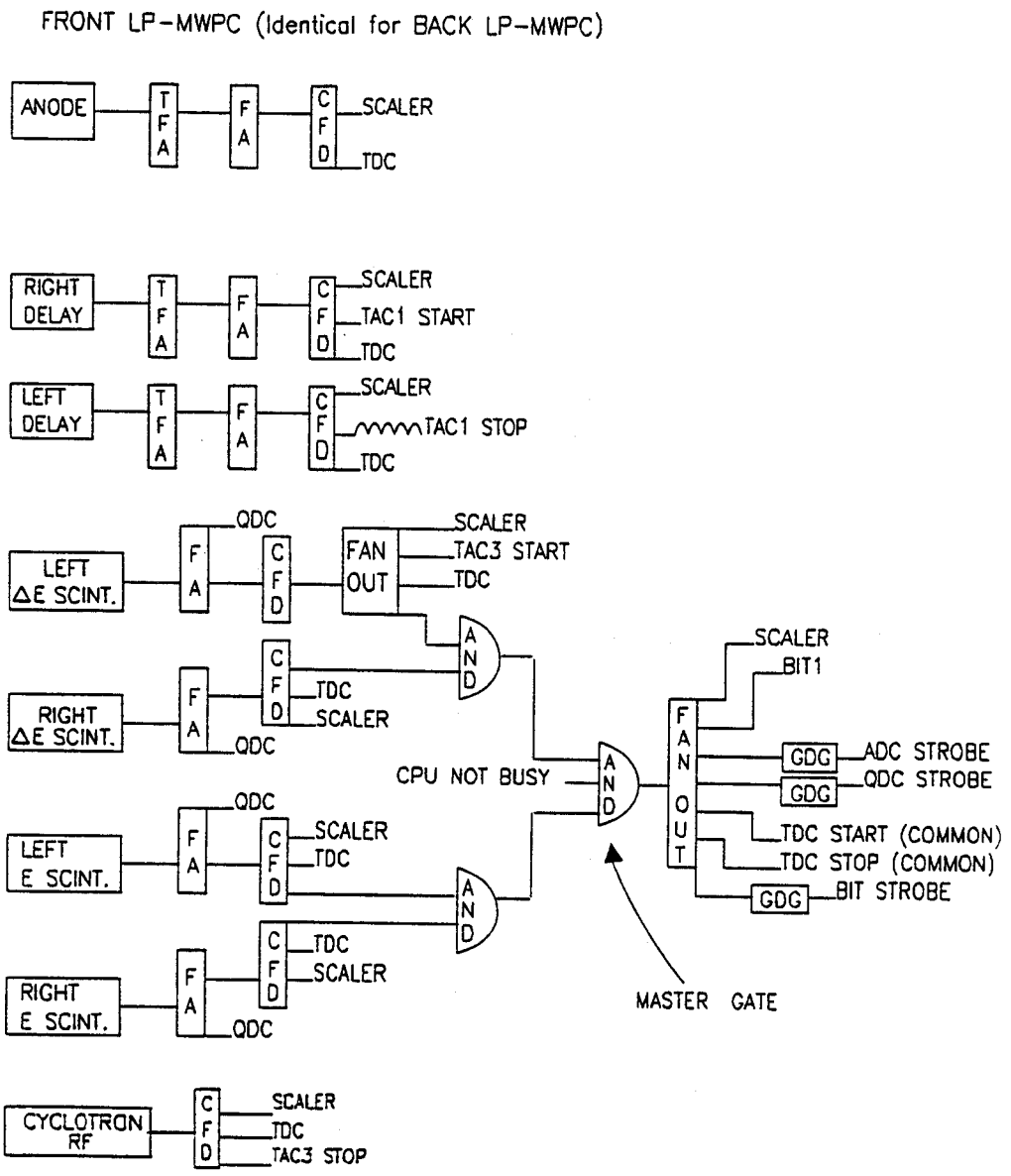


Figure 3.3: Schematic diagram of the electronics for the interim beamlime experiment. Electronic modules: TFA = timing filter amplifier, FA = fast amplifier, CFD = constant fraction discriminator, TAC = time-to-analog converter, TDC = time-to-digital converter, ADC = analog-to-digital converter, QDC =charge-to-digital converter, GDG = gate and delay generator.

a particle passed through the system) and the NOT-BUSY signal from the front-end computer. For diagnostic purposes, timing signals were recorded with TDC's for both MWPC's, both scintillators and for the RF. The TDC's were set-up in the "COMMON START" mode: a COMMON START signal was sent to them from the event trigger and the different timing signals were sent as STOP signals. A total of 17 signals were recorded by the front-end computer for each event trigger. The data acquisition software and hardware system used to read the ADC, QDC and TDC modules and record the data to tape was the standard NSCL data acquisition system [Fox 89].

# V The experiment

As a test of the beamline spectrometer, we measured the products from the reaction of a $^{14}N$ beam at 75 MeV/u with Al and Ta targets with thicknesses of 8 and 10 mg/cm$^2$, respectively. Data were collected for approximately 10 field settings in steps of 5%, covering the A/q region of 2.0 to 3.0. The magnetic field of the dipole was measured with an NMR magnetometer. For primary beam charge collection, an aluminum bar was placed inside the dipole and was connected to a current integrator. The position and angle calibration of the detectors was performed in two independent ways, giving consistent results: first, the radial arm (on which the detecting system was mounted) was rotated by a known angle and the change in position of the 0° elastically scattered beam particles was measured, and second, a slotted copper mask was inserted between the two counters and was irradiated with a dispersed primary beam.

# VI Data analysis and results

In the present 0-degree spectrometer, the momentum and the scattering angle of a particle leaving the target are related to the measured position and angle at the front position counter. The calculations and the procedure that were developed to extract these quantities from the data are described below.

We can write the magnetic rigidity $B\rho$ of a particle moving in the magnetic field of a dipole as [Care 87]:

$$B\rho = 3.3356 \frac{p}{q} \tag{3.1}$$

where $B$ is the magnetic field induction (in kG), $\rho$ is the radius (in cm) of the trajectory of the particle in the dipole field, $p$ is the momentum of the particle (in MeV/c) and $q$ is its charge (in units of elementary charge). In the present experiment, the position of the undeflected beam particles at several charge states ($^{14}N^{7+}$ and $^{14}N^{6+}$) obtained at several different magnetic field settings, directly calibrated the curvature radius $\rho$ versus position (fig. 3.4) corresponding to a scattering angle $\theta_b$ with respect to the spectrometer optical axis at the target position (fig. 3.5a). This angle, made by the beam emerging from the accelerator, was found to be $\theta_b \cong 1°$. We had no control over this angle, since the spectrometer was fixed and there were no bending elements after the cyclotron and before the target. However, it was exploited to increase the observed reaction-angle range to 2°.

The curvature radius—position calibration, shown in Fig. 3.4, can be well described by a linear function:

$$\rho(\theta_b) = A_0(\theta_b) - A_1(\theta_b) X_{FP} \tag{3.2}$$

where $X_{FP}$ is the position (in channel number) of a particle at the front position counter. Two additional calibration points, obtained in a subsequent experiment with

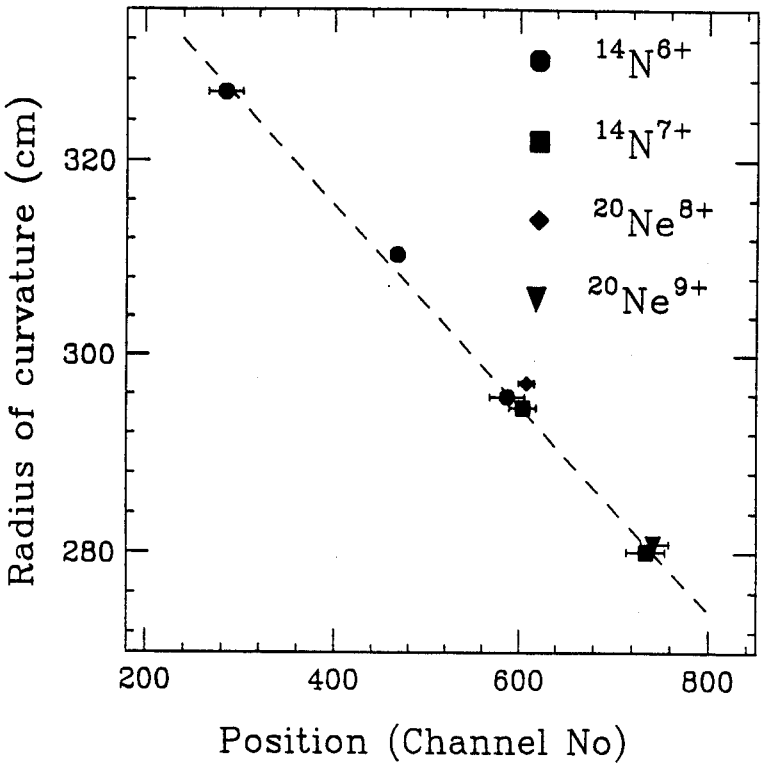


Figure 3.4: Calibration of the radius of curvarute versus front-counter position. The error-bars on the points have widths of $2\sigma$. The widths of the peaks of the elastically scattered beam particles which arrive near the center of the front detector are mainly due to the magnification term $(x|x)$. The growth of the peak widths with increasing distance from the center of the detector is attributed to the momentum dependent term $(x|x\delta)$. The dashed straight line is a least-squares fit to the data points.

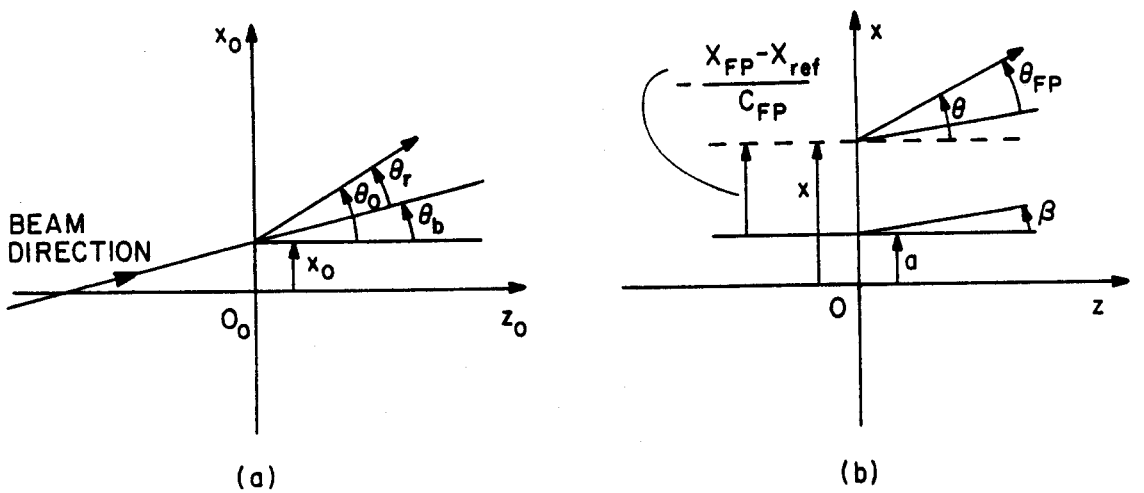


Figure 3.5: Coordinate systems used in the calculations of momentum and reaction angle:
a) Initial coordinate system (at the target position). The beam strikes the target with an offset $x_0$ and an angle $\theta_b$. Reaction products emerge from the target at angles $\theta_0$ relative to the spectrometer axis ($z$-axis). The interesting nuclear reaction angle is $\theta_r = \theta_0 - \theta_b$.
b) Final coordinate system (at the position of the front counter). In this system, $\alpha$ and $\beta$, respectively, are the position and angle coordinates of the 0° elastically scattered beam particles of one run that was chosen as reference; $x$, $\theta$ are the final position and angle coordinates, respectively, of a particle that entered the spectrometer with initial coordinates $x_0$, $\theta_0$ and momentum deviation $\delta$; the quantity $-\frac{X_{FP}-X_{ref}}{C_{FP}}$ is the position of the particle relative to the reference position $\alpha$ and $\theta_{FP}$ is the angle of the particle relative to the reference angle $\beta$.

a $^{20}$Ne beam at 65 MeV/u, agree very well with the nitrogen data. So, for a particle emitted at an angle $\theta_b$ relative to the spectrometer axis, eqs. (3.1) and (3.2) relate its momentum to the position on the front counter. But for angles $\theta_0$ different from $\theta_b$, the correlation of front counter position with angle $\theta_0$, produced in the spectrometer, renders eq. (3.2) inadequate. A $\theta_0$ versus front counter position calibration would be neccessary, which we were not able to obtain in the present experiment. There are at least two ways to perform this calibration; first, by bending the beam before the target with an inflector magnet system and second, by inserting a slotted aperture at a certain distance after the target. In the present work, the calibration was obtained from a TRANSPORT calculation, which should be adequate, as the fields of the magnets and their positions along the beamline are well known. In order to take into account the angle dependence of the curvature radius, a relation similar to eq. (3.2) was derived in which the coefficients $A_0$ and $A_1$ were expressed as functions of the angle $\theta_0$ in first order. Specifically we can write, similar to eq. (3.2):

$$\rho(\theta_0) = A_0(\theta_0) - A_1(\theta_0)X_{FP} \tag{3.3}$$

where now

$$A_0(\theta_0) = A_0(\theta_b) - K_0(\theta_0 - \theta_b) \tag{3.4}$$

$$A_1(\theta_0) = A_1(\theta_b) - K_1(\theta_0 - \theta_b) \tag{3.5}$$

where the coefficients $K_0$ and $K_1$ are related to the calculated first, second and third order matrix elements with the following expressions (these equations are derived in appendix B):

$$K_0 = \frac{\rho_0}{100(x|\delta)'}\left((x|\theta) + \frac{(x|\theta\delta)'}{(x|\delta)'}x_{off}\right) \tag{3.6}$$

$$K_1 = \frac{\rho_0}{100 C_{FP}} \frac{(x|\theta\delta)'}{(x|\delta)'^2} \tag{3.7}$$

where:

$$(x|\theta\delta)' = (x|\theta\delta) + (x|\theta\delta^2)\delta \tag{3.8}$$

$$(x|\delta)' = (x|\delta) + (x|x\delta)x_0 \tag{3.9}$$

$$x_{off} = \frac{X_{ref}}{C_{FP}} + \alpha - (x|x)x_0 \,. \tag{3.10}$$

In these expressions we have: $\delta = 100\frac{\Delta p}{p}$ the momentum deviation (in %) of the particle from the momentum of the central ray, $\rho_0$ the radius of curvature (in cm) of the central ray inside the dipole magnet, $x_0$ the $x$–coordinate of the beam-spot at the target position (fig. 3.5a), $C_{FP}$ the position calibration coefficient of the front position counter (in channels/cm), $X_{ref}$ the position (in channel number) of the $0^o$ elastically scattered beam particles of one run that was chosen as reference, and $\alpha$ the final position (in cm) of the reference beam particles relative to the optical axis of the spectrometer (fig. 3.5b). Terms including $x_0$ were taken to be zero, because the value of $x_0$ was not known (but was thought to be small).

One can see that eqs. (3.4) and (3.5) are functions of the reaction angle $\theta_r = \theta_0 - \theta_b$, that is the angle of a particle leaving the target relative to the beam direction, which is, of course, the interesting nuclear reaction angle. This angle can be calculated by the formula:

$$\theta_r = \theta_0 - \theta_b = \frac{\theta_{FP} - [C_0(\theta_b) + C_1(\theta_b)\delta + C_2(\theta_b)\delta^2]}{(\theta|\theta) + (\theta|\theta\delta)\delta + (\theta|\theta\delta^2)\delta^2} \tag{3.11}$$

where $\theta_{FP}$ is the angle (in mr) of a particle at the front position detector relative to the reference beam and $C_0(\theta_b)$, $C_1(\theta_b)$, $C_2(\theta_b)$ are the coefficients of a quadratic fit of the relation $\theta_{FP} = f(\delta)$ for the $0^0$ elastically scattered beam particles (that is, for

$\theta_0 = \theta_b$). So, the scattering angle of a given particle can be calculated according to eq. (3.11) from its final angle $\theta_{FP}$ and its momentum deviation $\delta$.

The $\delta$–dependence of the reaction angle $\theta_r$ and of the curvature radius $\rho(\theta_r)$ for a particle indicates that a successive approximation calculation has to be performed in order to obtain $\theta_r$ and $\rho(\theta_r)$ from the measured quantities $X_{FP}$ and $\theta_{FP}$. For this calculation, an initial value of $\delta$ for a particle was obtained from its position $X_{FP}$ using eq. (3.2) and the relation $\delta = 100\frac{\rho-\rho_0}{\rho_0}$. The convergence of this iterration is fast, i.e. in few steps.

Using these expressions and procedure, the curvature radius (thus the momentum) and the reaction angle of the particles were calculated on an event-by-event basis. The resolutions (FWHM) of the curvature radius and the reaction angle were approximately 2.0% and 15 mr, respectively.

As is standard in spectrometer measurements, an $A/q$ parameter was constructed using the expression for the curvature radius and the measured TOF. Substituting the momentum $p = \gamma A m_p v$ in eq. (3.1), we have:

$$B\rho = 3.3356\ \frac{\gamma A m_n v}{q} \tag{3.12}$$

where $\gamma$ is the relativistic factor $\gamma = (1 - \frac{v^2}{c^2})^{-1/2}$, $m_n$ is the nucleon mass (in MeV/c$^2$) and $v$ is the velocity of the particle (in units of c, the speed of light). For the velocity of a particle we can write: $v \propto \frac{L}{T-TOF}$, where $L$ is the flight path length between the target and the timing detector, TOF is the measured time-of-flight (relative to the RF cycle) and $T$ is a constant (representing the number of RF periods elapsed between a given reaction at the target and the next beam pulse after the start signal for this event from the detector). Substituting this expression of $v$ in eq. (3.12) and

solving for $A/q$ we get:

$$\frac{A}{q} \propto B\rho \frac{T - TOF}{L} \tag{3.13}$$

from which the $A/q$ parameter can be calculated also on an event-by-event basis.

Isotope separation and identification were performed using a two-dimensional histogram of $\Delta$E versus $A/q$, generated for each run. In this histogram, the groups corresponding to the elastically scattered beam particles, when present, were used to calibrate the $A/q$ axis. For each isotope group on the $\Delta$E vs $A/q$ histogram a software gate was drawn from which a $\theta_r$ vs $p/q$ histogram was generated. Unfortunately, due to limited TOF resolution, the isotope groups were not completely separated and thus, each isotope gate was contamimated by neighboring isotopes.

Up to this point, the offline analysis was performed with the NSCL data analysis program SARA [Winf 91]. For the subsequent analysis, a program was developed for manipulation of the $\theta_r$ vs $p/q$ spectra in order to obtain the momentum distributions of the different isotopes. The analysis steps performed by this program are outlined below. First, a "control" matrix was created for the program. This matrix had elements of the form: gate(isotope,run); that is, the elements were the gate numbers of the different isotopes observed in the different runs of the experiment. The matrix was read by the program enabling it to collect, for every isotope, the $\theta_r$ vs $p/q$ spectra from all the runs in which the isotope was present. Then, for each $\theta_r$ vs $p/q$ spectrum, the program performed a cut of $\theta_r$ in three regions with centers at $1^o$, $2^o$ and $3^o$ and widths of $1^o$. For each of these reaction-angle regions the program generated a $p/q$ spectrum.

For normalization purposes, for each isotope, the program created a matrix of the form: counts(p/q,run), containing the number of counts of every $p/q$ channel for every run. The ratio of counts for runs with overlapping rigidity settings provided a way to

obtain a relative normalization of the runs. Beam charge collection was satisfactory for only few of the runs (in which the beam was bent enough to hit the aluminum-bar Faraday-cup in the dipole) and thus, we had to use this relative normalization method for the rest of the runs.

For every isotope at each angle (1°, 2° and 3°), the program normalized the $p/q$ spectra, converted them to $p/A$ spectra and properly combined the latter to give the final $p/A$ distributions. Finally, it integrated the $p/A$ distributions at each angle to create the angular distributions of the isotopes.

As representative results of the present study, the momentum distributions of $^{13}$C, $^{15}$B and $^{11}$Be produced by the $^{14}$N beam at 75 MeV/u on Al target and their angular distributions from Al and Ta targets are shown in Fig. 3.6. The error-bars are statistical and are omitted when they are smaller than the plotting symbols. We conservatively estimate that a factor of approximately 2 accounts for the systematic errors primarily due to the uncertainty in the normalization of different runs with overlapping momenta (approximately ±20%) and to uncertainties in the beam current integration.

The present results exhibit the main characteristics of momentum and angular distributions of projectile-like isotopes produced at intermediate energies at and near 0 degrees. Near-projectile fragments (one or two nucleons removed), like $^{13}$C, have narrow momentum distributions peaked near the beam velocity. Their angular distributions show the effect of Coulomb deflection, since for the Al target they are steeper than those for the Ta target [Bibb 79]. If more nucleons are removed from the projectile, the fragments, like $^{11}$Be, have wider momentum distributions peaked again near the beam velocity. Nucleon-transfer (pick-up) products have also been observed in the experiment. The momentum distributions of these products (e.g. $^{15}$B in Fig. 3.6) are peaked at considerably lower velocities than that of the beam. More

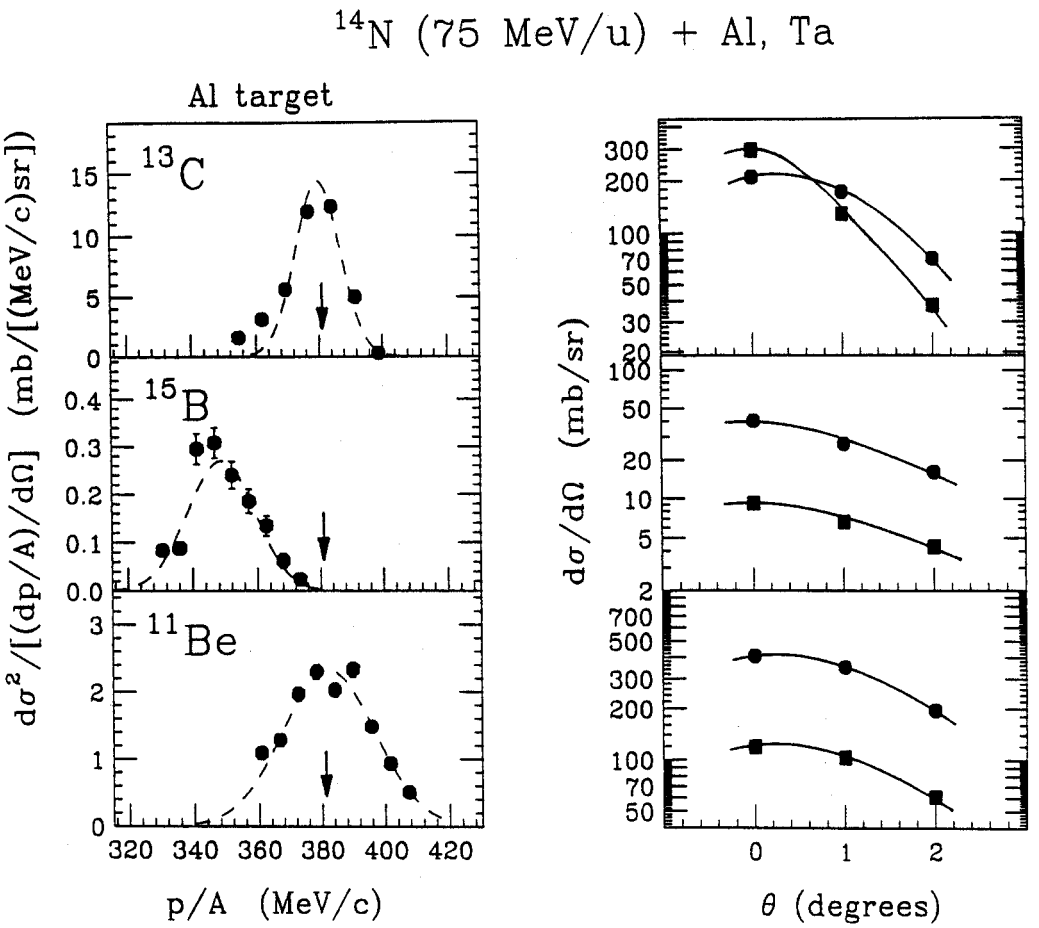


Figure 3.6: Momentum and angular distributions of several projectile-like isotopes produced by a $^{14}$N beam at 75 MeV/u on $^{27}$Al and $^{181}$Ta targets. The momentum/nucleon distributions are at 0° from the $^{27}$Al target. The arrows correspond to the momentum/nucleon of the beam. The dashed lines are Gaussian functions fitted to the data. The angular distributions are from both the Al (squares) and Ta (closed points) targets. The lines are just to guide the eye.

detailed measurements of such transfer products are presented in chapter 4 and their characteristics are analysed in chapter 5.

Summarizing, the quality of the results of this experiment was limited, due to the following reasons: first, the poor TOF resolution which hindered a clear isotope separation and second, the limited momentum and reaction-angle resolution of the spectrometer. The latter was partially due to time constraints during the experiment, which prevented us from fully investigating the optics of the spectrometer and performing more detailed calibrations. Nevertheless, the analysis of this data set was very instructive, leading us to develop procedures to manipulate and combine effectively the large number of spectra involved in the construction of distributions of projectile fragmentation products. The preparation and experience obtained from the present study was crucial for our subsequent measurements with the A1200 beam analysis device, which are described in the following chapter. Finally, from a practical standpoint, the experiment was very informative, giving us insight into how to operate a 0-degree spectrometer for fragmentation measurements and indicating the problem of the alignment of the beamline (relative to the direction of the beam as emerging from the accelerator) and the critical nature of the stability of the RF timing for the future experiments with the A1200.

# Chapter 4

# Projectile Fragmentation Measurements with the A1200 Mass Separator

## I Introduction–Description of the A1200

In this chapter, studies of the projectile fragmentation process with the A1200 Mass Separator are described. This work represents a continuation of our preliminary study with the interim K1200 beamline (described in chapter 3) in which more detailed measurements of the momentum distributions of near-projectile fragments and especially of few nucleon pick-up products from peripheral reactions at intermediate energy were made.

The A1200 beam analysis device [Sher 90], built in the place of the interim K1200 beamline, connects the K1200 cyclotron with the experimental vaults. The A1200 can be used either as a beam transport device or as a fragment separator. It can separate projectile fragments from K1200 beams and deliver them to the various experimental devices or it can be operated in a "stand-alone" mode to study these fragments. The A1200 (fig. 4.1) consists of a large number of superconducting magnets [Zell 85], which are: four 22.5° bending dipole magnets, four quadrupole doublets and two quadrupole triplets. There are also four room-temperature sextupole magnets for

aberration corrections.

The design and the symmetry of the A1200 allow two basic modes of operation: a dispersive mode and an achromatic mode. In the dispersive mode, intended for accurate cyclotron beam analysis purposes, the dispersions of the two dipole pairs are added to give a maximal resolving power but a small acceptance. In the achromatic mode, primarily used for radioactive beam separation, the dispersions are canceled at the end of the device to provide a final achromatic image, while creating two intermediate dispersive images (labeled Image #1 and Image #2 in Fig. 4.1) between the two pairs of dipoles.

Furthermore, in the achromatic mode, two different acceptance modes are possible: an intermediate (or medium) acceptance mode, if the target (labeled OBJECT in Fig. 4.1) is placed at the beginning of the A1200, and a high acceptance mode, if the target is placed near the entrance to the first quadrupole triplet. The characteristics of the A1200 operation modes are summarized in Table 4.1.

The magnets of the A1200 can be conveniently set to a desired $B\rho$ value with a computer code. For a given rigidity value the code calculates the currents for the magnets and sends the values to the power supplies. This program requires a minimum amount of time to set all 22 magnets of the spectrometer for a measurement at a given rigidity value. This feature was crucial for our distribution studies, because in order to cover a substantial momentum range for all the interesting isotopes, a large number of data runs (e.g. $\sim$20-30) of neighboring rigidity settings had to be performed (since the A1200 has a momentum acceptance of only 3% in the medium acceptance mode). For accurate rigidity measurements, the fields of the dipole magnets are measured by NMR magnetometers. For beam charge collection, aluminum bars are located in the first pair of dipoles, along with movable blockers at the exits of these dipoles. The bars and the blockers can be connected in series to a current integrator.

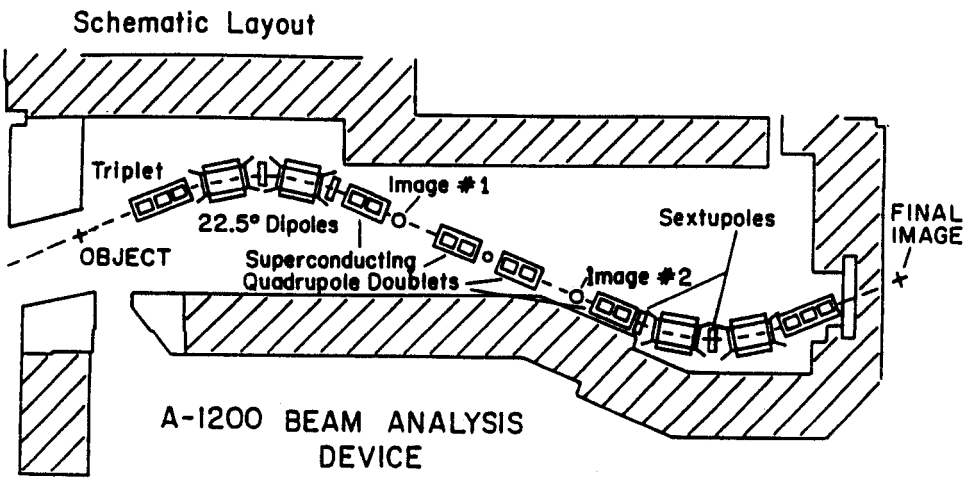


Figure 4.1: Schematic layout of the A1200 beam-analysis device.

Table 4.1: Characteristics of the operation modes of the A1200 [Sher 90].

| Parameter | Operation Mode | | |
|---|---|---|---|
| | High Res. | Medium Acc. | High Acc. |
| $\Omega$[msr] | 0.1 | 0.8 | 4.3 |
| $\Delta\theta$[mr] | 10 | 20 | 54 |
| $\Delta\phi$[mr] | 10 | 40 | 80 |
| $\Delta$P/P[%] | 0.4 | 3.0 | 3.0 |
| B$\rho$[T-m] | 5.4 | 7.2 | 5.4 |
| Resolution† | 10000‡ | 3300 | 1300 |
| (x/x) | | | |
| Int. Image | 3.0 | 0.47 | 1.24 |
| Focal Plane | 1.0 | 0.99 | 1.0 |
| (x/$\delta$)[cm/%] | | | |
| Int. Image | 15.0 | 1.67 | 1.80 |
| Focal Plane | 10.0 | 0.0 | 0.0 |

†1mm beam spot on the production target.
‡at the final image, with half the resolution at the center image.

# II Experiment and results

In the fragmentation measurements with the A1200, we operated the device as a 0-degree spectrometer in the achromatic medium acceptance mode. The full angular acceptance ($\Delta\theta$ = 20 mr, $\Delta\phi$ = 40 mr) around 0-degrees (i.e., beam direction) was employed. Fragmentation targets were placed at the beginning of the device ("OBJECT" in Fig. 4.1). The reaction products were focused at the end of the device on to a detection array consisting of two X–Y position sensitive parallel-plate avalance counters (PPACs) and a $\Delta$E–E telescope. The $\Delta$E detector was a totally depleted ion-implanted silicon detector (briefly called "PIN-diode") 500 microns thick with an active area of 25 cm$^2$. The E detector was a 5 cm thick plastic scintillator viewed by two photomultiplier tubes, one on each end. The two PPACs before the $\Delta$E–E telescope, separated by ~60 cm, were used to monitor the focusing of the particles: the first PPAC determined the position of the particles at the final image and, combined with the second one, the final angle with respect to the optical axis of the device. A third X–Y sensitive PPAC was positioned at the second intermediate image (Image #2 in Fig. 4.1) of the A1200. At this dispersive image, the horizontal position of the particles is linearly related to their rigidity, and thus the momentum of the particles can be calculated.

The position signals from the PPACs were created by charge division of an electron avalanche collected on a series of anode strips (which were connected in series with resistors). Each detector has two sets of anode strips, one horizontal and one vertical, thus providing X- and Y-position information. The principle of resistive charge division is illustrated in Fig. 4.2. The PPACs were operated with isobutane gas at a pressure of 5 torr and at an anode voltage of ~600 Volt. The position resolution (FWHM) obtained with these detectors was approximately 1 mm.

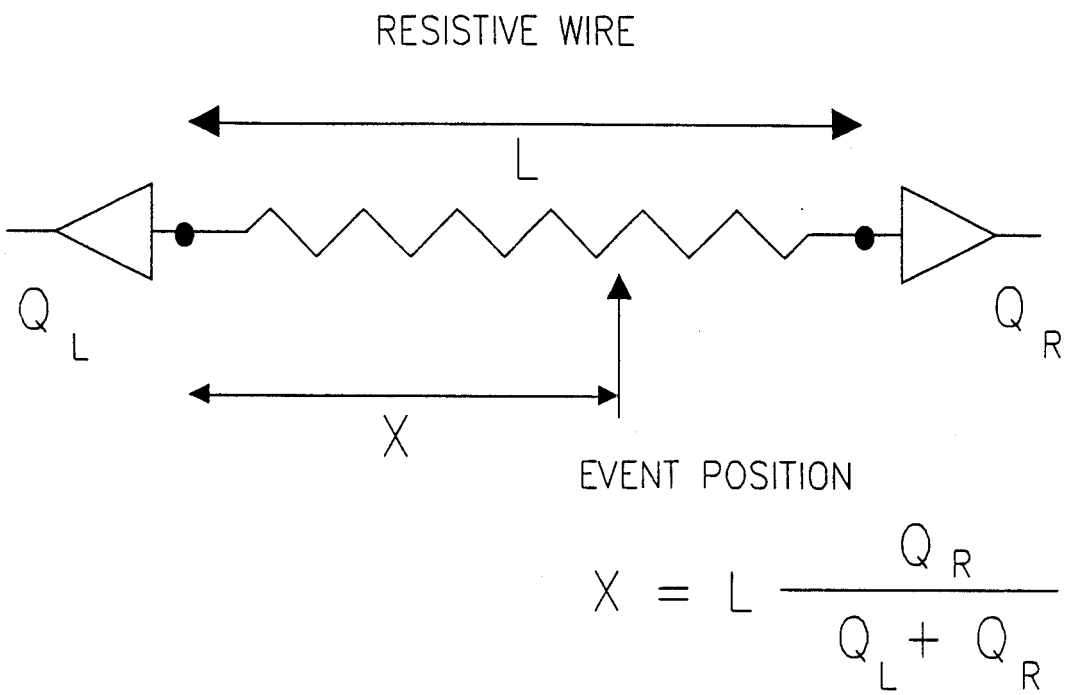


Figure 4.2: The principle of resistive charge division for position measurements. The charge of an electron avalanche, created by a fast charged particle entering the gas volume of the detector, is collected by a series of anode strips which are connected in series with resistors. The charge is split into two fractions, which propagate towards the two ends of the resistor series. The ratio of the signals at the ends of the resistor series is directly related to position.

A calibration of rigidity versus Image #2 horizontal position (simply called *position* in the following) was obtained by measuring the positions (channel numbers) of the 0-degree elastically scattered beam particles with various charge states (see Fig. 4.7). An absolute measurement of the beam momentum was achieved by positioning a known charge state of the beam at the center of Image #2 PPAC and recording the magnetic fields of the first pair of dipoles.

Time-of-flight was measured against the RF cycle of the cyclotron, with a resolution (FWHM) better than 2 ns for the particles of interest. The $\Delta$E measurement with the PIN-diode provided very good Z separation and a combination of $\Delta$E with the TOF measurement provided unambiguous particle identification (see Fig. 4.8).

A schematic diagram of the electronic modules used in the present measurements is shown in Fig. 4.3. The basic characteristics are similar to those described in the previous chapter and are briefly described here. The four position signals (Left, Right, Top, Bottom) obtained from each of the three PPACs were read by ADC's. TOF against the RF cycle was measured with a TAC. The $\Delta$E detector signal was sent to an ADC; the two E-scintillator PMT signals were sent to QDC's and their timing signals were AND'ed. The event trigger (Master Gate) was defined by the coincidence of the following signals: the AND'ed Image #2 PPAC left and right signals, the $\Delta$E signal and the AND'ed left and right scintillator signals. Again for diagnostic purposes, TDC signals were recored for all the PPACs, the $\Delta$E detector, the E scintillator and the RF timing. A total of 31 signals were recorded by the front-end computer. Again, the standard NSCL data acquisition system was used to read the electronics modules and write the data to tape [Fox 89].

In our first experiment with the A1200, upon commissioning of the device, we measured the fragmentation products from the reactions of a $^{20}$Ne beam at 85 MeV/u with $^{181}$Ta (10 mg/cm$^2$) and $^{9}$Be (3 mg/cm$^2$) targets. The target thicknesses were

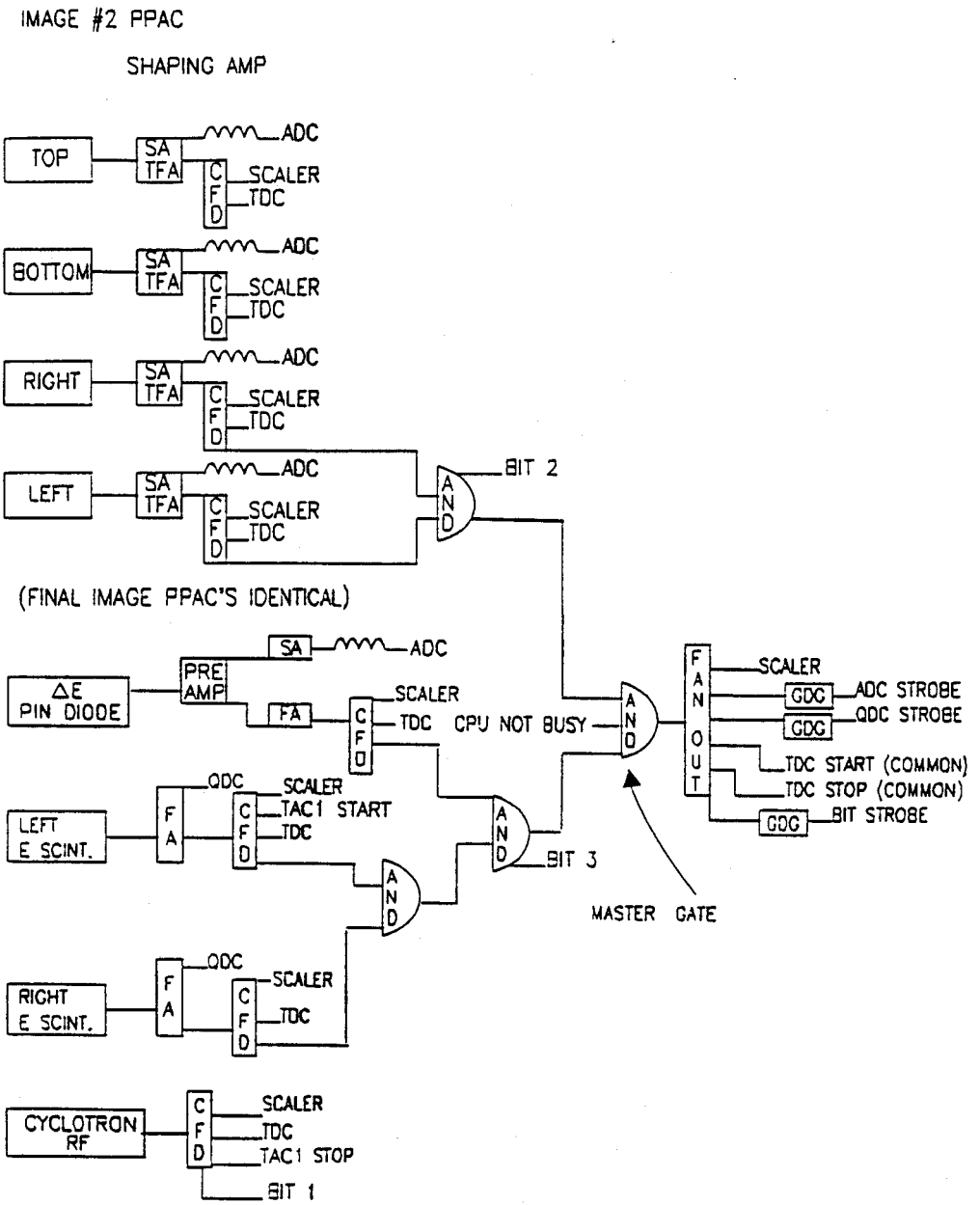


Figure 4.3: Schematic diagram of the electronics for the fragmentation experiments with the A1200 (for definitions of the acronyms see Fig. 3.3).

such that, for the particles of interest, the energy loss and the angular spreading due to multiple scattering were negligible. A series of successive data acquisition runs were performed at overlapping rigidity settings that covered the $A/q$ region of 2.1 to 3.0. The rigidity steps were 2% and thus, an 1% overlap between runs with neighboring rigidity settings was obtained (since the rigidity acceptance of the A1200 is 3%). In addition to the $^{20}$Ne experiment, we performed the same series of measurements with beams of $^{15}$N and $^{18}$O at 70 MeV/u with the $^{181}$Ta target.

The analysis of these data sets was similar to the data analysis described in chapter 3. However, it should be pointed out that the reconstruction of important quantities from these data was simpler and more accurate, due to the superior optical characteristics of the A1200 compared to those of the simple interim beamline.

Isotope separation and identification were performed, as already mentioned, with a two-dimensional histogram of $\Delta$E vs A/q. The isotope groups were very well separated and unambiguously identified. For each isotope, a position spectrum was generated. The position spectra were converted to p/A spectra (using the rigidity-position calibtation) with a modified version of the program for spectrum manipulation discussed in chapter 3. Subsequently, with this program, the p/A spectra were normalized and properly combined to give the final p/A distributions. Normalization of runs with the beam current integrator was not successful, since in many runs the unreacted beam was not completely collected by the Faraday cups inside the first pair of dipoles. Again, we had to rely on a relative normalization of the runs, which turned out to be partially successful (mainly due to the small overlap between runs with neighboring rigidities). For this reason, only a few of the spectra were of good quality. The best PLF momentum distributions from this analysis are shown in Figures 4.4, 4.5 and 4.6.

In addition to the previous experiments, a detailed measurement of the fragmentation products from an $^{18}O$ beam at 80 MeV/u with an $^{27}Al$ (5 mg/cm$^2$) target was performed at a later time. As additional experience operating the A1200 had been acquired, this measurement was more successful and complete. In this experiment, beam charge normalization was obtained using a monitor detector placed a short distance after the target at a small angle relative to the beam direction. For a given run, the total number of counts recorded by this detector was proportional to the beam charge of this run, thus providing a satisfactory normalization of the different runs. The data analysis of this experiment was similar to the analysis of the previous experiments. In addition, the momentum distributions of the isotopes were also normalized by the corresponding efficiency of Image #2 PPAC relative to the $\Delta$E detector (whose efficiency was taken to be 1). The relative yields of the fragments were obtained by integrating the normalized momentum distributions and are analysed in chapter 5. Representative results of momentum distributions from this measurement, along with Gaussian functions fitted to the data, are shown in Figures 4.9 and 4.10.

The momentum distributions obtained from the measurements with the A1200 were of better quality compared to the distributions obtained from the K1200 interim beamline measurements. As also previously observed, along with nucleon-removal products (whose distributions were centered very close to the beam velocity), nucleon pick-up products have been observed in these measurements (with momentum distributions peaking at velocities lower than that of the beam). An analysis and discussion of these distributions is presented in chapter 5.

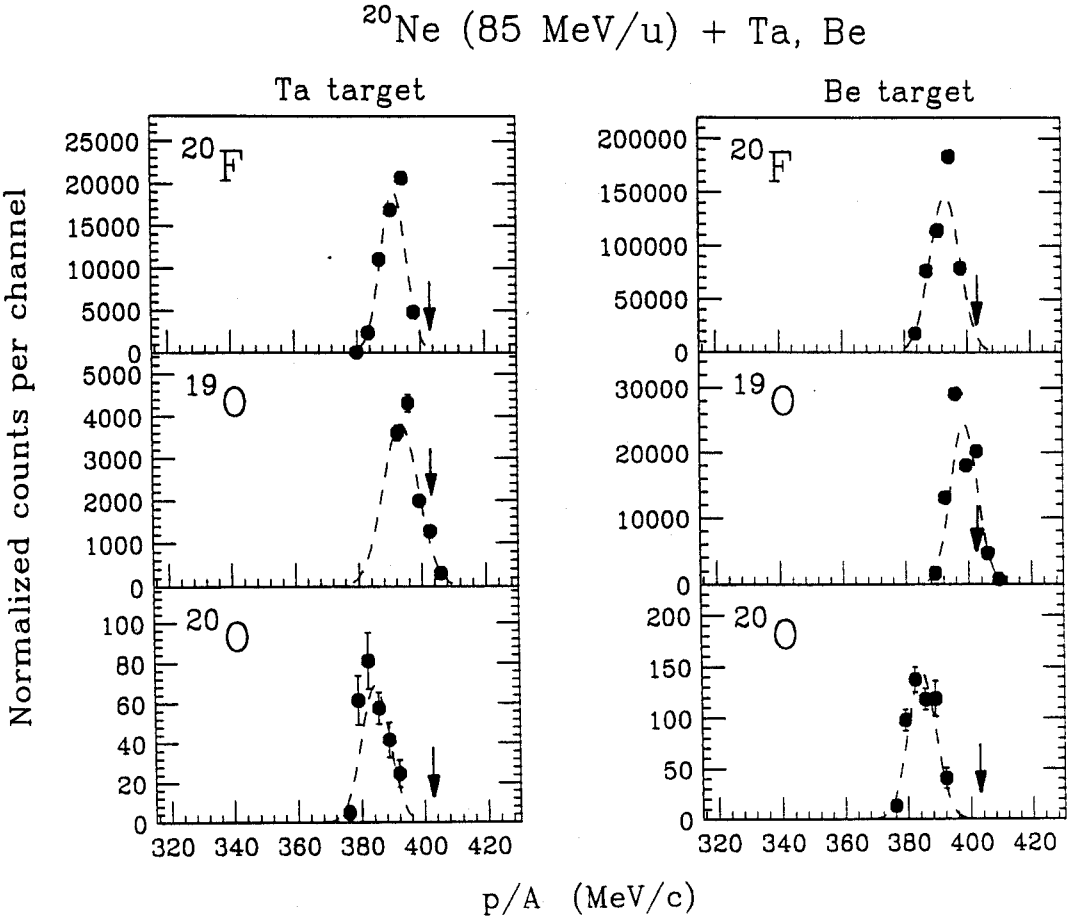


Figure 4.4: Momentum/nucleon distributions of PLFs produced by a $^{20}$Ne (85 MeV/u) beam on $^{181}$Ta and $^{9}$Be targets. The arrows correspond to the momentum/nucleon of the beam. The dashed lines are Gaussian functions fitted to the measured distributions.

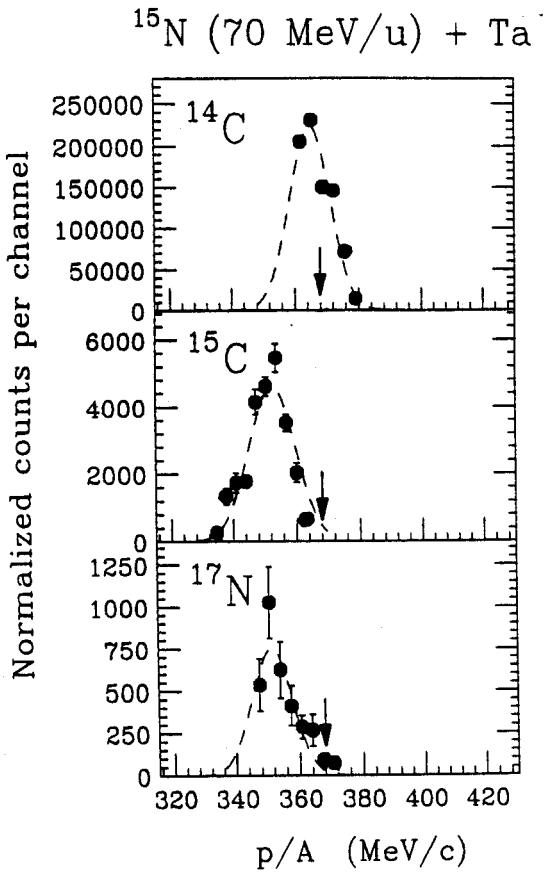


Figure 4.5: Momentum/nucleon distributions of PLFs produced by a $^{15}$N (70 MeV/u) beam on a $^{181}$Ta target. The arrows correspond to the momentum/nucleon of the beam. The dashed lines are Gaussian functions fitted to the measured distributions.

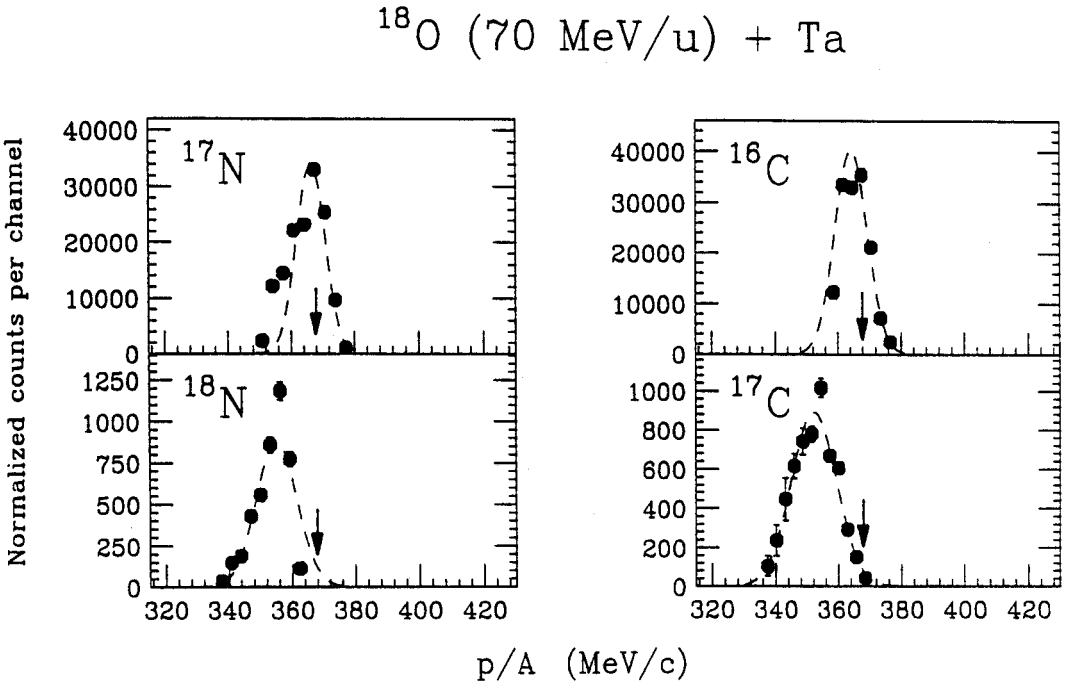


Figure 4.6: Momentum/nucleon distributions of PLFs produced by a $^{18}$O (70 MeV/u) beam on a $^{181}$Ta target. The arrows correspond to the momentum/nucleon of the beam. The dashed lines are Gaussian functions fitted to the measured distributions.

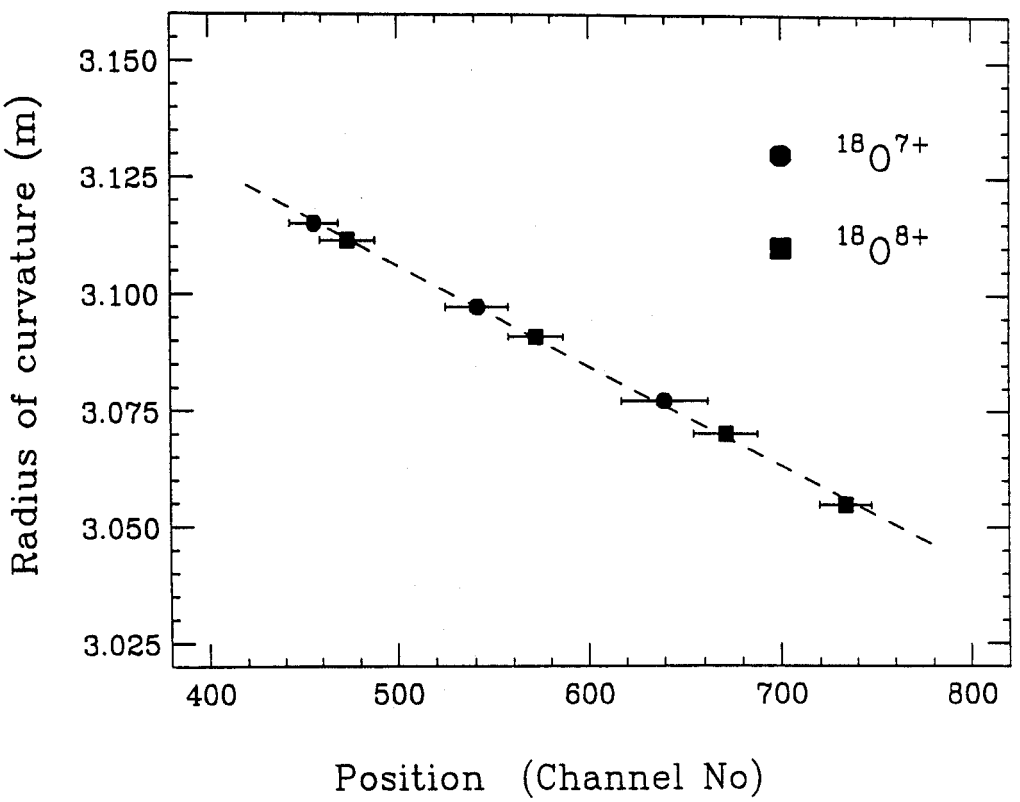


Figure 4.7: Rigidity vs Image #2 position calibration for the $^{18}$O (80 MeV/u) + $^{27}$Al experiment. The dashed straight line is a least-squares fit to the data points.

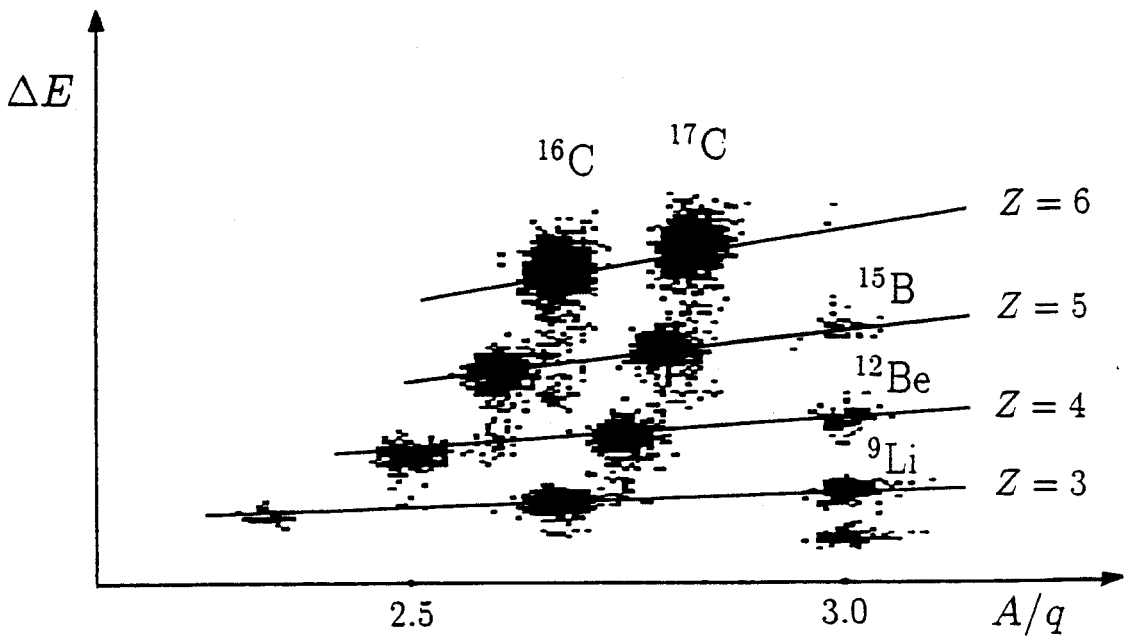


Figure 4.8: An example of a ΔE vs A/q histogram from the $^{18}$O (80 MeV/u) + $^{27}$Al experiment.

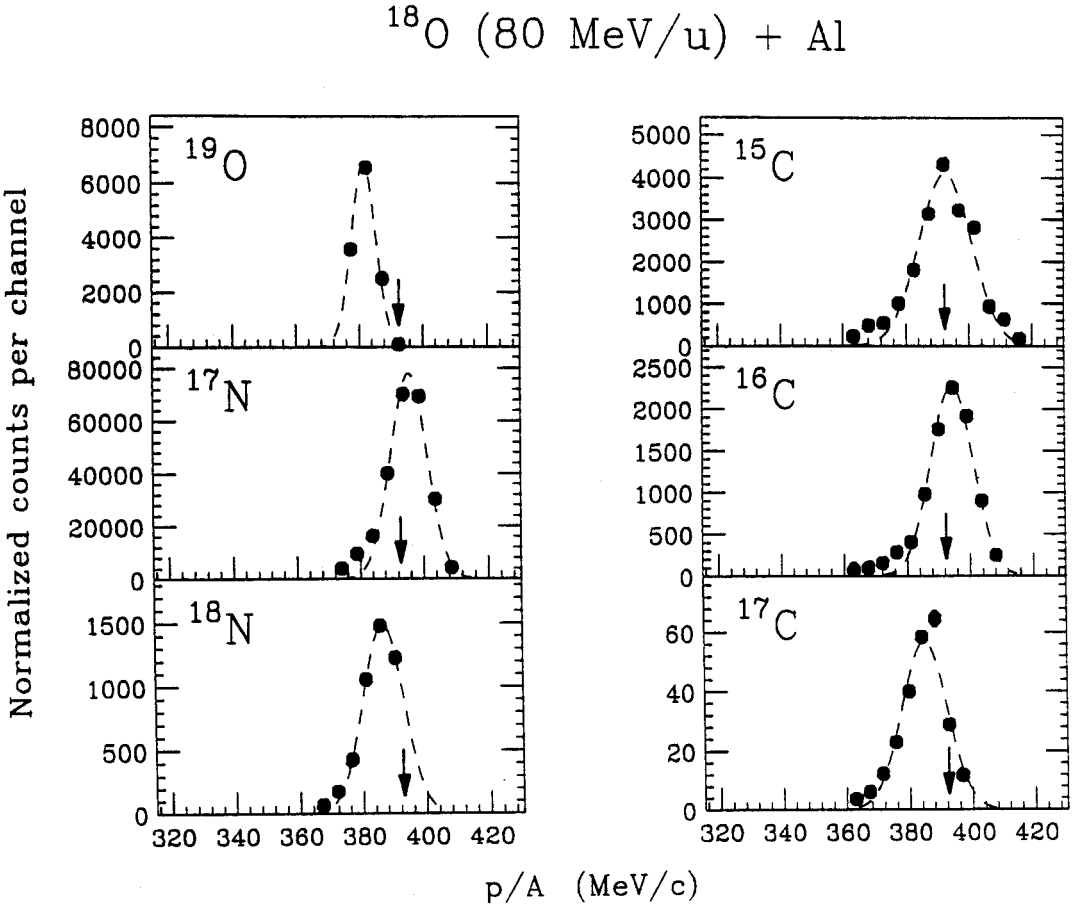


Figure 4.9: Momentum/nucleon distributions of PLFs produced by a $^{18}$O (80 MeV/u) beam on an $^{27}$Al target. The arrows correspond to the momentum/nucleon of the beam. The dashed lines are Gaussian functions fitted to the measured distributions.

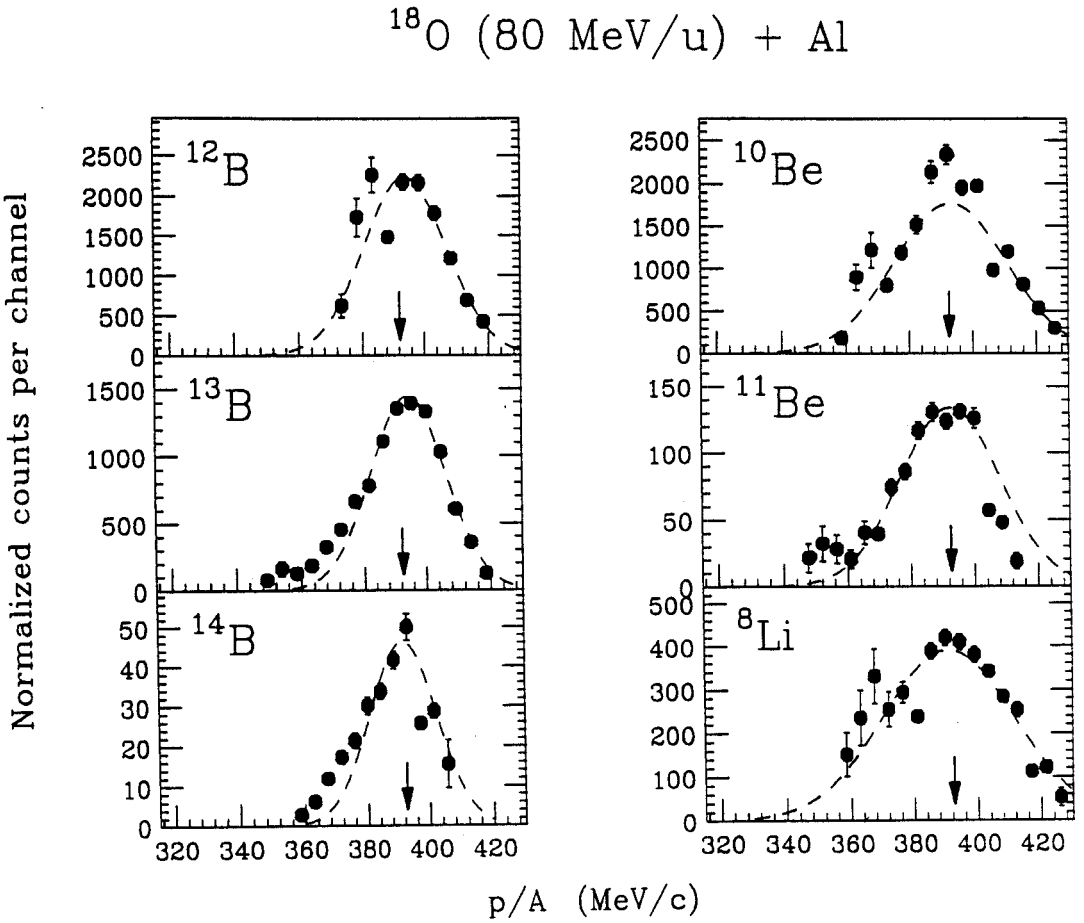


Figure 4.10: Momentum/nucleon distributions of PLFs produced by a $^{18}O$ (80 MeV/u) beam on an $^{27}Al$ target. The arrows correspond to the momentum/nucleon of the beam. The dashed lines are Gaussian functions fitted to the measured distributions.

# Chapter 5

# Results and Discussion

## I Introduction

In this chapter, the characteristics of the distributions of projectile-like fragments obtained from the experiments described in chapters 3 and 4 are presented in a systematic way and are interpreted with simple models. The momentum distributions of the fragments were fitted with Gaussian functions using a simple histogram manipulation code. Care was taken to exclude the tail on the low-momentum side of the distributions, which is attributed to dissipative mechanisms [Blum 86, Borr 86]. The centroids and the widths of the fitted Gaussian distributions were then summarized and analysed. A detailed study of the centroids, the widths and the relative yields of the fragments produced in the reaction of $^{18}$O (80 MeV/u) projectiles with $^{27}$Al target is presented in the following sections, as this data was the most complete of the various systems studied in this work. The characteristics of the distributions from the other measurements were consistent with the $^{18}$O (80 MeV/u) results. A compilation of the centroids of the momentum distributions of nucleon pick-up products from all the reactions studied in this work is given at the end of section II.

# II Study of the centroids of the momentum distributions

## A Nucleon removal products

The centroids of the parallel momentum/nucleon distributions of nucleon removal products from the reaction of $^{18}O$ (80 MeV/u) with $^{27}Al$ is presented in Fig. 5.1. For comparison purposes, the centroids are divided by the momentum/nucleon of the projectile.

The centroids of these distributions are close to the beam momentum/nucleon and do not follow any monotonic dependence on the mass loss $\Delta A$ (the number of nucleons lost by the projectile). This feature is in contrast to that observed in high energy fragmentation reactions in which the centroids decrease with $\Delta A$ (approximately linearly for near-projectile fragments) [Morr 89, Stép 91].

The dependence of the mean momentum/nucleon on mass loss can be derived in a simple way from energy conservation. We assume that the removal of $\Delta A$ nucleons from the projectile requires some "unbinding energy" $E_s$ coming from the projectile initial kinetic energy $T_P$, thus the projectile kinetic energy at the moment of fragmentation is reduced to: $T'_P = T_P - E_s$. Furthermore, we assume that the fragment's mean energy per nucleon, $\langle T_F \rangle / A_F$, is equal to the projectile energy per nucleon at the moment of fragmentation:

$$\frac{\langle T_F \rangle}{A_F} = \frac{T_P - E_s}{A_P} \tag{5.1}$$

The fragment's mean (parallel) momentum/nucleon is, of course, related to its mean kinetic energy/nucleon by the relativistic equation:

$$\frac{\langle p_F \rangle}{A_F} = \frac{1}{c}\sqrt{\frac{\langle T_F \rangle}{A_F}\left(\frac{\langle T_F \rangle}{A_F} + 2m_n c^2\right)} \tag{5.2}$$

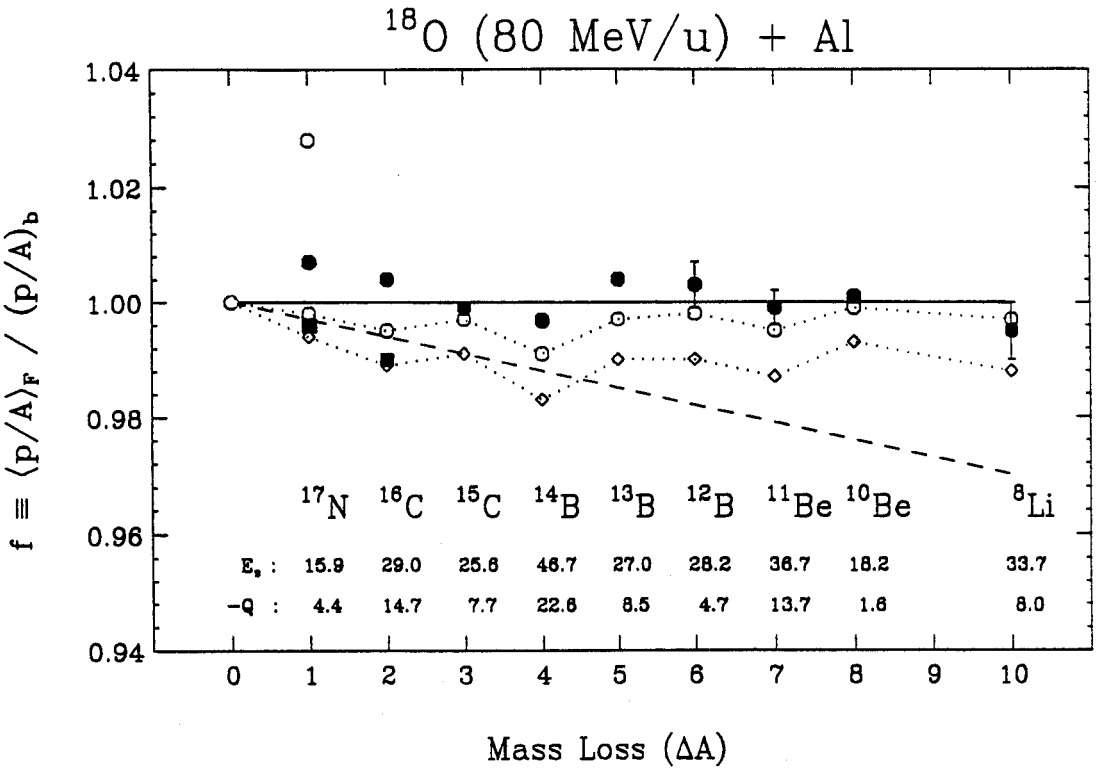


Figure 5.1: Variation of the centroids of the parallel momentum/nucleon distributions of nucleon-removal products from the reaction $^{18}$O (80 MeV/u) + $^{27}$Al. The closed circles are the experimental points. [The two closed squares are from the reaction $^{18}$O (70 MeV/u) + $^{181}$Ta.] The solid line corresponds to the beam momentum/nucleon. The dashed line and the diamonds correspond to calculations according to eq. (5.3) (see text). The open circles represent calculations using eq. (5.5). For a given fragment, the cluster separation energy $E_s$ and the Q-value are given (in MeV) below the isotope symbol (see text).

where $m_n$ is the rest mass of a bound nucleon ($m_n c^2$ = 931.5 MeV). Inserting eq. (5.1) into (5.2), we get:

$$\frac{\langle p_F \rangle}{A_F} = \frac{1}{c}\sqrt{\frac{T_P - E_s}{A_P}\left(\frac{T_P - E_s}{A_P} + 2m_n c^2\right)} \tag{5.3}$$

We can calculate the separation energy $E_s$ in two limits (as already mentioned in chapter 2): first, an independent-particle picture of the projectile nucleus and second, a cluster picture. Assuming that the nucleons are independent particles, they can be removed one after the other and the total energy required is given by:

$$E_s = E_{s,n}\Delta A \tag{5.4}$$

where $E_{s,n}$ is the average separation energy per nucleon (~8 MeV for medium and heavy nuclei). In this case, the mean momentum/nucleon of a fragment is directly related to $\Delta$A. The values calculated according to eq. (5.3), using eq. (5.4) for $E_s$, are given by the straight dashed line in Fig. 5.1.

On the other hand, in the cluster-stripping model, $E_s$ is the energy required to separate the projectile into two bound clusters: the observed fragment $F$ and the removed part $R$. The cluster separation energies $E_s$ for the fragments can be calculated from binding energies (see next section for details) and are listed in Fig. 5.1 below the fragment symbols. The values of the mean momentum/nucleon calculated with this model (shown in Fig. 5.1 by the diamonds) seem to follow the trend of the data, but they are also considerably lower than the experimental points.

The failure of the previous simple approaches to accurately describe the centroids of the momentum distributions led us to take into account the effects of the target in the nucleon removal process (which is traditionally ignored in descriptions of high-energy reactions). In an attempt to describe the variation of the centroids of the nucleon removal products that takes into consideration the presence of the target,

we substituted $-Q$ in eq. (5.3) for $E_s$, where Q is the ground-state Q-value of the two-body projectile–target rearrangement reaction leading to a given fragment. Thus, similar to eq. (5.3), we have:

$$\frac{\langle p_F \rangle}{A_F} = \frac{1}{c}\sqrt{\frac{T_P + Q}{A_P}\left(\frac{T_P + Q}{A_P} + 2m_n c^2\right)} \tag{5.5}$$

The calculated values of the centroids for the reaction of $^{18}O$ (80 MeV/u) on $^{27}Al$ are given in Fig. 5.1 by the open circles. Except for $^{17}N$ and $^{16}C$, very good agreement between the calculated values and the experimental points is obtained, particularly for the variation from nucleus to nucleus. From this comparison we infer that the mean momentum/nucleon of the removal products approximately follows the variation of the Q-value of the corresponding projectile–target rearrangement reaction (rather than the separation energy $E_s$, which is the case in high-energy fragmentation). Interestingly, the mean momentum/nucleon values of $^{17}N$ and $^{16}C$ are higher than that of the projectile (0.7% and 0.4%, respectively). This feature is attributed to the importance of direct transfer (stripping) reaction channels in the observed momentum distributions of these fragments. Such direct transfer contributions are expected to decrease progressively for products further in mass from the projectile.

In order to calculate the mean momentum/nucleon of a projectile-like fragment produced by a two-body transfer reaction, we first apply energy conservation to the projectile–target system and we have:

$$T_P + Q = \langle T_F \rangle + \langle T_{T'} \rangle \tag{5.6}$$

where $\langle T_F \rangle$ and $\langle T_{T'} \rangle$ are the mean kinetic energies of a given fragment and the corresponding target-like residue (which has accepted the nucleons removed from the projectile), respectively. Because we measure the PLF distributions very close to 0 degrees in the lab system, we should expect $\langle T_{T'} \rangle \ll \langle T_F \rangle$. Kinematics calculations

with the code "S320" [Winf 86] for the system $^{18}$O (80 MeV/u) + $^{27}$Al showed that, near 0 degrees, $\langle T_{T'} \rangle$ is about 0.5–1.0 MeV (whereas $\langle T_F \rangle$ is on the order of 1400 MeV). Thus, the PLF has essentially all the initial projectile energy (plus the small negative Q-value due to the two-body rearrangement):

$$\langle T_F \rangle = T_P + Q \tag{5.7}$$

Substituting this expression in eq. (5.2), we get:

$$\frac{\langle p_F \rangle}{A_F} = \frac{1}{c}\sqrt{\frac{T_P + Q}{A_F}\left(\frac{T_P + Q}{A_F} + 2m_n c^2\right)} \tag{5.8}$$

Evaluating eq. (5.8) for $^{17}$N, we get: f $\equiv (\langle p_F \rangle / A_F)/(p_P/A_P) = 1.028$ (see Fig. 5.1) and for $^{16}$C we get: f = 1.057. We see that these values of the mean momentum/nucleon of $^{17}$N and $^{16}$C are higher than the experimental values, whereas the values calculated using eq. (5.5) are lower. Consequently, the observed momentum/nucleon distributions of these products contain a significant contribution from the direct stripping channels, which have mean momentum/nucleon (velocity) higher than that of the beam. Direct transfer (stripping) channels may contribute, to a lesser extent, to the distributions of the other nucleon removal products, since the centroids of their momentum distributions tend to be higher than those calculated according to eq. (5.5).

In contrast to the $^{18}$O (80 MeV/u) + $^{27}$Al system, the centroids of the momentum/nucleon distributions of $^{17}$N and $^{16}$C from the reaction $^{18}$O (70 MeV/u) + $^{181}$Ta are lower than the beam momentum/nucleon, approximately following the predictions of the high-energy model [eq. (5.3)] previously discussed. Consequently, the direct transfer channels are suppressed for this system. Such suppression with the heavier $^{181}$Ta target may be due to the higher Coulomb barrier of the system (72.7 MeV in the lab frame) compared to that of the $^{18}$O + $^{27}$Al system (28.7 MeV).

# B Nucleon pick-up products

The centroids of the momentum/nucleon distributions of the nucleon pick-up products observed in the $^{18}$O (80 MeV/u) + $^{27}$Al experiment are shown in Fig. 5.2 (closed circles). These centroids are considerably below the momentum/nucleon of the beam, in contrast to the case of nucleon-removal products previously discussed.

In order to calculate the centroids of the distributions of the pick-up products, eq. (5.8) can be applied [as previously discussed, the final product is assumed to have essentially all the projectile initial kinetic energy (actually $\langle T_F \rangle = T_P + Q$)]. The calculations according to eq. (5.8) are shown in Fig. 5.2 by the open circles.

For $^{19}$O, the calculated value (f = 0.969) agrees very well with the experimental value (f = 0.971). Thus, we conclude that $^{19}$O is mostly produced by the direct reaction: $^{27}$Al($^{18}$O,$^{19}$O)$^{26}$Al (Q = −9.1 MeV).

For $^{18}$N, the calculated value (f = 0.993) is ∼1% higher than the experimental value (f = 0.984). In this case, the exchange reaction $^{27}$Al($^{18}$O,$^{18}$N)$^{27}$Si (Q = −18.7 MeV) may only partially contribute to the observed momentum distribution. In addition, we can suppose that $^{18}$N is also produced by a two-step mechanism consisting of a break-up of $^{18}$O to $^{17}$N and a neutron pick-up by $^{17}$N. According to this mechanism, the mean kinetic energy of $^{17}$N produced in the first step can be calculated as discussed previously for the nucleon removal products. For the second step, represented by the pick-up reaction $^{27}$Al($^{17}$N,$^{18}$N)$^{26}$Al (Q = −10.2 MeV), the mean kinetic energy of $^{18}$N can be calculated from eq. (5.7) where, instead of $T_P$ we insert the mean kinetic energy of $^{17}$N calculated in the break-up step. Then, from eq. (5.2), the mean momentum/nucleon of this procuct can be calculated and is found to be (f = 0.965) ∼2% lower than the experimental value. Consequently, we conclude that (at least) both mechanisms (the nucleon exchange mechanism and the break-up+pick-up

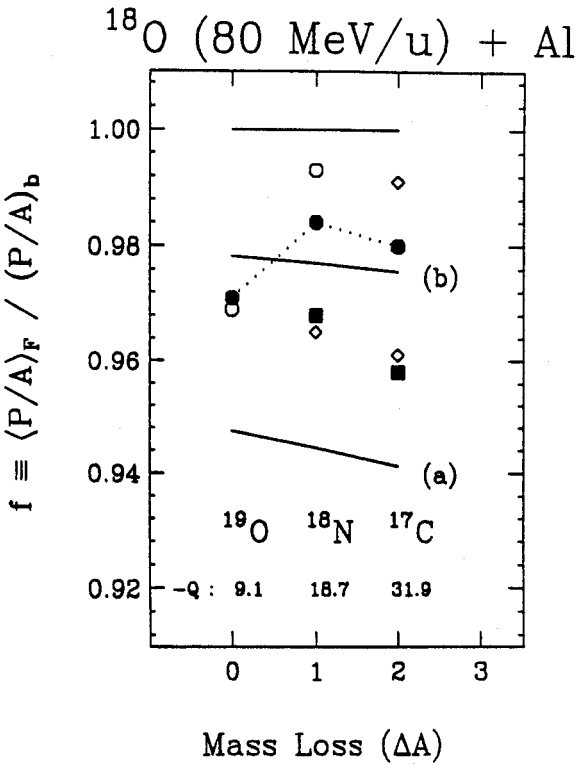


Figure 5.2: Variation of the centroids of the parallel momentum/nucleon distributions of nucleon pick-up products from the reaction $^{18}$O (80 MeV/u) + $^{27}$Al. The closed circles are the experimental points. [The two closed squares are from the reaction $^{18}$O (70 MeV/u) + $^{181}$Ta.] The horizontal straight line corresponds to the beam momentum/nucleon. The open circles are calculations assuming a single-step transfer reaction [the Q-values are given (in MeV) below the isotope symbols]. The diamonds are calculations assuming a two-step mechanism: break-up + pick-up (see text). The inclined straight lines are calculations according to a simple model based on momentum conservation (see text).

mechanism) contribute to the production of $^{18}$N nuclei.

A similar analysis can be followed for the $^{17}$C case and similar conclusions can be drawn. Assuming the two-body transfer reaction $^{27}$Al($^{18}$O,$^{17}$C)$^{28}$P (Q = −31.9 MeV), the calculated mean momentum/nucleon (f = 1.018, not shown in Fig. 5.2) is ∼4% higher than the experimental value (f = 0.980). Assuming a two-step mechanism involving, first, a break-up of $^{18}$O to $^{16}$C and then a neutron pick-up by $^{16}$C: $^{27}$Al($^{16}$C,$^{17}$C)$^{26}$Al (Q = −12.3 MeV), the calculated value (f = 0.959) is ∼2% lower than the experimental one. Alternatively, assuming a different two-step reaction involving, first, a break-up of $^{18}$O to $^{17}$N and then, a nucleon exchange reaction to $^{17}$N: $^{27}$Al($^{17}$N,$^{17}$C)$^{27}$Si (Q = −18.0 MeV), the calculated value (f = 0.991) is now ∼1% higher than the experimental value.

It should be noted that the experimental values of the mean momentum/nucleon of $^{18}$N and $^{17}$C from the $^{18}$O (70 MeV/u) + $^{181}$Ta reaction are well described by a mechanism involving, first, the fragmenation (break-up) of $^{18}$O to $^{17}$N and $^{16}$C, respectively, and second, a neutron pick-up by these intermediate fragments. The mechanisms involving the exchange reactions previouly discussed are, once again, suppressed in the case of the $^{181}$Ta target. From this we conclude that, apart from the case of $^{19}$O, more than one channel is involved in the production of the nucleon pick-up products.

Considering the complicated nature of the production mechanism of the nucleon pick-up products, a simple model able to predict the general behaviour of the mean momentum/nucleon of these products is desirable. For this purpose, we developed a simple mechanical model of the pick-up process based on momentum conservation. According to this model, the mean (parallel) momentum $\langle p_F \rangle$ of the observed

fragment $F$ is written as:

$$\langle p_F \rangle = \langle p_{PF} \rangle + \langle p_t \rangle \tag{5.9}$$

where $\langle p_{PF} \rangle$ is the mean momentum of the projectile part (with mass $A_{PF}$) of the observed fragment which is assumed to have, on average, the momentum/nucleon (velocity) of the projectile. Thus:

$$\langle p_{PF} \rangle = A_{PF} \frac{p_P}{A_P} \tag{5.10}$$

and $\langle p_t \rangle$ is the mean momentum of the nucleon (or nucleons) picked-up from the target. If we assume that the transfered nucleon is picked-up randomly from the target (thus, $\langle p_t \rangle = 0$), then the mean momentum/nucleon of the fragment is, according to eq. (5.9) and (5.10):

$$\frac{\langle p_F \rangle}{A_F} = \frac{A_{PF}}{A_F} \frac{p_P}{A_P} \tag{5.11}$$

The calculated values according to this equation are represented by the solid line labeled (a) in Fig. 5.2 and are much lower than the experimental values. However, if the nucleon is assumed to be picked-up from the target with momentum, on average, equal to the typical nuclear Fermi momentum (230 MeV/c) oriented along the direction of the projectile motion (thus, $\langle p_t \rangle = p_{Fermi}$), then the mean momentum/nucleon of the fragment is:

$$\frac{\langle p_F \rangle}{A_F} = \frac{1}{A_F} \left( A_{PF} \frac{p_P}{A_P} + p_{Fermi} \right) \tag{5.12}$$

The values calculated according to eq. (5.12) are given by the solid line labeled (b) in Fig. 5.2 and are in good agreement (within $\pm 0.5\%$) with the experimental points. Consequently, the downshift of the mean momentum/nucleon of the pick-up products can be described in a simple way by momentum conservation and the

additional assumption that the nucleon is picked-up from the target preferentially with momentum equal to the nuclear Fermi momentum oriented along the direction of the projectile motion.

This model also applies to pick-up products where more than one nucleon is picked-up from the target. If the number of picked-up nucleons is $\Delta A_t$, then similar to eq. (5.12), we have:

$$\frac{\langle p_F \rangle}{A_F} = \frac{1}{A_F}\left[(A_F - \Delta A_t)\,\frac{p_P}{A_P} + \Delta A_t\, p_{Fermi}\right] \tag{5.13}$$

where we have used the relation: $A_{PF} = A_F - \Delta A_t$ for the mass of the projectile part of the final fragment. Rearranging this equation we get:

$$\frac{\langle p_F \rangle}{A_F} = \frac{p_P}{A_P} - \frac{\Delta A_t}{A_F}\left(\frac{p_P}{A_P} - p_{Fermi}\right) \tag{5.14}$$

which, for a given projectile energy, has a linear dependence of the mean momentum/nucleon on $\Delta A_t/A_F$. A compilation of the centroids of the momentum/nucleon distributions of few-nucleon (up to 3) pick-up products obtained from the experiments described in chapters 3 and 4 is presented in Fig. 5.3. The centroids are divided by the momentum/nucleon of the corresponding beam and are given as function of the ratio $\Delta A_t/A_F$. The experimental points are shown by the closed symbols and the calculated values [according to eq. (5.14)] are shown by the corresponding open symbols. The overall agreement of the calculation with the experimental values is very good.

# III Study of the widths of the momentum distributions

The variation of the widths of the (parallel) momentum distributions of projectile-like fragments from the reaction of $^{18}$O (80 MeV/u) with $^{27}$Al is presented in Fig. 5.4 as

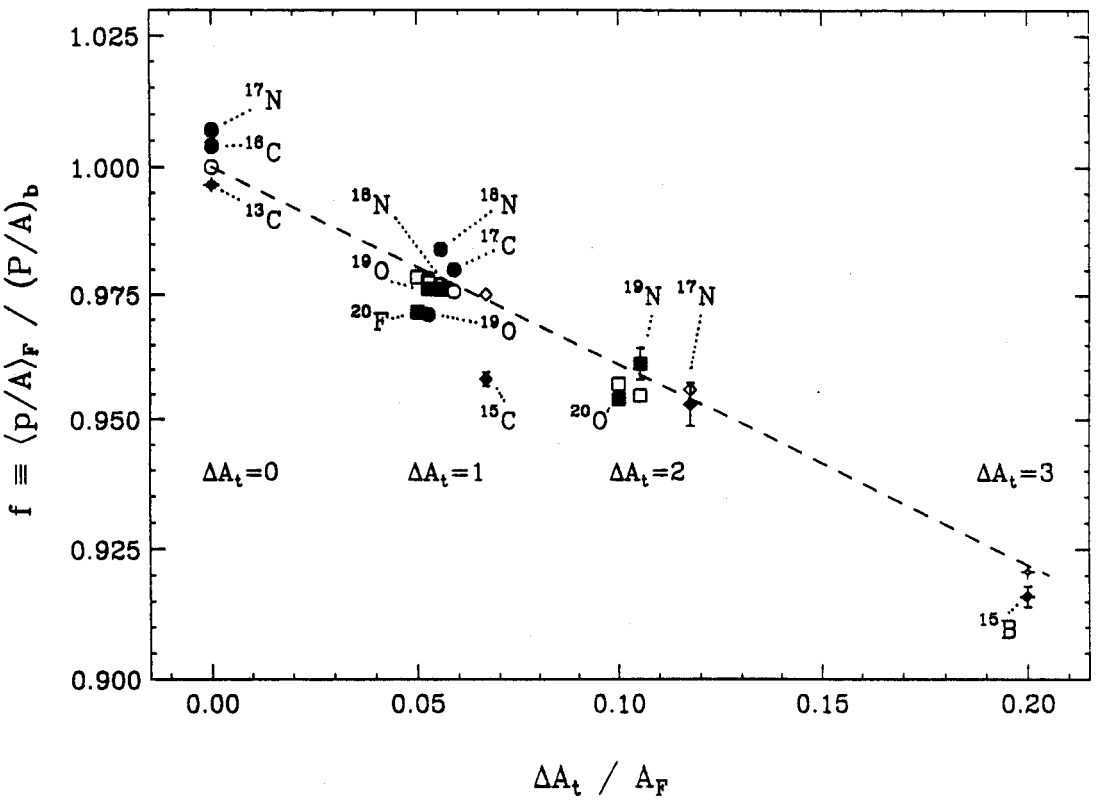


Figure 5.3: Variation of the centroids of the momentum/nucleon distributions of few-nucleon pick-up products from the reactions studied in the present work. The experimental points are shown by the closed symbols. The open symbols are calculated according to eq. (5.14). Specifically, the symbols correspond to the different reactions as follows: circles: $^{18}$O (80 MeV/u) + $^{27}$Al, squares: $^{20}$Ne (85 MeV/u) + $^{181}$Ta, diamonds: $^{15}$N (70 MeV/u) + $^{181}$Ta, and crosses: $^{14}$N (75 MeV/u) + $^{27}$Al (chapter 3). The straight line represents the general trend of the data.

a function of the mass loss $\Delta A$ (closed points). Both nucleon removal and nucleon pick-up products are included in the figure. Calculations of the widths performed with the simple models of Goldhaber and Friedman are presented in subsections A and B, respectively.

## A Calculations of the widths with Goldhaber's model

According to the independent-particle model of Goldhaber [Gold 74] (discussed in chapter 2), the width of the (parallel) momentum distribution of nucleon removal products is given by:

$$\sigma^2 = \sigma_0^2 \frac{A_F(A_P - A_F)}{A_P - 1}. \tag{5.15}$$

For the present system, we evaluated this equation using a reduced width $\sigma_0 = 80$ MeV/c. The calculated values of the widths are indicated in Fig. 5.4 by the lower dashed line and are in very good agreement with the data. It should be pointed out that the reduced width obtained from the present measurement agrees very well with the values previously obtained from the fragmentation data of $^{16}$O and $^{12}$C projectiles at relativistic energies [Grei 75] (see Table 2.1 and discussion in chapter 2).

Interestingly, the width of the momentum distribution of $^{17}$N is ~20% higher than predicted by eq. (5.15). This discrepancy is not present in the case of $^{17}$N fragments produced by the reaction $^{18}$O (70 MeV/u) + $^{181}$Ta (indicated in fig. 5.4 by the closed square). The broadening of the momentum distribution of $^{17}$N fragments with $^{27}$Al target is once again attributed to a considerable contribution of a direct stripping channel, along with the fragmentation (break-up) channel, to the momentum distribution of $^{17}$N. The component of the momentum distribution due to the stripping channel [Merm 86] peaks at momentum higher than that of the fragmentation channel (see also previous section), thus the overall momentum distribution is broader

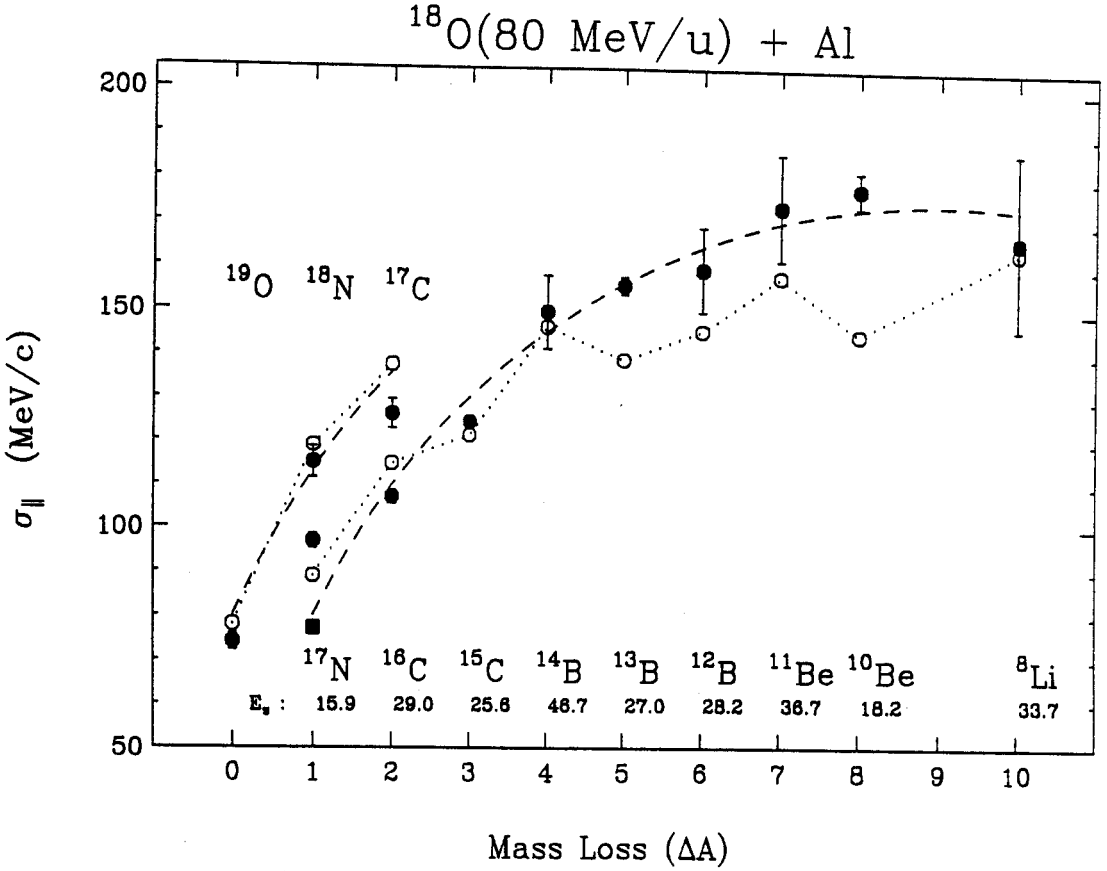


Figure 5.4: Variation of the widths of the parallel momentum distributions of projectile-like fragments from the reaction $^{18}$O (80 MeV/u) + $^{27}$Al. The closed circles are the experimental points. [The closed square is from the reaction $^{18}$O (70 MeV/u) + $^{181}$Ta.] The lower dashed line is calculated with Goldhaber's model [Gold 74]. The upper dashed line is from an extended version of Goldhaber's model for nucleon pick-up products. The open circles are calculations with Friedman's model [Frie 83]. For the nucleon removal products, the cluster separation energies $E_s$ are given (in MeV) below the isotope symbols.

than that of the fragmentation channel alone. The stripping channel is suppressed when $^{181}$Ta target is used and the width is in agreement with the value calculated with the fragmentation model.

The widths of the momentum distributions of the neutron pick-up products are larger than their corresponding fragmentation products (e.g. in Fig. 5.4 compare the widths of $^{18}$N and $^{17}$C with those of $^{17}$N and $^{16}$C, respectively). In order to interpret the increase in the width of the momentum distribution of a product that has picked-up a nucleon from the target, we propose an extension of Goldhaber's model in which we take into account the nucleon momentum distribution in the target nucleus, along with that in the projectile nucleus. The momentum distribution of a pick-up product is assumed to result from the folding of two distributions: first, the momentum distribution of the projectile part of the final fragment and second, the momentum distribution of the nucleon(s) picked-up from the target. These distributions are assumed to be Gaussian distributions with widths expressed as in eq. (5.15). The momentum distribution of the final product is also Gaussian that has a width given by the quadratic addition of the values from the previous two distributions. Thus:

$$\sigma^2 = \sigma_0^2 \frac{A_{PF}(A_P - A_{PF})}{A_P - 1} + \sigma_0^2 \frac{\Delta A_t (A_T - \Delta A_t)}{A_T - 1} \tag{5.16}$$

where $A_{PF} = A_F - \Delta A_t$ is the mass of the projectile part of the final product and $\Delta A_t$ is the number of nucleons picked-up from the target ($A_T$ is the mass of the target). In writing eq. (5.16) we have implicitly assumed that the nucleon momentum distribution in the target is the same as that in the projectile nucleus and therefore, we have used the same reduced width $\sigma_0$ for both the projectile and the target. The widths of the momentum distributions of the neutron pick-up products calculated according to eq. (5.16) with $\sigma_0 = 80$ MeV/c are indicated in Fig. 5.4 by the upper dashed line and are in good agreement with the experimental values.

From this discussion, we conclude that the independent-particle model can well account for the widths of the parallel momentum distributions of both nucleon removal and nucleon pick-up products. For the pick-up products, we must take into account the nucleon momentum distributions in both the projectile and the target.

The behaviour of the widths of the parallel momentum distributions of nucleon removal and nucleon pick-up products shows that the width observable is rather insensitive to the detailed course of the production mechanism. This statement is also true for the widths of fragmentation products obtained at high energies (see chapter 2).

## B Calculations of the widths with Friedman's model

Apart from the calculations with the independent-particle model, we performed calculations of the widths using the cluster-stripping model of Friedman [Frie 83] (discussed in chapter 2) which are shown in Fig. 5.4 by the open circles. For the nucleon removal products, eq. (2.15) was applied. For a given fragment, the separation energy $E_s$ of the system $F \dot{-} R$ was calculated from the change in binding energy between the projectile and the system $F$–$R$: $E_s = B_P - (B_F + B_R)$, where "$B$" stands for binding energy. The cluster separation energies $E_s$ are given in Fig. 5.4 below the isotope symbols. Examples of break-up patterns for several products are given in Table 5.1.

Table 5.1: Examples of break-up patterns of $^{18}$O projectiles. $E_s$ are the corresponding separation energies. The last line is the one-neutron stripping pattern from $^{27}$Al target.

| | | | |
|---|---|---|---|
| $^{18}$O | $\longrightarrow$ | $^{17}$N + p | $E_s$ = 15.9 MeV |
| $^{18}$O | $\longrightarrow$ | $^{13}$B + $^{4}$He + p | $E_s$ = 27.0 MeV |
| $^{18}$O | $\longrightarrow$ | $^{10}$Be + 2 $^{4}$He | $E_s$ = 18.2 MeV |
| $^{18}$O | $\longrightarrow$ | $^{8}$Li + $^{10}$B | $E_s$ = 33.7 MeV |
| $^{27}$Al | $\longrightarrow$ | $^{26}$Al + n | $E_s$ = 13.0 MeV |

In calculating $E_s$, we chose the break-up pattern (if more than one for a given fragment) which corresponded to the lowest $E_s$; that is, we assumed that the clusters stripped from the projectile are the most bound. The widths calculated according to Friedman's model are also in good agreement with the experimental data, especially for products close to the projectile (up to $^{14}$B, see Fig. 5.4). For the other nucleon removal products, the calculated widths are somewhat lower than the experimental values. For example, a low width value is calculated for $^{10}$Be and is due to the small separation energy required to break $^{18}$O into $^{10}$Be and two alpha particles ($E_s$ = 18.2 MeV). Thus, we conclude that the cluster stripping patterns assumed in the calculation (having the lowest possible $E_s$) are not the only fragmentation pathways leading to the production of the fragments. Apart from the cluster stripping channels, other fragmentation channels involving first, the production of excited primary fragments and second, their subsequent decay by particle evaporation contribute to the production mechanism (see also chapter 2).

In order to calculate the widths of the momentum distributions of the nucleon pick-up products using Friedman's model, we proposed an extension of the model similar to that of Goldhaber's model discussed previously. We again assumed that the momentum distribution of a pick-up product results from the combination of the momentum distribution of the projectile part of the product [with width $\sigma_{PF}$ given by eq. (2.15)] and the momentum distribution of the nucleon (or cluster of nucleons) picked-up from the target [with width $\sigma_t$ given again by eq. (2.15) applied to the stripping of the nucleon (or cluster) from the target]. The width of the combined momentum distribution is given by the quadratic addition of the two widths:

$$\sigma^2 = \sigma_{PF}^2 + \sigma_t^2. \tag{5.17}$$

For the neutron pick-up products of the present data, $\sigma_{PF}$ is taken from the

corresponding nucleon removal products and $\sigma_t$ is calculated from eq. (2.15) applied to the neutron stripping from the target (see Table 5.1). The widths calculated according to eq. (5.17) are shown in Fig. 5.4 and are in good agreement with the experimental values.

The agreement of the measured widths of the momentum distributions of nucleon pick-up products with Goldhaber's model and Friedman's model calculations suggests that the widths of these products can be very well predicted by taking into account the momentum distributions of both the projectile part and the picked-up part of the observed fragment.

# IV Study of Relative Yields

The relative yields of projectile-like fragments produced by the reaction $^{18}O$ (80 MeV/u) + $^{27}Al$ are presented in Fig. 5.5 by the closed circles. The yields were obtained by integrating the measured momentum distributions of the fragments (and are expressed in total normalized counts).

Calculations of the yields with the abrasion-ablation model are shown in Fig. 5.5 by the diamonds. For the abrasion stage of the calculation we assumed proton–neutron correlations according the the giant-dipole-resonance (GDR) model [Morr 79] (see also chapter 2). As natural for an abrasion-ablation calculation, no nucleon pick-up products were predicted by the model. For the nucleon removal products, the predictions of the code are not in agreement with the present data.

Calculations of the yields with the INC model are shown in Fig. 5.5 by the crosses. The INC code "ISABEL" of Yariv and Fraenkel [Yari 79] (see also chapter 2) was used for the nucleon-removal step of the reaction. For the deexcitation step, a statistical evaporation code was used to calculate the cross sections of the fragments.

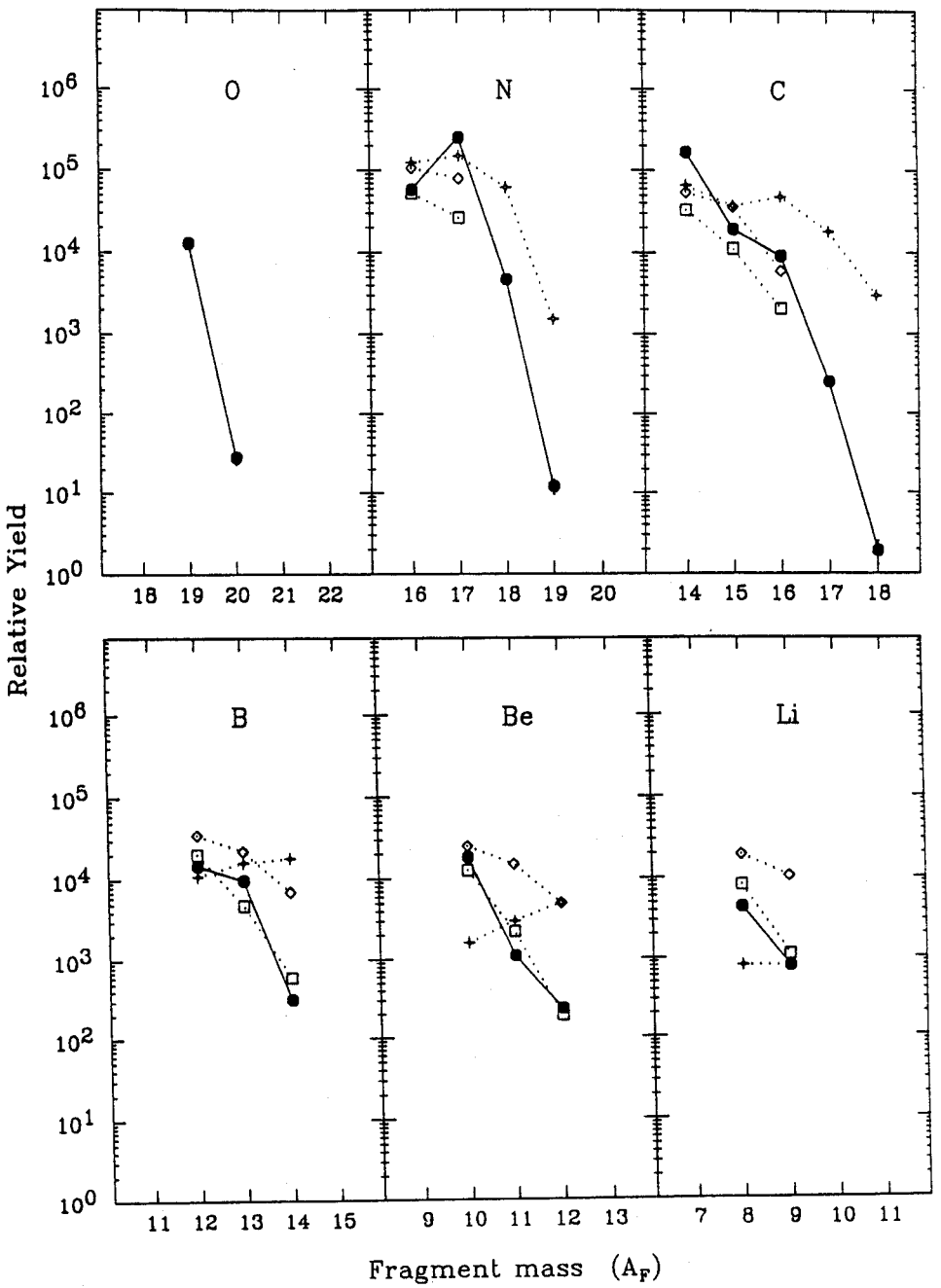


Figure 5.5: Relative yields of projectile-like fragments from the reaction $^{18}O$ (80 MeV/u) + $^{27}Al$. The closed circles are the experimental points. The diamonds and the crosses are calculations with the abrasion–ablation model [Morr 79] and the INC model [Yari 79], respectively. The squares are predictions of a high-energy parametrization [Sümm 90].

Interestingly, nucleon pick-up products are predicted by the model for the present intermediate-energy reaction (as a result of nucleon exchange due to nucleon–nucleon collisions in the overlap stage of the process). However, the agreement of the calculated yields with the trend of the data is rather poor. It should also be mentioned that the calculation predicted the centroids and the widths of the parallel momentum distributions of the fragments; the centroids were much lower than the experimental points and the widths were larger. From these results, we infer that the INC calculation for the present system seems to overestimate the excitation energy of the primary fragments [in contrast to the case of PLFs from the heavy beam $^{84}$Kr (200 MeV/u) [Stép 91] for which the code gave predictions in agreement with the data].

In addition, we performed calculations of the yields with the high-energy empirical parametrization of Sümmerer and Morrissey [Sümm 90], shown in Fig. 5.5 by the squares. This parametrization has been obtained from target fragments produced at high energies (>1 GeV/u). The present calculations were performed with the code "INTENSITY" [Wing 91] which, at present, uses this high-energy parametrization (for lack of an appropriate intermediate-energy parametrization) to predict rates of radioactive beams of PLFs separated by the A1200. The predictions of this calculation agree with the trend of the data only for fragments far in mass from the projectile (i.e. B, Be, Li).

Finally, we performed calculations of the relative yields of the nucleon removal products with Friedman's model [Frie 83] (see also chapter 2) using eq. (2.16). The parameter $b$ was obtained from the slope of the function $W = \ln(\gamma_{exp} x_0^3 / S(Z_R, A_R))$ versus $2\alpha x_0$ [eq. (2.17)]. The plot of this function for the present data set is given in Fig. 5.6 and shows a good linear behaviour for most of the fragments. A value $b = 0.57$ for the cut-off parameter is obtained from the slope of the least-squares-fit straight line. It should be noted that this value is higher than the value proposed

by Friedman ($b = 0.4$) for the fragmentation products of relativistic $^{12}C$ and $^{16}O$ [Frie 83]. Also, the present data show a better linear correlation for W than the data of relativistic $^{16}O$ (see Fig. 4 in Frie 83).

Using the extracted value of $b$ in eq. (2.16) and normalizing the calculated yields with respect to the experimental yield of $^{17}N$, the relative yields of the nucleon removal products were obtained (shown in Fig. 5.7 by the open circles) and are in good agreement with the data.

In order to calculate the relative yields for the nucleon pick-up products, we assumed that the yield $\gamma_F$ of a given fragment can be expressed as:

$$\gamma_F = \gamma_{PF}\,\gamma_t \tag{5.18}$$

where $\gamma_{PF}$ is the yield of the projectile part of the fragment, and $\gamma_t$ is the yield for the removal of a nucleon (or cluster) from the target. Both factors are calculated according to eq. (2.16) applied to the corresponding system. Thus, the factor $\gamma_{PF}$ can be taken from the corresponding nucleon removal products and $\gamma_t$ is calculated for the stripping of the neutron(s) from the target. Because each of the factors appearing in eq. (5.18) requires [according to eq. (2.16)] a different normalization, we need one more normalization factor for the nucleon pick-up products. In addition, for the case of $^{19}O$ and $^{20}O$, where no nucleon removal occurs, a different normalization should be necessary. In this case we normalized the relative yields according to $^{19}O$. For the relative yield calculation of $^{18}N$, $^{19}N$, $^{17}C$ and $^{18}C$, normalization of the yields relative to $^{18}N$ was performed. The calculated values, shown in Fig. 5.7 by the open diamonds, are in good agreement with the data. Thus, an extension of Friedman's model in the form of eq. (5.18) gives a good description of the ratio of yields of pick-up products with different numbers of nucleons transfered (here for 1 and 2 neutrons). As already has been mentioned in chapter 2, absolute cross section predictions are

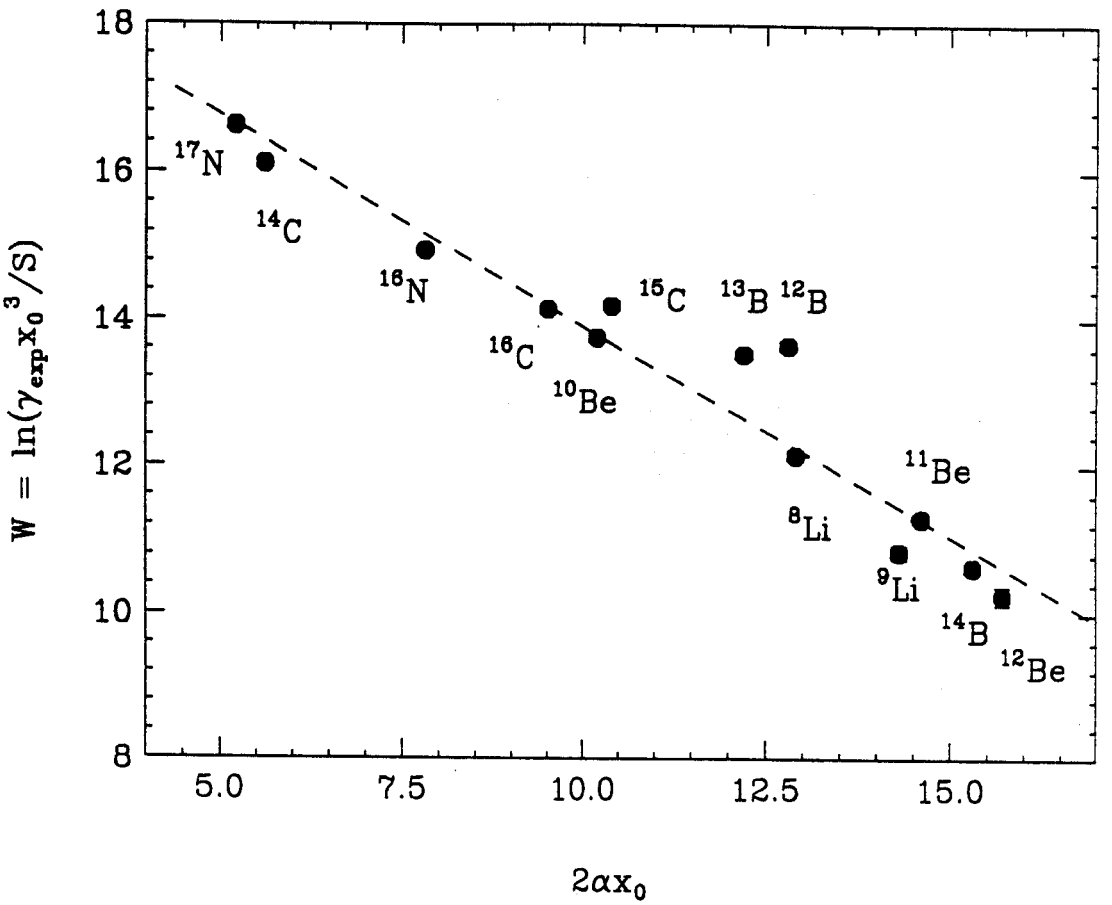


Figure 5.6: Plot of the function $W = \ln(\gamma_{exp} x_0^3/S)$ versus $2\alpha x_0$ for the yields of projectile-like fragments from the reaction $^{18}$O (80 MeV/u) + $^{27}$Al. The dashed line is a least-squares fit to the data points.

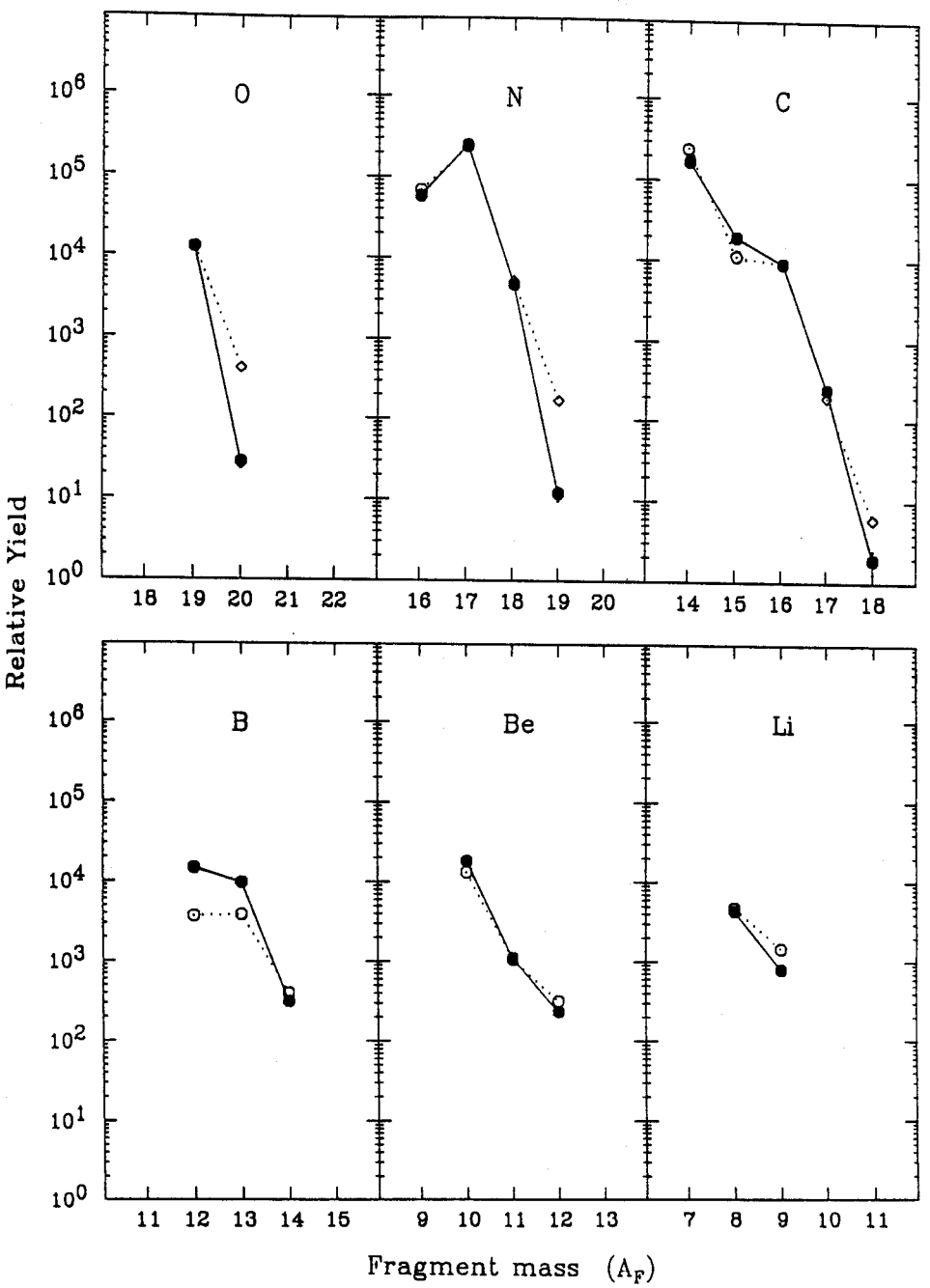


Figure 5.7: Comparison of the relative yields of PLFs from the reaction $^{18}O$ (80 MeV/u) + $^{27}Al$ with calculations using Friedman's model [Frie 83]. The closed circles are the experimental points. The open circles are Friedman's model calculations for the nucleon-removal products and the diamonds are calculations for the pick-up products (see text).

not possible with Friedman's model, due to the neglect of the impact parameter of the collision.

In conclusion, the relative yields of projectile-like fragments cannot be well described by either the abrasion-ablation model or the intranuclear cascade model. The INC model predicts the production of nucleon pick-up products at the present energy (80 MeV/u), but the calculations are higher than the experimental values. Interestingly, the cluster-stripping model of Friedman gives a good description of the relative yields in most of the cases and especially for fragments close in mass to the projectile. From these observations we can also infer that the projectile-like fragments of the present light beam are produced with a break-up (and/or pick-up) mechanism possibly involving low excitation energies. This conclusion is similar to that reached for data from other light projectiles at lower bombarding energies (see chapter 2).

# Chapter 6

# Summary and Conclusions

In this dissertation, a study of the projectile fragmenation process in the intermediate energy regime was presented. A review of the experimental and theoretical progress concerning the fragmentation reactions was presented in chapter 2. The characteristics of projectile-like fragments, the basic models developed to interpret the data and our present understanding of the fragmentation mechanism were discussed.

The experimental measurements of the present work (presented in chapters 3 and 4) were motivated by the need of systematic data of projectile fragments near 0 degrees produced by intermediate-energy beams. Because of the presence of the primary beam, accurate measurements at and near 0 degrees are especially difficult and require the use of 0-degree spectrometers. In the present work, two different devices were operated as 0-degree spectrometers: the K1200 interim beamline and the A1200 mass separator.

The operation of the K1200 interim beamline as a spectrometer was presented in chapter 3. Beam optics calculations showed that a moderate acceptance mode was possible for this simple device. The fragments were detected at the end of the beamline, inside the 92" scattering chamber with a detection system consisting of two position-sensitive detectors and a $\Delta E$–$E$ plastic scintillator telescope. The reactions

studied were $^{14}$N (75 MeV/u) + $^{27}$Al and $^{181}$Ta. Momentum and reaction-angle of the fragments were reconstructed. The momentum distributions of the fragments at 0°, 1° and 2° and their angular distributions were obtained from the data. Nucleon-removal and nucleon pick-up products were observed in the experiment. Unfortunately, the quality of the results of these measurements was limited first, due to poor TOF measurement which hindered a clear isotope identification and second, due to a limited resolution of the reconstructed momentum and reaction angle of the particles. However, the experiment and the analysis of the data were very instructive and valuable, providing preparation and experience for the subsequent experiments with the A1200.

The measurements of projectile fragmentation distributions with the A1200 beam analysis device were presented in chapter 4. The A1200 was operated in the achromatic medium acceptance mode, which has two intermediate dispersive images and a final achromatic image. Fragmentation targets were placed at the beginning of the device and the products were detected at the final-image detector array consisting of two $X$–$Y$ position detectors and a $\Delta E$–$E$ telescope. Momentum information was obtained from position measurement at the second intermediate image with a third position detector. In a first series of measurements, PLF distributions from the following reactions were measured: $^{20}$Ne (85 MeV/u) + $^{9}$Be and $^{181}$Ta, $^{15}$N (70 MeV/u) + $^{181}$Ta and $^{18}$O (70 MeV/u) + $^{181}$Ta. The results of these measurements were limited, mainly due to problems in the relative normalization of the data runs. Nevertheless, several good momentum distributions were obtained from these data sets. At a later time, a detailed measurement of PLFs from the reaction $^{18}$O (80 MeV/u) + $^{27}$Al was performed which focused on measuring the 0-degree momentum distributions of neutron-rich projectile-like fragments. As additional experience operating the A1200 had been obtained, this measurement turned out to be the most complete and successful of the present work and a detailed analysis and interpretation of its results

were presented in chapter 5. The measured 0-degree momentum distributions of nucleon removal and nucleon pick-up products were fitted with Gaussian functions and the extracted centroids and widths were subsequently analysed.

The centroids of the momentum/nucleon distributions of the nucleon removal products from the reaction $^{18}O$ (80 MeV/u) + $^{27}Al$ were very close to the beam momentum/nucleon. They did not decrease monotonically with respect to the mass loss (as has been observed at high energies), but they followed the variation of the ground-state Q-value of the two-body rearrangement reactions leading to the different fragments. For PLFs very close to the projectile, the centroids were higher than the beam momentum/nucleon. This observation was attributed to the contribution of a direct stripping channel, along with the fragmentation (break-up) channel to the production of these fragments. On the other hand, the centroids of the nucleon pick-up products were remarkedly lower than the beam momentum/nucleon. This feature was interpreted by the kinematics of direct pick-up and/or break-up+pick-up channels which, depending on the situation, were assumed to contribute to the observed momentum distributions. In addition, the direct channels were found to be dramatically suppressed when the heavy $^{181}Ta$ target was used.

The general behaviour of the centroids of the nucleon pick-up products was found to follow the predictions of a simple mechanical model based on momentum conservation and the additional assumption that the nucleon(s) picked-up from the target have preferentially momenta (on average) equal to the nuclear Fermi momentum oriented in the direction of the projectile motion. This behaviour was found to be common for all the nucleon-pickup products observed in the experiments of the present work.

The widths of the momentum distributions of the nucleon removal products were in good agreement with the predictions of the independent-particle model of Goldhaber [Gold 74] with a reduced width $\sigma_0 = 80$ MeV/c. However, the widths of the

nucleon pick-up products were larger than the corresponding removal products and found to be well described if the momentum distributions of both the projectile part and the picked-up nucleon(s) were taken into account. Similar to Goldhaber's model, the cluster stripping model of Friedman [Frie 83] gave good predictions of the widths, especially for fragments very close to the projectile.

Finally, the relative yields of projectile-like fragments from the reaction $^{18}O$ (80 MeV/u) + $^{27}Al$ were obtained. Calculations with the abrasion-ablation model and the intranuclear cascade model gave a rather poor agreement with the trend of the data. However, calculations of the relative yields with Friedman's model were, in most of the cases, in good agreement with the experimental values. These facts imply that a break-up (and/or pick-up) mechanism possibly involving low excitation energy is responsible for the production of projectile-like fragments from the present light projectile.

In conclusion, the results of the present study demonstrated a number of important features of projectile-like fragments produced from light projectiles at intermediate energies. Along with the fragmentation (break-up) channel, direct transfer channels (stripping and/or pick-up) have a considerable contribution to the production of the fragments. Due to the inclusive character of the present measurements, a separation of the different reaction channels was not possible. However, assuming their contributions and using simple models, we were able to adequately describe the observations.

A study of the relative contributions of the break-up and transfer channels to the production of projectile-like fragments requires exclusive measurements. For example, measurements of PLFs in coincidence with charged particles can yield quantitative information about the various mechanisms. At present, very few measurements of this type exist in the literature.

It should be pointed out that our present systematics and understanding of the mechanisms of intermediate energy fragmentation are far from complete. Further extended measurements of PLF distributions should be performed at and near 0 degrees in order to obtain detailed systematics of the observables, test the applicability of existing models and motivate additional theoretical work on the reaction dynamics of peripheral collisions at the intermediate energy regime.

Apart from a reaction dynamics standpoint, a detailed systematics and understanding of the production mechanism of PLFs at intermediate energies are extremely valuable for the development of radioactive nuclear beams, allowing trustworthy predictions of production rates and other important properties to be made.

# Appendix A

# Derivation of Equations of Fragmentation Models

In this appendix, a derivation of the equations of two simple fragmentation models, namely, Goldhaber's model and Friedman's model are presented in detail. These models have been discussed in chapter 2.

## I Goldhaber's Model

Assuming a sudden fragmentation picture and applying momentum conservarion to the fragmenting projectile nucleus (or, equivalently, target nucleus) in its own rest frame, we have

$$\sum_{i=1}^{A_P} \vec{p}_i = 0 \tag{A.1}$$

where $\vec{p}_i$ denotes the momentum of the $i$-th nucleon of the projectile. Taking the square of this expression, we get

$$\sum_{i=1}^{A_P} p_i^2 + \sum_{i \neq j}^{A_P} \vec{p}_i \cdot \vec{p}_j = 0. \tag{A.2}$$

Taking the average of the terms of this equation and performing the summations we get

$$A_P \langle p_i^2 \rangle + \binom{A_P}{2} \langle \vec{p}_i \cdot \vec{p}_j \rangle = 0. \tag{A.3}$$

For the momentum $p_F$ of a projectile fragment with mass $A_F$, we have

$$\vec{p_F} = \sum_{i=1}^{A_F} \vec{p_i}. \tag{A.4}$$

Squaring this equation and evaluating the average values of the resulting terms we get

$$\langle p_F^2 \rangle = A_F \, \langle p_i^2 \rangle + \binom{A_F}{2} \langle \vec{p_i} \cdot \vec{p_j} \rangle. \tag{A.5}$$

Solving eq. (A.3) for $\langle \vec{p_i} \cdot \vec{p_j} \rangle$, substituting into eq. (A.5), (implicitly assuming that the internal nucleon motion of the nucleous does not change upon fragmentation), and performing the algebraic manipulations with the combinatorials, we arrive at the following expression for $\langle p_F^2 \rangle$ :

$$\langle p_F^2 \rangle = \langle p_i^2 \rangle \, \frac{A_F(A_P - A_F)}{A_P - 1}. \tag{A.6}$$

This equation relates the average-square momentum $\langle p_F^2 \rangle$ of the observed fragment with the average-square momentum $\langle p_i^2 \rangle$ of the nucleon motion inside the projectile (also denoted as $\langle p_n^2 \rangle$). Assuming isotropy, the projection of the fragment momentum distribution on any axis will be a Gaussian function with width $\sigma$ related with the average-square fragment momentun via: $\langle p_F^2 \rangle = 3\sigma^2$. Inserting this expression in eq. (A.6), we get the following equation for the width:

$$\sigma^2 = \sigma_0^2 \, \frac{A_F(A_P - A_F)}{A_P - 1} \tag{A.7}$$

where the reduced width $\sigma_0$ is defined by

$$\sigma_0^2 = \frac{\langle p_i^2 \rangle}{3}. \tag{A.8}$$

If, instead of a sudden fragmentation picture, an excitation–break-up picture is adopted, the total kinetic energy of the (excited) projectile nucleus at the moment of its break-up is

$$E_P = E_F + E_R \tag{A.9}$$

where $E_F$ and $E_R$ are the kinetic energies of the fragment and the removed part, respectively. Refering to the projection of the motion on one axis, say the z–axis (along the beam direction), we have

$$E_{P,z} = \frac{p_z^2}{2m_n A_F} + \frac{p_z^2}{2m_n(A_P - A_F)} \tag{A.10}$$

where $m_n$ is the nucleon mass and the fact that the momentum vectors of the fragment and the removed part are antiparallel (because of momentum conservation) has been used. This equation shows that the motion of the system along the $z$-axis corresponds to one degree of freedom, namely $p_z$. Thus, according to the theorem of energy equipartition, the average energy $\langle E_{P,z} \rangle$ will be $\frac{1}{2}kT$, where $k$ is Boltzmann constant and $T$ is the temperature of the projectile. Taking the average of eq. (A.10) and using the above argument, we have

$$\frac{\langle p_z^2 \rangle}{2m_n A_F} + \frac{\langle p_z^2 \rangle}{2m_n(A_P - A_F)} = \frac{1}{2}\, kT \tag{A.11}$$

which, since $\langle p_z^2 \rangle = \sigma^2$, finally gives the following expression for the width:

$$\sigma^2 = m_n kT\, \frac{A_F(A_P - A_F)}{A_P}. \tag{A.12}$$

Comparing this equation with eq. (A.7), the reduced width $\sigma_0$ is expressed as:

$$\sigma_0^2 = m_n kT\, \frac{A_P - 1}{A_P}. \tag{A.13}$$

# II Friedman's Model

The radial wave function $\psi_{F-R}(r)$ which describes the relative motion of the removed cluster $R$ and the observed fragment $F$ is approximated, near the nuclear surface, by the expression

$$\psi_{F-R}(r) \propto \frac{e^{-\alpha r}}{r} \tag{A.14}$$

where $\alpha$ is the wave-number of the relative motion:

$$\alpha = \frac{1}{\hbar}\sqrt{2\mu E_s} \tag{A.15}$$

where $\mu$ is the reduced mass of the system $F$–$R$, $\mu = A_F(A_P - A_F)/A_P$, and $E_s$ is its separation energy.

The form eq. (A.14) of the wave function corresponds to the quantum mechanical problem of a particle moving in a potential of the form

$$V(r) = \begin{cases} -V_0 & \text{if } 0 \le r \le x_0 \\ 0 & \text{if } r > x_0 \end{cases} \tag{A.16}$$

with energy $E = -E_s < 0$. Specifically, eq. (A.14) is the radial solution of the Schrödinger equation of the particle in the (classically forbidden) region $r > x_0$.

We express the radial distance $r$ in terms of the longitudinal $z$ and the transverse $r_\perp$ coordinates:

$$r = \sqrt{z^2 + r_\perp^2}. \tag{A.17}$$

Because of the peripheral character of the fragmentation process, we are mostly interested in the behaviour of the wave function $\psi_{F-R}(r)$ near the region where the cluster to be removed (upon interaction with the target nucleus) just "touches" the remaining fragment, that is near the point $(z = 0, r_\perp = x_0)$, where $x_0$ is the radius of the fragment, taken to be $x_0 = 1.2A_F^{1/3}$ (in fm). With this point in mind, we expand eq. (A.17) in a Taylor series about that point and keeping the lowest (nonzero) order terms in $z$ and $r_\perp$, we get

$$r \simeq \frac{z^2}{2x_0} + r_\perp. \tag{A.18}$$

Inserting $r$ from this expression into eq. (A.14) and separating the variables, we get

$$\psi_{F-R}(z, r_\perp) \propto \frac{e^{-\frac{\alpha z^2}{2x_0}}}{\sqrt{1 + \frac{z^2}{x_0^2}}} \frac{e^{-\alpha r_\perp}}{r_\perp}. \tag{A.19}$$

Thus, the wave function has been separated into two factors, each one depending on only one of the coordinates $z$ and $r_\perp$. Using this wave function, we can derive the longitudinal momentum distribution of the fragment. For this purpose, we evaluate the partial Fourier transform $\mathcal{F}_{F-R}(p_z, r_\perp)$ of the wave function $\psi_{F-R}(z, r_\perp)$ with respect to $z$ ($k_z = p_z/\hbar$):

$$\begin{aligned}
\mathcal{F}_{F-R}(p_z, r_\perp) &= \frac{1}{\sqrt{2\pi}} \int_{-\infty}^{+\infty} \psi_{F-R}(z, r_\perp) e^{-ik_z z}\, dz \\
&\propto \frac{e^{-\alpha r_\perp}}{r_\perp} \int_{-\infty}^{+\infty} \frac{e^{-\frac{\alpha z^2}{2x_0}}}{\sqrt{1+\frac{z^2}{x_0^2}}} e^{-ik_z z}\, dz \\
&\propto \frac{e^{-\alpha r_\perp}}{r_\perp} \int_{-\infty}^{+\infty} e^{-\left(\frac{\alpha}{2x_0}+\frac{1}{2x_0^2}\right)z^2} e^{-ik_z z}\, dz \\
&\propto \frac{e^{-\alpha r_\perp}}{r_\perp} e^{-\frac{k_z^2}{4\left[\frac{\alpha}{2x_0}\left(1+\frac{1}{\alpha x_0}\right)\right]}}.
\end{aligned} \tag{A.20}$$

The above Fourier transform is a mixed coordinate–momentum representation of the wave function. The last step has been obtained using the approximate expression $1/\sqrt{1+\frac{z^2}{x_0^2}} \simeq e^{-\frac{z^2}{2x_0^2}}$ and evaluating the resulting Fourier integral, using Tables of Integrals. The Fourier transform $\mathcal{F}_{F-R}(p_z, r_\perp)$, eq. (A.20), is then integrated over $r_\perp$ (simply integrating the $r_\perp$–dependent term). Taking its square modulus, the longitudinal momentum distribution $f(p_z)$ of the fragment is obtained:

$$f(p_z) \propto e^{-\frac{p_z^2}{2\sigma^2}} \tag{A.21}$$

with $\sigma$ given by

$$\sigma^2 = \hbar^2 \frac{\alpha}{2x_0}\left(1+\frac{1}{\alpha x_0}\right). \tag{A.22}$$

In order to include the contribution of the Coulomb interaction between the fragment and the removed part to the width of the parallel-momentum distribution, another approximate form of the relative wave function, containing the Colomb interaction,

will be derived. This is accomplished using a WKB approximation to the wave function in the region of interest. For $r \geq x_0$, the wave function can be written as (see e.g. Merz 70, page 117):

$$\psi_{F-R,WKB}(r) \propto \frac{1}{r} \frac{1}{\sqrt{k_c(r)}} \exp\left(-\int k_c(r)\, dr\right) \tag{A.23}$$

where

$$k_c(r) = \frac{1}{\hbar}\sqrt{2\mu(E_s + \frac{b_c}{r})} \tag{A.24}$$

where $b_c$ is the Coulomb parameter of the system $F$–$R$: $b_c = e^2 Z_F Z_R$. Defining as $y$ the ratio of the Coulomb energy at $r = x_0$ to the separation energy $E_s$, $y = (b_c/x_0)/E_s$, and using eq. (A.15), the function $k_c(r)$ is expressed as

$$k_c(r) = \alpha\sqrt{1 + \frac{yx_0}{r}} \tag{A.25}$$

Using this expression, the integral in eq. (A.23) is evaluated to give approximately

$$\int k_c(r)\, dr \simeq \alpha\sqrt{1 + \frac{yx_0}{r}}\, r \tag{A.26}$$

thus the wave function takes the form:

$$\psi_{F-R,WKB}(r) \propto \frac{e^{-\alpha\sqrt{1+\frac{yx_0}{r}}\, r}}{r}. \tag{A.27}$$

The form of this wave function is similar to that of eq. (A.14) (the $r$–dependence of the square root near $x_0$ is slow and can be neglected). Consequently, a treatment of this wave function similar to that of eq. (A.14) gives again a Gaussian $p_z$-momentum distribution, but in this case the width is given by:

$$\sigma^2 = \hbar^2 \frac{\alpha}{2x_0}\left(\sqrt{1+y} + \frac{1}{\alpha x_0}\right). \tag{A.28}$$

Note that this expression can be obtained from eq. (A.22) with the substitution $\alpha \rightarrow \alpha\sqrt{1 + \frac{yx_0}{r}}$ with $r = x_0$.

According to Friedman's model, the yield $\gamma_F$ of a fragment is expressed as

$$\gamma_F \propto S(Z_R, A_R)\, |\psi_{F-R}(r = x_0)|^2. \tag{A.29}$$

The factor $S(Z_R, A_R)$ expresses the relative probability for the removed part $R$ to contain $Z_R$ protons and is given by a hypergeometric distribution. The square modulus of the wave function at $r = x_0$ gives the probability for the system $F$–$R$ to be found at a "touching" configuration. Squaring eq. (A.14) we have

$$|\psi_{F-R}(r)|^2 \simeq N^2 \frac{e^{-2\alpha r}}{r^2} \tag{A.30}$$

where $N$ is a normalization constant. In order to evaluate $N$, we further assume that the wave function is constant up to a radius $R_c$ smaller than $x_0$, and varies exponentially according to eq. (A.14) for larger distances. Under this assumption, the normalization constant is found to be approximately

$$N^2 \simeq \frac{e^{2\alpha R_c}}{R_c}. \tag{A.31}$$

Inserting this expression of $N$ into eq. (A.30) and furthermore parametrizing $R_c$ as $R_c = x_0(1 - b)$, with $0 < b < 1$, we get:

$$|\psi_{F-R}(r = x_0)|^2 \simeq \frac{e^{-2\alpha(x_0 - R_c)}}{x_0^2 R_c} = \frac{e^{-2\alpha x_0 b}}{x_0^3(1 - b)}. \tag{A.32}$$

Substituting this equation in eq. (A.29), the following expression for the yield is obtained

$$\gamma_F \propto S(Z_R, A_R)\, \frac{e^{-2\alpha x_0 b}}{x_0^3(1 - b)}. \tag{A.33}$$

# Appendix B

# Supplement on Calculations for the Interim K1200 Beamline Experiment

In this appendix, a discussion of beam optics concepts relevant to spectrometer operations is presented and derivations of the equations developed for the analysis of the data obtained from the experiment with the Interim K1200 Beamline (chapter 3) are given.

## I Beam Optics concepts

In order to describe a particle as it passes through an ion-optical system, transfer coefficients can be introduced which express the change of the coordinates of the particle from one position to another [Care 87]. A reference trajectory is assumed for the system where the coordinate systems $x_0y_0z_0$ and $xyz$ are defined at the beginning and at the end of the system, respectively, with the $z$–axes pointing along the direction of the particle motion (fig. B.1). For simplicity, we assume that the system is mechanically symmetric about the $xz$–plane and the magnetic field on that plane is everywhere perpendicular to it (or zero). In the present system, this plane is the horizontal plane, which is also the dispersive plane of the dipole. The reference

trajectory passes through the quadrupole axes and the central orbit of the dipole magnet.

A particle is assumed to be emitted from the point $(x_0, y_0)$ on the plane $z_0 = 0$ at the beginning of the system with direction specified by the angles $\theta_0$ and $\phi_0$, the angles with respect to the $z$-axis made by the projections of the velocity of the particle on the $xz$ and $yz$ planes, respectively. After traveling through the system, it will emerge at the end of the system at the point $(x, y)$ on the plane $z = 0$ with direction specified by the angles $\theta$ and $\phi$. A reference (or central) momentum $p_0$ is defined for the system as the momentum necessary for a particle to follow the reference trajectory. The momentum of any other particle is then described by its deviation $\delta$ (in percent) from the reference momentum.

In order to take into account the differences in the length of different trajectories, a variable $l$ is introduced and defined as the path length difference between the trajectory of a given particle and the central trajectory of the system.

The beam-optical system maps the initial coordinates $x_0$, $\theta_0$, $y_0$, $\phi_0$, $l_0$, and $\delta$ of a particle that traverses it to the final ones $x$, $\theta$, $y$, $\phi$, $l$, $\delta$ ($\delta$ doesn't change, unless accelerating elements are present in the system). Thus, each coordinate of a particle at the exit of the system is a function of all the initial coordinates. For the final position, for example, we can write:

$$x = f(x_0, \theta_0, y_0, \phi_0, l_0, \delta) \tag{B.1}$$

The values of the coordinates $x$, $\theta$, $y$, $\phi$ and $l$ are in principle very small compared to typical lengths or angles of the spectrometer (for instance, the curvature radius and the bending angle of a dipole, respectively). Also, the momentum deviations $\delta$ of the particles from the reference momentum, are usually chosen to be small. As is usual in spectrometer operation, a large momentum range can be covered by changing

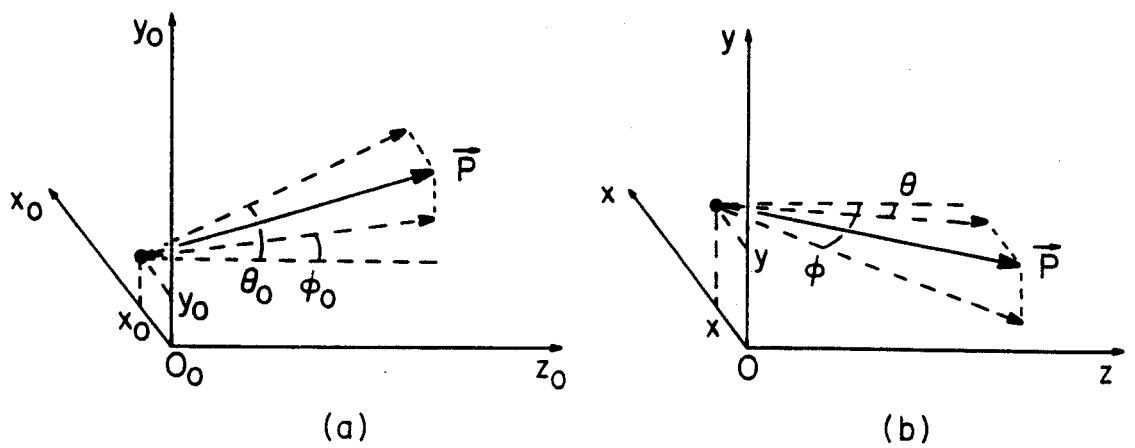


Figure B.1: Coordinate systems used in general beam optics calculations.

the fields of the magnets in sussessive steps, thus changing the value of the reference momentum $p_0$ (whereas keeping $\delta$ a small fraction of $p_0$).

Equation (B.1) can be expressed as a Taylor expansion in its variables, usually written as:

$$\begin{aligned} x &= (x|x)x_0 + (x|\theta)\theta_0 + (x|\delta)\delta + (x|l)l_0 \\ &\quad + (x|x^2)x_0^2 + (x|x\theta)x_0\theta_0 + (x|\theta^2)\theta_0^2 \\ &\quad + (x|x\delta)x_0\delta + (x|\theta\delta)\theta_0\delta + (x|\delta^2)\delta^2 \\ &\quad + (x|y^2)y_0^2 + (x|y\phi)y_0\phi_0 + (x|\phi^2)\phi_0^2 \\ &\quad + (x|\theta\delta^2)\theta_0\delta^2 + \cdots \end{aligned} \tag{B.2}$$

Each coefficient in this expression is a partial derivative of the function $x$ with respect to the indicated variable(s); so, for instance, we have: $(x|x) = \frac{\partial x}{\partial x_0}$, $(x|\theta) = \frac{\partial x}{\partial \theta_0}$, $(x|\theta\delta) = \frac{1}{2!}\frac{\partial^2 x}{\partial\theta_0\partial\delta}$, and so on. These coefficients are called transfer coefficients or matrix elements (of the corresponding order). Speciffically, the coefficient $(x|x)$ is the first order (horizontal) magnification and $(x|\delta)$ is the dispersion of the system. Also $(x|\theta^2)$ is called the geometric aberration and $(x|\theta\delta)$ is called the chromatic aberration. Due to the symmetry of the system about the $xz$ plane, terms of the form $(x|y^\mu\phi^\nu)$ with $\mu+\nu$ odd must be zero and are not included in expression (B.2).

The transfer coefficients are in general determined analytically. They can, for instance, be calculated by the matrix multiplication code TRANSPORT up to third order. Expressions similar to (B.2) can also be written for the coordinates, other than $x$, of the system.

If at the end of the system $(x|\theta) = 0$, we have a (first order) horizontal focus. In this case, the first order momentum resolution of the system is defined as the percent change in momentum needed to displace the first order image by a distance equal to its width $\Delta x = (x|x)\Delta x_0$, where $\Delta x_0$ is the horizontal size of the beam-spot at

the beginning of the system. Thus, the (first order) momentum resolution $R_1$ of the system is expressed as:

$$R_1 = \frac{(x|x)\Delta x_0}{(x|\delta)} \tag{B.3}$$

When $(x|\theta)$ is not zero and highter order terms [i.e. $(x|x\delta)$ and $(x|\theta\delta)$] are present, their effects have to be taken in to account in the calculation of the momentum resolution. In this case, the aberration-limited momentum resolution of the system can be written as:

$$R_{ab} = \frac{\Delta x_{ab}}{(x|\delta)} \tag{B.4}$$

where $\Delta x_{ab}$ is the overall image size resulting from the contributions of all the different aberrations. An approximate expression for $\Delta x_{ab}$ for the interim beamline spectrometer is given at the end of the next section.

# II Derivation of the expressions for the momentum and the reaction angle

The final position $x$ of a particle at the front counter is related to the initial position $x_0$, initial angle $\theta_0$ and $\delta$ with the expression [Care 87] (see Fig. 3.5a and 3.5b):

$$x = (x|x)x_0 + (x|\theta)\theta_0 + (x|\delta)\delta + (x|x\delta)x_0\delta + (x|\theta\delta)\theta_0\delta + (x|\delta^2)\delta^2 + (x|\theta\delta^2)\theta_0\delta^2 \tag{B.5}$$

where only the most important for the present system matrix elements are included (for example all $y$-dependent terms are dropped). After rearrangement, we can get the following equation for $\delta$:

$$\delta = \frac{x - (x|x)x_0 - (x|\theta)\theta_0}{(x|\delta) + (x|x\delta)x_0 + (x|\theta\delta)\theta_0 + (x|\delta^2)\delta + (x|\theta\delta^2)\theta_0\delta} \tag{B.6}$$

Substituting $\delta = 100\left(\frac{\rho}{\rho_0} - 1\right)$ in the left side of the above equation, omittimg the $(x|\delta^2)$ term (since it has a negligible contribution, see values in Table 3.2), and using the abbreviated expressions:

$$(x|\theta\delta)' = (x|\theta\delta) + (x|\theta\delta^2)\delta \tag{B.7}$$

$$(x|\delta)' = (x|\delta) + (x|x\delta)x_0 \tag{B.8}$$

we get:

$$\rho = \rho_0 + \frac{\rho_0}{100}\,\frac{x - (x|x)x_0 - (x|\theta)\theta_0}{(x|\delta)'\left(1 + \frac{(x|\theta\delta)'\theta_0}{(x|\delta)'}\right)} \tag{B.9}$$

Expanding the binomial in the denominator to first order in its argument (since it is small), we get:

$$\rho = \rho_0 + \frac{\rho_0}{100(x|\delta)'}\left(1 - \frac{(x|\theta\delta)'\theta_0}{(x|\delta)'}\right)(x - (x|x)x_0 - (x|\theta)\theta_0) \tag{B.10}$$

Now, referring to Fig. 3.5b), the position coordinate $x$, (with respect to the coordinate system $xOz$ in the horizontal plane), is related to the measured position $X_{FP}$ (in channels) as:

$$x = -\frac{X_{FP} - X_{ref}}{C_{FP}} + \alpha \tag{B.11}$$

in which the negative sign is due to the fact that the direction of increasing position as measured by the detector was taken to be opposite to that indicated by the coordinate system $xOz$. After substitution of this expression for $x$ in the above equation and some algebraic manipulation, keeping terms up to first order in $\theta_0$, we arrive at the relation:

$$\rho(\theta_0) = A_0(\theta_0) - A_1(\theta_0)X_{FP} \tag{B.12}$$

where:

$$A_0(\theta_0) = \left(\rho_0 + \frac{\rho_0}{100(x|\delta)'} x_{off}\right) - \frac{\rho_0}{100(x|\delta)'} \left((x|\theta) + \frac{(x|\theta\delta)'}{(x|\delta)'} x_{off}\right) \theta_0 \tag{B.13}$$

and

$$A_1(\theta_0) = \frac{\rho_0}{100(x|\delta)' C_{FP}} \left(1 - \frac{(x|\theta\delta)'}{(x|\delta)'} \theta_0\right) \tag{B.14}$$

with the definition:

$$x_{off} = \frac{X_{ref}}{C_{FP}} + \alpha - (x|x)x_0 \tag{B.15}$$

By writing the equations of $A_0(\theta_0)$ and $A_1(\theta_0)$ for $\theta_0 = \theta_b$ and subtracting the latter from the former, we finally get:

$$A_0(\theta_0) = A_0(\theta_b) - \frac{\rho_0}{100(x|\delta)'} \left((x|\theta) + \frac{(x|\theta\delta)'}{(x|\delta)'} x_{off}\right) (\theta_0 - \theta_b) \tag{B.16}$$

and

$$A_1(\theta_0) = A_1(\theta_b) - \frac{\rho_0}{100 C_{FP}} \frac{(x|\theta\delta)'}{(x|\delta)'^2} (\theta_0 - \theta_b) \tag{B.17}$$

In order to derive the equation for the scattering angle $\theta_r$, we start from the expression that relates the final angle $\theta$ of a particle at the front counter with the initial coordinates $x_0$, $\theta_0$ and $\delta$:

$$\theta = (\theta|x)x_0 + (\theta|\theta)\theta_0 + (\theta|\delta)\delta + (\theta|x\delta)x_0\delta + (\theta|\theta\delta)\theta_0\delta + (\theta|\delta^2)\delta^2 + (\theta|\theta\delta^2)\theta_0\delta^2 \tag{B.18}$$

Referring again to Fig. 3.5b we can write: $\theta = \theta_{FP} + \beta$, where $\theta_{FP}$ is the angle of a given particle with respect to the angle of the reference $0^o$ elastically scattered beam particles and $\beta$ is the angle of these arbitrarily chosen reference beam particles with

respect to the optical axis of the spectrometer. Substituting this into eq. (B.18) and rearranging, we get:

$$\theta_{FP} = C_0(\theta_0) + C_1(\theta_0)\delta + C_2(\theta_0)\delta^2 \tag{B.19}$$

with:

$$C_0(\theta_0) = -\beta + (\theta|x)x_0 + (\theta|\theta)\theta_0 \tag{B.20}$$

$$C_1(\theta_0) = (\theta|\delta) + (\theta|x\delta)x_0 + (\theta|\theta\delta)\theta_0 \tag{B.21}$$

$$C_2(\theta_0) = (\theta|\delta^2) + (\theta|\theta\delta^2)\theta_0 \tag{B.22}$$

By rewriting each of these equations for $\theta_0 = \theta_b$ and subtracting from the corresponding equation for $\theta_0$, we find:

$$C_0(\theta_0) = C_0(\theta_b) + (\theta|\theta)(\theta_0 - \theta_b) \tag{B.23}$$

$$C_1(\theta_0) = C_1(\theta_b) + (\theta|\theta\delta)(\theta_0 - \theta_b) \tag{B.24}$$

$$C_2(\theta_0) = C_2(\theta_b) + (\theta|\theta\delta^2)(\theta_0 - \theta_b) \tag{B.25}$$

Substituting these expressions into the equation for $\theta_{FP}$, and solving for $\theta_r = \theta_0 - \theta_b$, we get:

$$\theta_r = \frac{\theta_{FP} - (C_0(\theta_b) + C_1(\theta_b)\delta + C_2(\theta_b)\delta^2)}{(\theta|\theta) + (\theta|\theta\delta)\delta + (\theta|\theta\delta^2)\delta^2} \tag{B.26}$$

As mentioned in the previous section, the aberration-limited momentum resolution of the system can be expressed as

$$R_{ab} = \frac{\Delta x_{ab}}{(x|\delta)} \tag{B.27}$$

where $\Delta x_{ab}$ is the image size, which can be estimated to a first approximation, by an addition in quadrature of the contributions from the different aberrations. For the present system, for a given value of $\delta$, $\Delta x_{ab}$ can be estimated as:

$$\Delta x_{ab} = \left( [(x|x)\Delta x_0]^2 + [(x|x\delta)\Delta x_0 \delta]^2 + [(x|\theta) d\theta_0]^2 + [(x|\theta\delta) d\theta_0 \delta]^2 \right)^{1/2} \tag{B.28}$$

The scattering angle uncertainty $d\theta_0$ can be estimated, to a first approximation, as:

$$d\theta_0 = \frac{1}{(\theta|\theta)} \left( d\theta_{FP}^2 + [(\theta|x)\Delta x_0]^2 \right)^{1/2} \tag{B.29}$$

where $d\theta_{FP}$ is the uncertainty in the measured final angle $\theta_{FP}$. Expressions (B.28) and (B.29) follow from eqs. (B.5) and (B.18) respectively, where the most important terms are kept and a quadratic addition of the corresponding errors is performed.

# References

[Alon 84] J. Alonso, Proc. of the Workshop on Research with Radioactive Beams, Washington DC (1984), Lawrence Berkeley Laboratory Report 18187, unpublished and J. Alonso, A. Chatterjee and C. A. Tobias, IEEE Trans. on Nucl. Sci., **NS–26** (1978) 3003.

[Anne 87] R. Anne, D. Bazin, A. C. Mueller, J. C. Jacmart and M. Langevin, Nucl. Instrum. and Methods **A257** , 215 (1987).

[Bazi 90] D. Bazin, D. Guerreau, R. Anne, D. Guillemaud-Mueller, A. C. Mueller, and M. G. Saint-Laurent, Nucl. Phys. **A515** (1990) 349.

[Bert 81] G. Bertsch, Phys. Rev. Lett. **46** (1981) 472.

[Bibb 79] K. Van Bibber, D. L. Hendrie, D. K. Scott, H. H. Weiman, L. S. Schroeder, J. V. Geaga, S. A. Cessin, R. Treuhaft, Y. J. Grossiord, J. O. Rasmussen and C. Y. Wong, Phys. Rev. Lett. **43** (1979) 840.

[Blan 76] M. Blann, OVERLAID ALICE, U.S. ERDA Report No. COO-3494-29, Rochester, N.Y., 1976 (unpublished); also see F. Plasil and M. Blann, Phys. Rev. C **11** (1975) 508.

[Blat 52] J. M. Blatt and V. F. Weisskopf, "Theoretical Nuclear Physics", J. Wiley & Sons, 1952, p. 120.

[Blum 86] Y. Blumenfeld, Ph. Chomaz, N. Frascaria, J. P. Garron, J. C. Jacmart and J. C. Rounette, Nucl. Phys. **A455** (1986) 357.

[Bond 71] J. P. Bondorf, F. Dickmann, D. H. E. Gross, and P.J. Siemens, J. Phys. (Paris) Coll. C6 (1971) 145.

[Borr 86] V. Borrel, B. Gatty, D. Guerreau, J. Galin, and D. Jacquet, Z. Phys. A – Atomic Nuclei **324** (1986) 205.

[Bowm 73] J. D. Bowman, W. J. Swiatecki and C. F. Tsang, LBL report 2908 (1973), unpublished.

[Brad 88] F. P. Brady, W. B. Christie, J. L. Romero, C. E. Tull, B. McEachern, M. L. Webb, J. C. Young, H. J. Crawford, D. E. Greiner, P. J. Lindstrom, and H. Sann, Phys. Rev. Lett. **60** (1988) 1699.

[Bres 82] A. Breskin, Nucl. Instrum. and Methods **196**(1982) 11.

[Care 87] D. C. Carey, The Optics of Charged Particle Beams, Harwood Academic Publishers (1987).

[Care 88] D. C. Carey, Fermi National Accelerator Laboratory Technical Manual TM-1546, 1988, unpublished.

[Chen 68] K. Chen, Z. Fraenkel, G. Friedlander, J. R. Grover, J. M. Miller, and Y. Shimamoto, Phys. Rev. **166** (1968) 949.

[Egel 81] Ch. Egelhaaf, G. Bohlen, H. Fuchs, A. Gamp, H. Homeyer, and H. Kluge, Phys. Rev. Lett. **46** (1981) 813.

[Egel 83] Ch. Egelhaaf, M. Bürgel, H. Fuchs, A. Gamp, H. Homeyer, D. Kovar, and W. Rauch, Nucl. Phys. **A405** (1983) 397.

[Fox 89] R. Fox, R. Au, and A. VanderMolen, IEEE Trans. Nucl. Sci. (1989) 1562.

[Frie 83] W. A. Friedman, Phys. Rev. C **27** (1983) 569.

[Frie 87] E. M. Friedlander and H. H. Heckman, in Treatise on Heavy-Ion Reactions, edited by D. A. Bromley (Plenum, New York, 1987).

[Gali 88] J. Galin, Nucl. Phys. **A488** (1988) 297.

[Gelb 78] C. K. Gelbke, C. Olmer, M. Buenerd, D. L. Hendrie, J. Mahoney, M. C. Mermaz and D. K. Scott, Phys. Rep. **42** (1978) 311.

[Gold 48] M. Goldhaber and E. Teller, Phys. Rev. **74** (1948) 1046.

[Gold 74] A. S. Goldhaber, Phys. Lett. **53B** (1974) 306.

[Gold 78] A. S. Goldhaber and H. H. Heckman, Ann. Rev. Nucl. Part. Sci. **28** (1978) 161.

[Grei 75] D. E. Greiner, P. J. Lindstrom, H. H. Heckman, Bruce Cork, and F. S. Bieser, Phys. Rev. Lett. **35** (1975) 152.

[Guer 83] D. Guerreau, V. Borrel, D. Jacquet, J. Galin, B. Gatty and X. Tarrago, Phys. Lett. **131B** (1983) 293.

[Harp 71] J. D. Harp and J. M. Miller, Phys. Rev. C **3** (1971) 1847.

[Harv 81] B. G. Harvey, Phys. Rev. Lett. **47** (1981) 454.

[Harv 85] B. G. Harvey, Nucl. Phys. **A444** (1985) 498.

[Heck 72] H. H. Heckman, D. E. Greiner, P. J. Lindstrom and F. S. Bieser, Phys. Rev. Lett. **28** (1972) 926.

[Home 84] H. Homeyer, M. Bürgel, Ch. Egelhaaf, H. Fuchs, and G. Thoma, Z. Phys. A – Atoms and Nuclei **319** (1984) 143.

[Hufn 85] J. Hüfner, Phys. Rep. **125** (1985) 129.

[Kran 87] K. S. Krane, "Introductory Nuclear Physics", J. Wiley & Sons, 1987, p. 194.

[Kubo 90] T. Kubo, M. Ishihara, N. Inabe, T. Nakamura, H. Okuno, K. Yoshida, S. Simoura, K. Asahi, H. Kumagai and I. Tanihata, in *Proceedings of the 1st International Conference on Radioactive Nuclear Beams*, Oct. 1989, Berkeley, California, edited by W. D. Myers, J. M. Nitschke, and E. B. Norman, (World Scientific, 1990), p.563.

[McVo 80] K. W. McVoy and M. C. Nemes, Z. Phys. A – Atoms and Nuclei **295** (1980) 177.

[Merm 86] M. C. Mermaz, V. Borrel, D. Guerreau, J. Galin, B. Gatty, and D. Jacquet, Z. Phys. A – Atomic Nuclei **324** (1986) 217.

[Merz 70] E. Merzbacher, "Quantum Mechanics", 2nd edition, J. Wiley & Sons, 1970.

[Moni 71] E. J. Moniz, I. Sick, R. R. Whitney, J. R. Ficenec, R. D. Kephart, and W. P. Trower, Phys. Rev. Lett. **26** (1971) 445.

[Morj 88] M. Morjean, J. Frehaut, D. Guerreau, J. L. Charvet, G. Duchêne, H. Doubre, J. Galin, G. Ingold, D. Jacquet, U. Jahnke, D. X. Jiang, B. Lott, C. Magnago, Y. Patin, J. Pouthas, Y. Pranal, and J. L. Uzureau, Phys. Lett. **B203** (1988) 215.

[Morr 78] D. J. Morrissey, W. R. Marsh, R. J. Otto, W. Loveland, and G. T. Seaborg, Phys. Rev. C **18** (1978) 1267.

[Morr 79] D. J. Morrissey, L. F. Oliveira, J. O. Rasmussen, G. T. Seaborg, Y. Yariv, and Z. Fraenkel, Phys. Rev. Lett. **43** (1979) 1139.

[Morr 80] D. J. Morrissey, W. Loveland, M. de Saint Simon, and G. T. Seaborg, Phys. Rev. C **21** (1980) 1783.

[Morr 89] D. J. Morrissey, Phys. Rev. C **39** (1989) 460.

[Murp 83] M. J. Murphy, and R. G. Stokstad, Phys. Rev. C **28** (1983) 428.

[Murp 83a] M. J. Murphy et al., Phys. Lett. **120B** (1983) 75.

[Münz 90] G. Münzenberg, H. Geissel, P. Armbruster, K. H. Behr, B. Blank, K. H. Burkard, H. G. Clerc, M. Chen, J. P. Dufour, B. Franczak, J. J. Gaimard, E. Hanelt, R. Kirchner, O. Klepper, B. Langenbeck, F. Nickel, K. Poppensieker, M. S. Pravikoff, E. Roeckl, D. Schardt, K. H. Schmidt, H. J. Schött, Th. Schwab, B. M. Sherrill, K. Sümmerer and H. Wollnik, in *Proceedings of the 1st International Conference on Radioactive Nuclear Beams*, Oct. 1989, Berkeley, California, edited by W. D. Myers, J. M. Nitschke, and E. B. Norman, (World Scientific, 1990), p. 91.

[Myer 77] W. D. Myers, W. J. Swiatecki, T. Kodama, L. J. El-Jaick, and E. R. Hilf, Phys. Rev. C **15** (1977) 2032.

[Oliv 79] L. F. Oliveira, R. Donangelo, and J. O. Rasmussen, Phys. Rev. C **19** (1979) 826.

[Olso 81] D. L. Olson, B. L. Berman, D. E. Greiner, H. H. Heckman, P. J. Lindstrom, G. D. Westfall, and H. J. Crawford, Phys. Rev. C **24** (1981) 1529.

[Olso 83] D. L. Olson, B. L. Berman, D. E. Greiner, H. H. Heckman, P. J. Lindstrom, and H. J. Crawford, Phys. Rev. C **28** (1983) 1602.

[Path 72] R. K. Pathria, "Statistical Mechanics", Pergamon Press, 1972, p. 248.

[Rami 84] F. Rami, J. P. Coffin, G. Guillaume, B. Heusch, P. Wagner, A. Fahli, and P. Fintz, Z. Phys. A – Atomic Nuclei **318** (1984) 239.

[Rami 85] F. Rami, J. P. Coffin, G. Guillaume, B. Heusch, P. Wagner, A. Fahli, and P. Fintz, Nucl. Phys. **A444** (1985) 325.

[Sand 87] D. P. Sanderson, J. Nolen, R. Swanson, N. Mooney and R. Blue, National Superconducting Cyclotron Laboratory Annual Report 1987, p. 227, unpublished.

[Sher 87] B. M. Sherrill, N. Anantaraman, H. Blosser, R. Blue, S. Bricker, J. C. Dekamp, J. Easley, J. D. Johnson, H. Laumer, D. Lawton, F. Marti, L. Morris, J. A. Nolen, R. M. Ronninger, D. P. Sanderson, J. S. Winfield and A. F. Zeller, National Superconducting Cyclotron Laboratory Annual Report 1987, p. 183, unpublished.

[Sher 90] B. M. Sherrill, W. Benenson, D. Mikolas, D. J. Morrisey, J. A. Nolen and J. A. Winger, in *Proceedings of the 1st International Conference on Radioactive Nuclear Beams*, Oct. 1989, Berkeley, California, edited by W. D. Myers, J. M. Nitschke, and E. B. Norman, (World Scientific, 1990), p. 72.

[Silk 88] J. D. Silk, H. D. Holmgren, D. L. Hendrie, T. J. M. Symons, G. D. Westfall, P. H. Stelson, S. Raman, R. L. Auble, J. R. Wu and K. Van Bibber, Phys. Rev. C **37** (1988) 158.

[Soul 91] G. A. Souliotis, D. J. Morrissey, and B. M. Sherrill, Rev. Sci. Instrum. **62** (1991) 342.

[Stép 91] C. Stéphan, L. Tassan-Got, D. Bachelier, C. O. Bacri, R. Rimbot, B. Borderie, J. L. Boyard, F. Clapier, C. Donzaud, T. Hennino, M. F. Rivet, P. Roussel, D. Bazin, C. Grunberg, D. Disdier and B. Lott, Phys. Lett. B **262** (1991) 6.

[Stok 84] R. G. Stokstad et al., LBL report 18240, presented at Int. Conf. on Heavy Ion Physics, Mt. Fuji, Japan, Aug. 1984.

[Stok 85] R. G. Stokstad, Comments on Nucl. Part. Phys. **13** (1984) 231.

[Sümm 90] K. Sümmerer and D. J. Morrissey, in *Proceedings of the 1st International Conference on Radioactive Nuclear Beams*, Oct. 1989, Berkeley, California, edited by W. D. Myers, J. M. Nitschke, and E. B. Norman, (World Scientific, 1990), p. 122.

[Sümm 90a] K. Sümmerer, W. Brüchle, D. J. Morrissey, M. Schädel, B. Szweryn, and Y. Weifan, Phys. Rev. C **42** (1990) 2546.

[Tass 91] L. Tassan–Got and C. Stéphan, Nucl. Phys. **A524** (1991) 121.

[Viyo 79] Y. P. Viyogi, T. J. M. Simons, P. Doll, D. E. Greiner, H. H. Heckman, D. L. Hendrie, P. J. Lindstrom, J. Mahoney, D. K. Scott, K. Van Bibber, G. D. Westfall, H. Wieman, H. J. Crawford, C. McParland, and C. K. Gelbke, Phys. Rev. Lett. **42** (1979) 33.

[West 76] G. D. Westfall, J. Gosset, P. J. Johansen, A. M. Poskanzer, W. G. Meyer, H. H. Gutbrod, A. Sandoval, and R. Stock, Phys. Rev. Lett. **37** (1976) 1202.

[West 79] G. D. Westfall, L. W. Wilson, P. J. Lindstrom, H. J. Crawford, D. E. Greiner, and H. H. Heckman, Phys. Rev. **C19** (1979) 1309.

[Winf 86] J. Winfield, code "S320" (NSCL).

[Winf 91] J. Winfield, SARA Manual (NSCL).

[Wing 91] J. A. Winger, B. M. Sherrill, and D. J. Morrissey, Proc. EMIS Conf. (1991), in press.

[Yari 79] Y. Yariv and Z. Fraenkel, Phys. Rev. C **20** (1979) 2227.

[Zell 85] A. F. Zeller, R. T. Swanson, J. A. Nolen, D. Landry, M. J. Dubois and J. C. Dekamp, in *Proceedings of the 9th International Conference on Magnet*

*Technology* (1985), edited by C. Mazinucci and P. Weymuth (Swiss Institute for Nuclear Research, Zurich, 1985), p. 160 and J. C. Dekamp, C. T. Magsig, J. A. Nolen and A. F. Zeller, IEEE Trans. in Mag., **MAG–23** (1987) 524.